Alma Mater Studiorum · Università di Bologna

School of Science
Department of Physics and Astronomy
Master Degree Programme in Astrophysics and Cosmology

Receiver's Radiometric and Optical Optimization for Solar Observations in W-Band

Graduation Thesis

Presented by:
Federico Maria Rossi

Supervisor:
Chiar.mo Prof. Leonardo Testi

Co-Supervisor:
Dott. Fabrizio Villa

Academic Year 2024-2025
Graduation Date V

Contents

Introduction

The atmosphere of the Sun is the ensemble of its most external layers in which eruptive events can take place during periods of maximum solar activity, thus producing potentially hazardous threats to Earth's telecommunication systems and ground-based / space facilities, as much as to aeronautical workforce. The main focus of this thesis work is the design of a receiver capable of observing the solar activity in the microwave extended W-band, namely from 67 to 116 GHz: an up-to-now unprecedented spectral window for what concerns the observations of such phenomena, which may provide observational forecasting signals of these events. The Elegant Bread-Band n.2 (or EBB2) receiver, developed and characterized in this thesis, is part of the Solaris project, i.e. a network of single-dish antennas located in Italy and Antarctica which aims to a $24h$ global monitoring coverage of the solar activity, providing very concrete contributions and applications to the Space Weather branch of physics. As a matter of fact, the first chapter of this work is dedicated to an introduction to the Solar Physics and, in particular, to the structure of the atmosphere of the Sun and its fundamental magnetic activity, with the addition of key concepts about the physics of its radio band observable phenomena. Successively, a description of the Solaris project follows, where an overview of its main features, such as instrumental design, observing technique and current state of development, is provided in Chapter 2. Furthermore, the third Chapter of this work aims to provide a preliminary background on the general theory concerning radiometers and their practical applications, with a special focus on the concept of Gain compression and Y-Factor, two fundamental aspects essential to the derivation of the Noise Temperature of a receiver. This dissertation is an introduction to Chapter 4, which treats the full experimental characterization of the EBB2 receiver's single components and overall chain, as well as the study of its linear response in conditions simulating real solar events too, such as the so-called flares. Moreover, once the Noise Temperature of the device has been computed, thus marking its full characterization, real solar observations have been conducted for the first time by installing the EBB2 receiver in the 1.5 meter in diameter Solaris' Milano test antenna. In chapter 5 of this work, the results of such activity are discussed. Moreover in this chapter, the beam pattern simulation of the optical configurations of both Milano and the 2.6 meter ROSA antennas (Concordia station, Antarctica), through the employment of the software GRASP, are reported. This allowed the study of the convolutions of their beam pattern with temperature profiles extracted from real solar maps, obtained in previous observational campaigns. This last step not only made the simulations of real observation of both the Quiet and Active radio Sun possible, but it also cleared the way to a process of optimization for what concerns the choice of the Edge Taper value to adopt for future observations with ROSA Telescopes.

Chapter 1

The Sun: Structure, Magnetism and Radio Observable Phenomena

In this first chapter, the physical framework required to place the study of solar radio emission and its effects on space weather in context is provided. Following a summary of the Sun's basic characteristics and an explanation of its internal and atmospheric structure, special focus is placed on the magnetic field's function as the primary driver of solar activity and the 11-year Solar Cycle. The physical mechanisms and observational signatures of eruptive phenomena, flares, and active regions are then highlighted. The primary elements of solar radio emission are finally presented, laying the theoretical groundwork for the radio-band diagnostics that will be the focus of the ensuing chapters.

1.1 Solar Properties: Internal and External Structure

The Sun is a 4.5 billion years old $G2V$ spectral type main sequence star, located at approximately 150 millions Km from Earth. It is characterized by the following quantities, reported in *cgs* units:

- $R_\odot = 7 \cdot 10^{10}\ cm$;
- $M_\odot = 2 \cdot 10^{33}\ g$;
- $L_\odot = 4 \cdot 10^{33}\ erg/s$;
- $T_{e,\odot} \approx 5770\ K$.

1.1.1 Internal Structure of the Sun

The Sun's chemical composition consists in 70% of Hydrogen, 28% of Helium and a 2% of heavier elements and it possess a layered internal structure:

- **Core**: it is the region in which the processes of termonuclear reactions of the star take place and it extends up to approximately $0.25\ R_\odot$, with a temperature reaching about $T_{\odot,core} \approx 1.5 \cdot 10^7\ K$ and a mean density of $\overline{\rho_{\odot,core}} = 160\ g/cm^3$.
- **Radiative Region**: in this region, which extends between 0.25 and $0.7\ R_\odot$, the energy produced in the core is carried through the radiative transport mechanism, according to the Schwartzchild Criterium [11];

- **Convective Region**: it extends from $0.7\,R_{\odot}$ up to the surface; here the adiabatic gradient exceeds the radiative one and thus the energy is brought to the surface through a turbulent plasma convective motions-dominated transport [11].

1.1.2 External Structure: the Solar Atmosphere

Right above the convective region, the external structure of the Sun begins and it is divided in several main layers, i.e. photosphere, chromosphere, and corona. Given this work's interest in the study of the radio band solar phenomena, a part from the photosphere, which is related to the visible emission, both the just mentioned last two upper layers of the Sun's atmosphere, chromosphere and corona, will be treated more extensively. Furthermore, in this external regions, a heterogeneous radial gradient of the temperature can be observed [42].

- **Photosphere**: this region, $\sim 500\,Km$ of altitude, is considered as the surface of the Sun and is characterized by its optical transparency to the visible radiation, which is thus able to isotropically propagate following a Black Body emission. With an effective temperature of $\sim 5770\,K$, here is where both *Sun spots* and *active regions* (AR) forms;

- **Chromosphere**: the chromosphere is the lower layer of the solar atmosphere and, given the relatively high luminosity of the photosphere, it can be observed by naked eye only during a solar eclipse event. it is located approximately $2000\,Km$ above the photosphere. Here an initial temperature inversion has been observed: initially, a temperature decrease takes place ($\sim 4500\,K$) while, as the altitude increases, the temperature rises up to $\sim 10^4\,K$ will continue this ascending trend up to the last layers of the atmosphere. The reason behind this thermal behavior has not found an answer yet, remaining so a still highly debated argument; few hypotheses stand out, among which possible magnetohydrodynamic heating processes or even phenomena of reconnection of magnetic field lines in the corona [20]. As it will be treated in Sec.1.3.2, this is the region of major interest in the radio emissions of the Sun;

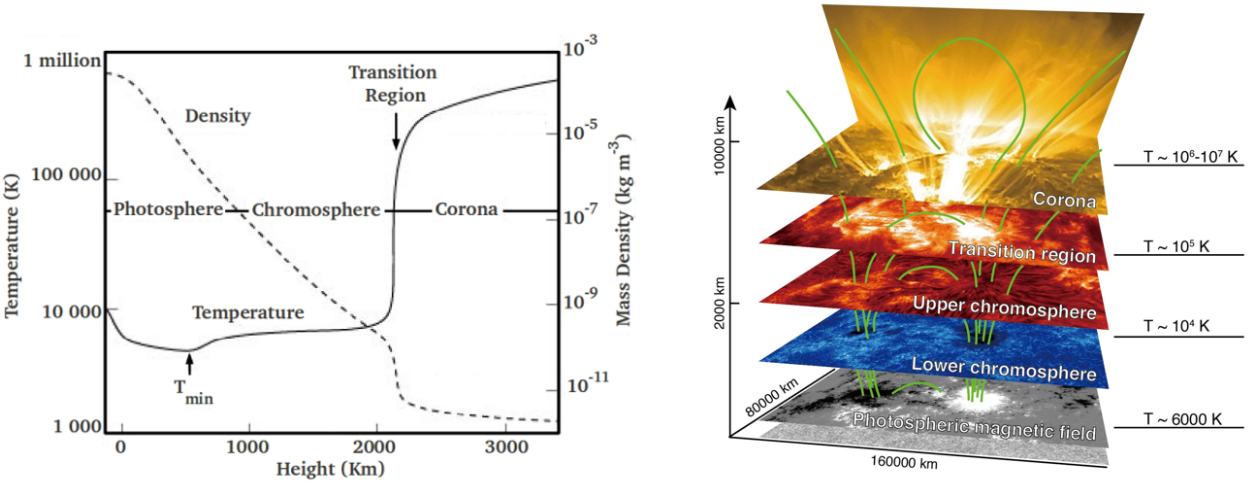

Figure 1.1: Left: Temperature and Density variations as a function of the height from the solar surface, where 0 Km stands for 1 $R_{\odot}$. The distinction within the mentioned layers of the Sun's Atmosphere is very well visible. Credits: [32]; **Right**: The structure of the solar atmosphere connected by magnetic (green) field lines. Corona: the hot upper atmosphere. Transition region: the thin atmospheric layer connecting the chromosphere and the corona. Chromosphere: the atmosphere up to about 2,000 km. Photosphere: the solar surface as seen in visible light. Credits: `https://solar-c.nao.ac.jp/en/`

- **Transition Region**: it consists in a region in the external surface of the Sun in which the temperature rises from the chromosphere's $10^4\ K$ to the typical coronal temperatures of the order of *millions* of Kelvins. However, as one can observe in Fig.1.1 , a plot showing the variation of temperature as a function of the Sun's Atmosphere altitude, the transition region is not considered as a proper physical layer lying between chromosphere and corona, but more as a volume of extremely irregular shape, still characterized though by a very thin thickness, thus reflecting the speed of the $10^4 \rightarrow 10^6\ K$ temperature transition [20];

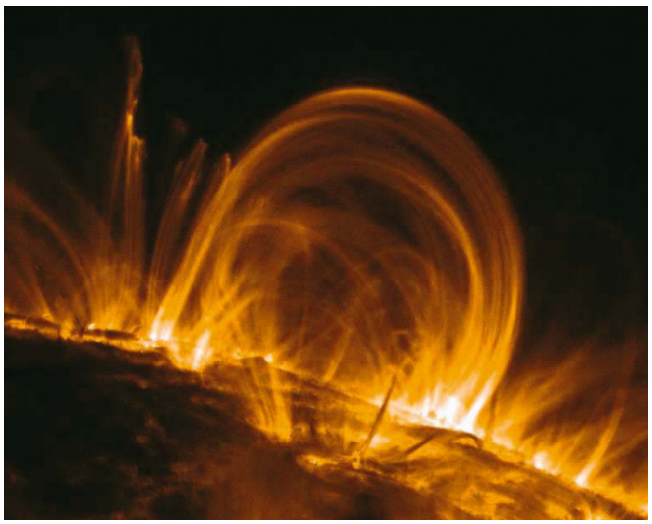

Figure 1.2: An image of the solar corona in X-rays taken by the Trace (Transition Region and Coronal Explorer) satellite. The image was obtained in a spectral band centered around 170 Å. Note the fine structure of the coronal loops outlining the magnetic field lines. Credits: [43]

- **Corona**: showed in Fig.1.2 , it is the most external region of the solar atmosphere and presents extreme temperatures of the order of $10^6\ K$ and its extension can reach the Earth and far beyond. The optical radiation of this feeble - very low density - gaseous envelope, due to its very faint brightness, can only be observed during an eclipse event or through dedicated instruments such as the coronographers. The shape of this region is heavily dependent on the *Solar Cycle* (treated in the next section): during the periods of minimum activity, the corona presents a quite reduced and semi-regular shaped extension with so called *streamers*, mostly stretching towards low latitudes. On the other hand, during the periods of maximum activity, the shape of the corona is much more extended and irregular, with streamers protracting almost isotropically [20]. The corona is the region in which *Coronal archs*, bridges of ultra-hot plasma usually connecting two Active Regions (AR), and Solar *prominences* (or *filaments*) can be observed: those can be classified in two families, i.e. quiescent prominences and *eruptive one*; the latter type can be associated to very violent events called *Coronal Mass Ejections*, or *CMEs*, showed in Fig.1.3. Other noteworthy phenomena are the *Coronal Holes*, examples of non-closed solar *loops* structures: mostly visible in x-rays, those area appear as impressive dark polar region (Fig.1.4) which forms due to magnetic field's lines which do not close and can, thus, form events of high-speed solar wind [20].

1.2 Solar Magnetic Field and Solar Activity Cycle

The *Magnetism* of the Sun is one the most studied aspects of Solar physics, since it is believed to be not only the starting point of the overall solar activity, but of the periodic *Solar Cycle*

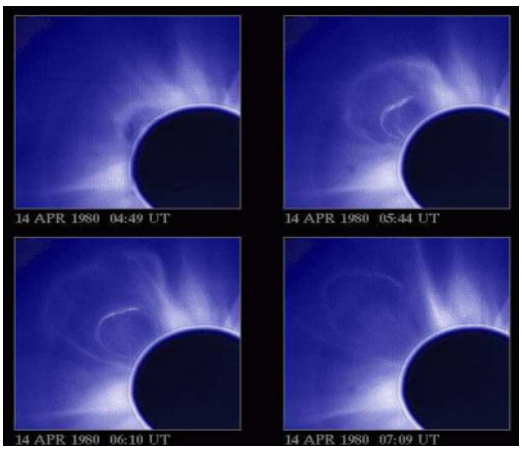

Figure 1.3: A spectacular CME occurred on April 14, 1980, observed with the coronagraph of the High Altitude Observatory aboard the Solar Maximum Mission. The last three images were taken at intervals of approximately one hour. Credits: [27]

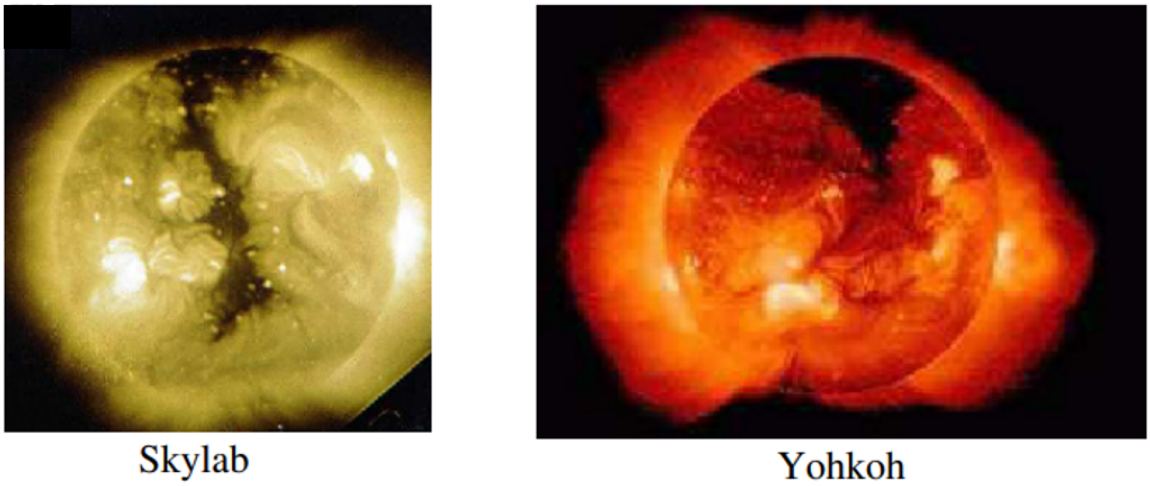

Figure 1.4: Those two images of the Sun ni the soft X-rays have been obtained from Skylab and Yokoh missions nearly twenty years apart (May 31, 1973, and May 8, 1992, respectively. In both images, the presence of a coronal hole is clearly visible. Credits: [20]

too, which will be treated shortly. The basis of the magnetism in the Sun lies on the fact that our star is composed for its most entirety by highly ionized fluid matter, the plasma. The motion of the free charges plunged in this fourth state of matter (which is responsible for the production of electric currents and magnetic fields themselves) is originated from the internal turbulent convective motions and by the *differential rotation* of the Sun: given the fluid nature of its composition, the angular velocity of the star varies as a function of the latitude and, more specifically, the equatorial region rotates more rapidly ($\sim 20\%$ faster) w.r.t. the poles; for this reason, the magnetic field lines, "frozen" in the plasma, start to curl, with a consequent thinning of the magnetic flux tubes (bundle of magnetic field lines enclosed in a tube-like regions of plasma), causing the amplification of the magnetic field itself. When a critical value is reached, the magnetic flux tubes start floating towards the surface, finally emerging as bipolar regions, i.e.**sunspots** (Sec.1.3.1) [20].
As already anticipated, the magnetic field of the Sun is the main engine of the Solar Activity Cycle: as a matter of fact, the star's magnetism presents a 11 years-long cycle which manifests mostly as a net variation of the sunspots visible on the surface of the Sun; it is thus the observable manifestation of the so called **Solar Dynamo** effect [37]. If the phenomenon of inversion of the magnetic polarity is considered too, however, it takes 22 years for the Sun to

go back to the last polarity configuration. This magnetic cycle is called **Hale's Cycle**, since the second Hale law exactly states that the sunspots polarity gets inverted after each cycle [20]. Fig.1.5 (bottom plot) highlights the relation within the sunspots' area expressed as a fraction of

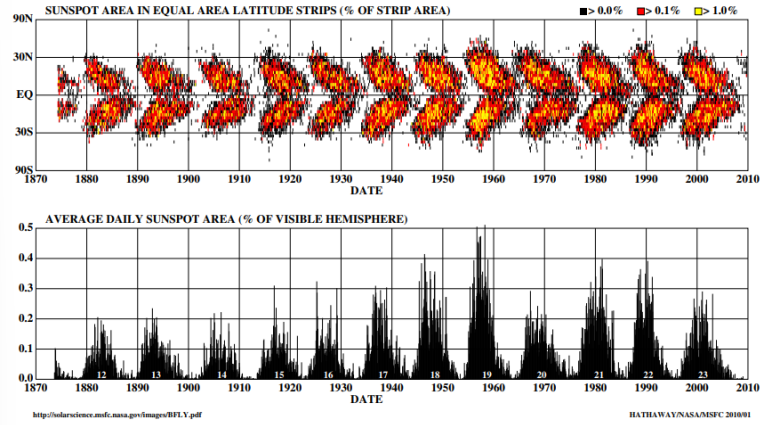

Figure 1.5: Top panel: latitudinal distribution of sunspots over time (*Maunder (Butterfly) Diagram*); **Bottom panel**: plot of the percentage of the visible hemisphere covered by sunspots, also as a function of time. Credits: [14]

the visible hemisphere (averaged on each stellar rotation) and the time; Another characteristic of the cycle is the latitude at which the sunspots appear, displayed in the top panel of the same Figure. This plot is the *Maunder diagram*, or *butterfly diagram*, and represents the visual representation of the *Sporer empirical law*: at the beginning of the cycle, the sunspots forms at relatively high latitudes ($\sim 30°$, on average) and then, as the cycle continues, they form closer to the equatorial region (latitudes as low as $\sim 10°$) [20]. Each point correspond to the position of a sunspot or AR in a given temporal position. The Solar Cycle Activity, though, is not just about the number of sunspots; several other solar events correlates with the minima and the maxima of the each cycle:

- **Shape of the Corona**: as already anticipated, it changes dramatically spanning from a very small extension and quite enlarged in the equatorial region, to a much more irregular and by far more extended conformation during the cycle maxima, with a generally higher coronal x-ray emission, as can be observed in Fig.1.6 ;

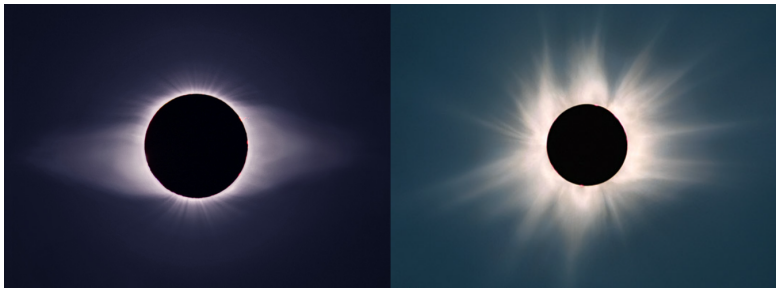

Figure 1.6: Left: image of the Sun's corona during a period of minimum solar activity. The picture was taken from a composite of eight separate photographs made by Fred Espenak (NASA Goddard Space Flight Center) from Dundlod, India during the total solar eclipse of 1995 October 24. One should note the shape of the corona limited to the equatorial regions only. Credits: [28]; **Right**: image of the November 1999 solar eclipse, taken by Wendy Carlos, composer and "coronaphile". Credits: [49]

- **Solar wind events**: the properties of the solar wind change, in conjunction with a higher Earth-experienced consequences such as polar lights, geomagnetic storm and radio-telecomunications disturbances
- **Number of explosive events**: During critical periods of maximum solar activity, the number of explosive events, i.e. *Solar Flares*, *Radio bursts* and *Prominences* (thus probable CMEs) increases dramatically.

1.3 Solar Events and Radio Emission

In this section, a more detailed description of the Active Regions (AR), i.e. the ensemble of the solar events whose frequency of appearance has been just discussed, is provided, with a focus on the *Solar Flares* and on the observation of those two phenomena in the wavelength of interest of this work: the radio band.

1.3.1 Active Regions and Flares

The *Active Regions*, or *AR*, are local regions in the solar atmosphere characterized by an organized and intense magnetic field, typically of bipolar nature and formed from the emergence of magnetic flux in the convective region. As already anticipated while discussing the solar magnetism in the previous section, their origin can be further explained as the emergence of magnetic field's tube-like structures forged by the solar dynamo effect: the field gets amplified in the inner layers of the Sun's convective region, thus creating a condition of magnetic instability. This causes those structures to start floating through *magnetic buoyancy*, finally manifesting themselves as *bipolar magnetic regions* on the photosphere, usually associated to pairs of opposite polarity *sunspots* [6][37]. As it will be briefly explained through the so-called Parker model, the sunspots represent just the base of a three-dimensional magnetic system which expands through the upper layers of the Sun Atmosphere. The **Sunspots** are considered one of the most striking phenomena of the solar magnetism. Fig.1.7 shows a real picture in

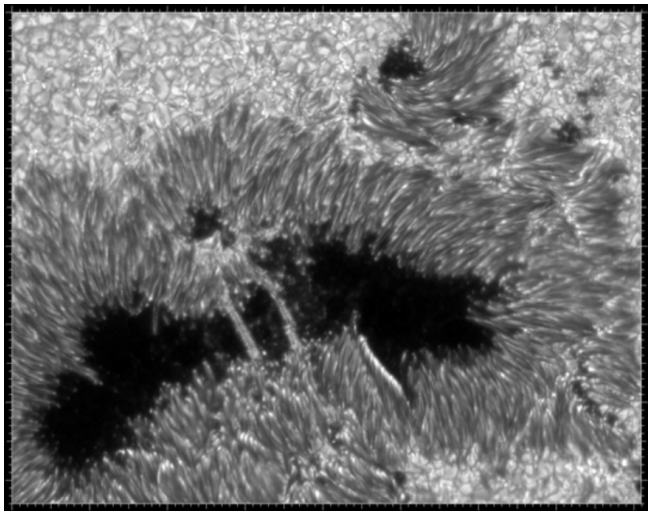

Figure 1.7: Image of a sunspot in white light acquired by the Swedish Solar Telescope (SST), owned and operated by the Institute for Solar Physics of the Royal Swedish Academy of Sciences. Umbra, penumbra, light bridges and bright dots features can be observed in the spot structure, as well as the convective cells surrounding it. Credits: [16]

white light[1] of a huge irregular-shaped sunspot, in which morphologic aspects of this event can

[1]Observation in integrated visible light, i.e. without filters isolating a single wavelength or spectral line.

be spotted, such as the *umbra* (the darkest region), *penumbra* (the gray region surrounding the umbra), *light bridges* (the two bright structures connecting the opposite shores of the penumbra) and *bright dots* in the inner region of the umbra. The sunspots typically presents circular of semi-circular shapes, with average diameters of the order of $\sim 30000\ Km$, almost three times the Earth. Their lifespans can vary based on their dimensions, typically being of the order of weeks, even increasing for bigger sunspots or group of them, which can even reach $\sim 10^5\ Km$ in extension. The darker appearance of a sunspot is caused by contrast w.r.t. the photosphere: as a matter of fact, their mean temperature is $\sim 4000\ K$ (vs the ~ 5800 of the photosphere). It is nowadays believed that this difference may rise exactly from the event which forms them:

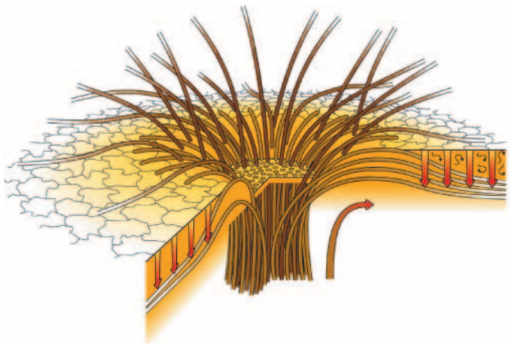

Figure 1.8: Schematic sketch on the insurgence of an AR: as can be observed from such representation, a tube-like magnetic field structure emerge from the photosphere, mostly interrupting the local convective motions and thus leaving a colder and very strong magnetic AR. Credits: [48]

the magnetic tubes, as can be visualized from Fig.1.8 , would actually inhibit the convective motions in the sunspots, thus ending in a by far lower energy transport efficiency w.r.t. to the one of the surrounding photosphere, consequently cooling down the interested region. In other words, the magnetic field-flooded solar plasma, by abating the energy transport, acts as a insulating medium [20].
As it is about to be further discussed, the AR are extremely tightly-linked with the majestic phenomenon of the **Solar Flares**. The *Solar Flares* are explosive phenomena which cause the emission in relatively short timescales of an enormous amounts of energy: for the most energetic events, values up to slightly less than $10^{33}\ erg$ are reached. Their emission interests all the electromagnetic spectrum, ranging from radio waves up to γ rays. Those spectacular events form in AR or in groups of AR particularly complicated in their magnetic topology: the higher the magnetic field's complexity, the higher the probability of flare occurrence. This concept can be explained through the *Parker Model* [20], i.e. one of the most accredited method out of the many in which the coronal heating processes (whose theoretical ambiguity has already been anticipated earlier) has been tried to be explained: by the time a new AR forms (hours/days timescales), the coronal magnetic field lines are arranged in well-organized loop structures connecting regions of inverse polarity. However (Fig.1.9), due to the photosphere convective motions, the bases (or "feet") of the single lines get chaotically dragged by the plasma, thus knotting, curling and intertwining them; in this magnetically complex scenario, when lines belonging to AR of inverse polarity interact with each other, the phenomenon of **Magnetic Reconnection** takes place, thus causing

- Plasma heating (the magnetic energy gets converted into thermal energy, heating up to $\sim 10^6\ K$);
- Particles acceleration (formation of the *Solar Energetic Particles*, or *SEP*, i.e. ions and electrons even ejected into open space)

Figure 1.9: Parker Model for coronal heating: the magnetic field lines connecting opposite polarity regions gets chaotically intertwined due to the convective cells plasma motions in the photosphere. In the regions in which different direction fields get in contact, the phenomenon of magnetic reconnection takes place, provoking the conversion of magnetic energy into thermal energy. Credits: [20]

- Hard X-rays and non-thermal radio emission (flare impulsive phase emission, tens of seconds/minutes timescales [3]).

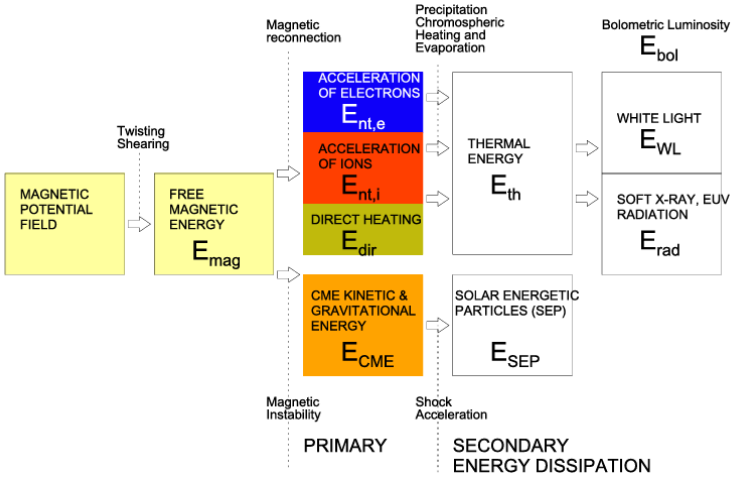

Figure 1.10: Schematic map of the physical processes that may occur during the phenomena of magnetic reconnections. Credits: [2]

This process, schematically shown in Fig.1.10, leads to the formation of Solar Flares and usually of CME too (causing the polar lights), even if the occurrence of flares is not bijective w.r.t. the other violent solar events discussed earlier, such as eruptive prominences and CME. Clearly, since these violent events are orignated in AR, their frequency of appearance is tightly linked to the Solar Activity Cycle.
The intensity of solar flares has been categorized by the *National Oceanic and Atmospheric Administration*, or *NOAA* [30], on the basis of their X-ray spectral luminosity in five different classes, reported on Tab.1.1. Generally, except for the X-class flares, the class is followed by

Class	X**-rays Power** $[W/m^2]$
A	$P < 10^{-7}$
B	$10^{-7} \leq P < 10^{-6}$
C	$10^{-6} \leq P < 10^{-5}$
M	$10^{-5} \leq P < 10^{-4}$
X	$P \geq 10^{-4}$

Table 1.1: *NOAA* flares logarithmic classification on the basis of X-rays Power in units of $[W/m^2]$

a number between 0 and 9 (for example, a $M.5$ flare corresponds to a $P = 5 \cdot 10^{-5}\, W/m^2$).

Given the large amount of high-energy particles beams in solar winds and in the magnetosphere produced by those phenomena, solar flares can cause serious impact on the Earth climate, as well as on satellites, orbiters and spaceships, astronauts crews included. A, B and C-type flares are quite frequent, with a very low impact on our planet; class M flares are able to cause radio blackouts on the hemisphere facing the Sun; the X-Flares, the most powerful among all the classes, occur more frequently during periods of maximum solar activity and can produce very strong geomagnetic storms and heavy radio blackouts.

1.3.2 Solar Radio Emission

The Solar radio emission is traditionally divided into a background component, the **Quiet Sun** (QS), a slowly varying component (associated mainly with AR) and a sporadic (*burst*) component [18]:

- **Quiet Sun - QS**: compared to the other components of the solar radio emission, the radio QS has the advantage of being fairly well understood as originating from *thermal bremsstrahlung* (free-free) in *local thermodynamic equilibrium*, or *LTE*, since it is generated by the electrons interacting with ions in the presence of relatively week magnetic field [42]. Under those conditions (and in general for radio weaves), its emission is well characterized by a Black Body under the Rayleigh-Jeans limit $h\nu/kT \ll 1$:

$$B_\nu(T) = \frac{2\nu^2 k_B T}{c^2} \,, \tag{1.1}$$

  where the Temperature T is not constant, but varies with ν: given the free-free emission mechanism, the cross section σ_{ff} (and thus the opacity, $k_\nu \propto n_e n_i \sigma_{ff} \rightarrow k_\nu \propto n_e^2 \sigma_{ff}$ since $n_e \approx n_i$ in ionized plasma) decreases with the frequency, since at first approximation

$$k_\nu \propto n_e^2 T^{-3/2} \nu^{-2} \,. \tag{1.2}$$

  For this reason, at high frequencies the plasma is less opaque, so deeper layers can be observed. At lower and lower frequencies instead, one can only see more external ones, which are characterized by higher and higher temperatures. So to give a practical examples, reasoning in terms of wavelengths, each λ identifies a different atmospheric layer:

  - ☐ $1\,mm \rightarrow$ lower Chromosphere ($\sim 4 - 6 \cdot 10^3\ K$);
  - ☐ $1\,cm \rightarrow$ higher Chromosphere ($\sim 10^4\ K$);
  - ☐ $10\,cm \rightarrow$ Corona ($\sim 10^6\ K$).

  Given its easy modeling, the radio Quiet Sun represents, thus, a very powerful diagnostic tool for the analysis of a wide range of atmospheric layers of the Sun, as it can be observed in Fig.1.11 .

- **Component-s** (slowly varying): radio observations are valuable in providing information on temporal variations of the emission from active regions. In particular, this specific component of the solar radio emission is associated to *non-flaring active regions*. The main mechanism of production of this emission is the thermal free-free radiation from hot plasma trapped in AR loop structures and it peaks around the $10\,cm$ wavelength. On long timescales, the total radio flux integrated over the whole disk is known to be a good index of solar activity, as it shows good correlation with relative sunspot numbers. However, signals of this components have an amplitude of almost two order of magnitude smaller compared to the QS component and intensity fluctuations caused by terrestrial atmosphere dominate [42];

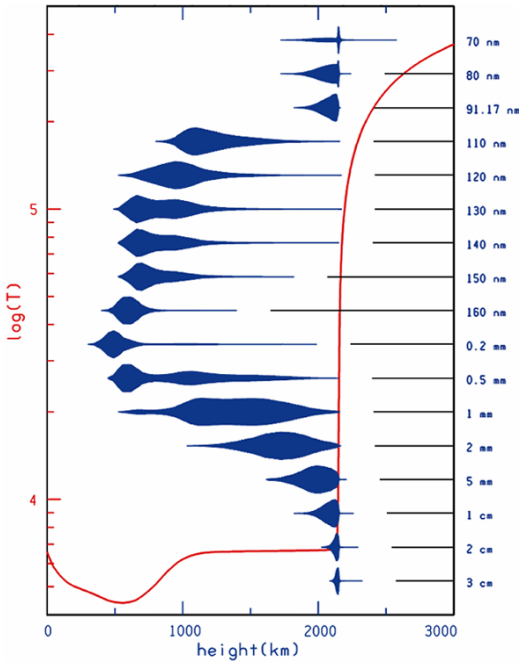

Figure 1.11: Contribution functions (blue) at several wavelengths, highlighting which atmospheric layer majorly contributes to the radiation observed at given frequency; the red line shows instead the behavior of the temperature as a function of the height (in Km units, where 0 represents the 1 $R_{\odot}$ Sun surface). Credits: [42]

- **Burst component**: the last component of the radio solar emission is characterized by non-thermal *emission bursts*, whose duration is typically included within few seconds up to few days and its intensity can surpass the one of the QS by several orders of magnitude. These radio bursts are tightly linked to the **solar flares** and they have been classified in five categories (*Type I-V bursts*) and each one refers to a different physical mechanism [20]. Speaking in terms of diagnostic contents, the two most important burst types are Type II and Type III bursts, since they are strongly connected to the flare events:

  - **Type II bursts - Coronal Shock Waves**: those radio bursts are associated to magnetohydrodynamical shock waves which are usually driven by fast Coronal Mass Ejections, CME [26];
  - **Type III bursts - Impulsive Electronic Acceleration**: maybe the most important type among the two, they represents the observational evidence of the acceleration of electrons driven by the already discussed effect of magnetic reconnection, forming thus Solar Energetic Particles (SEP) which can propagates through open magnetic field lines. Their importance come from their predictive power: before the occurrence of major flares, a series of Type III bursts can be observed, giving hints on initial preparation of magnetic reconnection, thus being a premature diagnostic of magnetic instability [3].

  A typical sequence of flare formation could thus observationally presents as follows:

  1. Magnetic instability in a AR;
  2. Impulsive Reconnection event → Type III
  3. CME ejection
  4. Coronal Shock → Type II
  5. Interplanetary propagation of the possible SEP

Finally, as for what concerns the radio-band electromagnetic emission of the AR, that is usually dominated by a *non-thermal gyromagnetic* component, a synchrotron emission generated by energetic electrons spiraling on their extremely intense magnetic field lines. This kind of radio emission represents thus a direct diagnostic not only of the coronal field but also of the populations of accelerated particles [10].

Chapter 2

The Solaris Project

This chapter describes the Solaris Project, including its technological advancements, operational plan, and scientific justification. Following an introduction to the network's conceptual framework and its applicability to Solar Physics and Space Weather applications, the discussion turns to the instrumental design, observing technique, and calibration strategy used for solar monitoring. Lastly, the project's current state of development is outlined, emphasizing the path toward an ongoing, worldwide solar monitoring network from prototype validation to the construction of Antarctic and mountain observation sites.

2.1 Introduction

The Solaris Project, namely 'A smart Solar imaging system at high radio frequency for continuous Solar monitoring and Space Weather applications' (Fig.2.1) is a network of small solar radio telescopes designed for operations in Antarctica and other polar/mountain sites which, under unique observing conditions (i.e. very low sky opacity and long solar exposures), is able to provide an unprecedented solar monitoring in radio W-band ($75 - 110\,GHz$)[1]. This can be achieved through *single-dish* imaging techniques at radio frequencies which can provide the mapping of the whole solar disk in less than 30 minutes, with a typical angular resolution of of $\sim 4'$. This process allows an unprecedented identification and spectral analysis of AR, *after* and *during* solar flare events, providing concrete advantages to both the Solar physics research and Space Weather applications. The scientific and technological background of Solaris is based on the knowledge pursued by the experience of the same research group on large single-dish radio telescopes observations at lower radio frequencies ($64\,m$ *SunDish* project [35] and $32\,m$ Medicina SRT INAF dishes [33]) [34], as well as on ALMA Band 2 receiver's developments [52].

2.2 Solaris: Concept, Objectives and Space Weather

As already anticipated, studying the solar atmosphere at different frequencies represents a major topic of current astrophysics and Space Weather; However, not only the high radio frequency observations are generally sparse, in particular in the $20 - 200\,GHz$ range, but the dynamic chromosphere activity lacks continuous/frequent monitoring suitable for Space Weather investigations: in particular, accurate measurements of the QS component of the Solar radio emission are lacking and/or scattered above $40\,GHz$. This is caused by the difficulty to separate the

[1]This is the standard W-band frequency range definition. In this work, it is alternatively considered as a W-band the extended 67-116 GHz frequency range.

Figure 2.1: **Left**: Solaris radio telescope 1.5 m prototype in Milan; **Center**: the Solaris 2.6 m station at Testa Grigia (Italian Alps); **Right**: the 2.6 m radio telescope at Concordia Station, Antarctica. Credits: [34]

pure QS from AR contributions, given the faint signal of the Solar radio emission's slow component w.r.t. the QS level (see previous chapter). The disentanglement of the two, as well as for peculiar large-scale structures such as coronal holes, loop systems and filaments, represent thus an open issue while studying radio ARs [21][50] and, as stated in the previous section, the AR-tightly linked signatures anticipating the flaring process can be quite observed by continuous radio monitoring. As a matter of fact, single-dish techniques offer accurate calibrated images independently from the target size, since actually free of synthesis imaging artifacts affecting the interferometric observations [23][33][24][22][34].

Speaking of QS, by employing the favorable observing conditions of Solaris network of antennas, a detailed measurements of the brightness temperature of the QS chromosphere and AR can be performed, contributing to Space Weather monitoring network and forecasts [34]. This is due to the very high solar radio brightness, which can be thus detected with relatively small telescopes and not particularly sophisticated detectors: for this reason, smart single-dish radio mapping of the solar disk is more suitable w.r.t. interferometric observations, given the necessity of dedicated and expensive short-baseline facilities requiring complicated calibration and data-analysis processes, especially for high frequencies. In this context, the Solaris Observatory can offer the unique opportunity of a continuous monitoring of the Sun in W-band in optimal conditions, during the Antarctic summers, operations impossible to achieve by the other presently available radio solar facilities [34]. This frequency band can offer a clear and unprecedented picture of both thermal and non-thermal evolution of the active sun, thus providing critical information about potentially hazardous solar events affecting both ground-based and space infrastructures, as much as aeronautical safety. In that direction, the broad-band analysis of eruptive events shows changes in their microwave/radio spectra a few days prior the event, suggesting both the emergence of a new AR photospheric magnetic field and shifting movements of the sunspots [42][4][5][1]. Such variations (i.e. *flattening* of the spectral index, computed by a multi-frequency analysis of the W-band radio solar spectrum) can be used as predictive criterion of eruptive and **geoeffective** events on the Sun, by anticipating the occurrence of flaring/CME processes.
Concerning the exploitation of the Solaris data, the operative plan is to focus thus on both Solar Physics Science and the Space Weather applications just described. Operatively speaking, the early science phase will include [34]:

- QS component's brightness temperature accurate measurement and monitoring of the slow component in W-band;
- Space Weather services focusing on continuous monitoring of flux/spectral variations of high-frequency counterpart of AR and flares;
- Correlation of detected solar events with high energy solar plasma flux on Earth and near-Earth space.

2.3 Solaris Receivers and Observation Strategy

The possible Solaris receivers will be built by taking advantage of the technological experience grown while developing the ALMA Band 2 receiver [52], whose first prototype was integrated and tested in the Solaris group's INAF-OAS laboratory, in Bologna. This technology, praising a world record in RF bandwidth ($[67-116]\,GHz$), suits very well for the goals of Solaris, since in principle it allows multi sub-bands instantaneously observations of the Sun (thus being able to compute a spectral index). However, as opposed to the ALMA receivers, the intense solar signal does not require a very high level of amplification for the Solaris' ones, nor a very low level of system noise, thus avoiding the cryogenic temperatures' work as for usual radioastronomy receivers. Yet, they need to be carefully designed and optimized so to not run into saturation due to the just mentioned high solar signal. as well as being sufficiently thermally stable while performing measurements.
For what concerns the *observation strategy*, the solar mapping is performed through 25 minutes-each *Equatorial On-The-Fly* (OTF) imaging scans, which provide continuous data acquisition through scans of the solar disk in RA and Dec (1.5° x 1.5° map, $5\,arcmin/s$ scan speed, 4 scans/beam). Features on the solar disk can evolve on very short timescales, thus daily - or even more frequent - monitoring is the optimal choice for dedicated radio solar facilities. When observing in Antarctica sites with *OASI* [9] and *COCHISE* [40] Telescopes, located respectively at the Mario Zucchelli Site (MZS) and Concordia base station, due to the very long Solar visibility windows, $\sim$ 20 solar images/day can be produced during summer, according to simulations including overheads and accounting for local orography [34]; this will allow unprecedented continuous solar monitoring hourly, finally producing output FITS images suited for further analysis by standard astronomy tools. Furthermore, given the apparent proper motion of the Sun in celestial coordinates of about $2.5\,arcmin/hour$, a blurring effect comparable to the beam size affects the raw images, for a typical mapping time of $\sim$ 1.5 hours. This can be seen in Fig.5.18 (Sec.5.2.1), which shows one of the Sun images obtained during the 2025 Antarctica Solaris mission. Finally, calibration observations are required to convert the raw maps to brightness temperature images; a brightness reference of about $7000\,K$ has been obtained for the QS level in the Solaris frequency range [19].

2.4 Project development

In summary, the development of the Solaris program can be structured as follows [34]:

1. **University of Milano Telescope prototype** : there, a $1.5\,m$ telescope has been realized for instrumentation and procedure development, validation and early tests. The first light of such instrument has been obtained on March 2024, observing the brightness profile of the solar disk in the $[86.7, 102.9]\,GHz$ frequency range, shown in Fig.2.2;

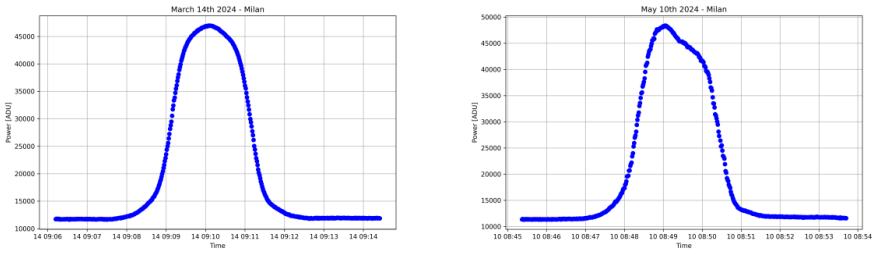

Figure 2.2: Left: First light of the Solaris 1.5m radiotelescope prototype in Milan obtained through a solar transit observation in March 2024; **Right**: test observation during the "Mother's Day" geomagnetic storm in May 2024, in which is clearly detected a very powerful Active Region. Credits: [34]

2. **Mountain Station establishment**: a 2.6 m radio telescope (with a twin primary mirror to the Antarctica Solaris antennas) has been installed by Sapienza University in Rome at Testa Grigia Station [15], located on the italian Alps at 3500 m a.s.l. Such site provides good sky conditions in extreme mountain environments, mimicking Antarctica-like conditions but in a more accessible location. Testa Grigia provides mid-season solar coverage, complementary to polar monitoring;

3. **Antarctica permanent solar observatory**: both in Mario Zucchelli and Concordia stations, Antarctica, a permanent Solaris polar Observatory has been approved by the *PNRA* (Italian National Program for Antarctic Research). There, Solaris exploits already existing radio telescopes, OASI and COCHISE as previously named, in both the above mentioned stations for solar monitoring at high radio-frequencies;

4. **Northern hemisphere observatory**: Solaris program aims toward a 24h global coverage for high-frequencies solar monitoring during the whole year. This can be achieved by the future realization of a Northern hemisphere Solaris station: feasibility studies for the implementation of Solaris in suitable Scandinavian/Arctic sites are ongoing.

5. **5m UniCal Telescope:** a 5-meter class telescope is foreseen to be installed at the University of Calabria to observe the sun in K-band (18-26 GHz).

Chapter 3

Radiometers and VNA Analysis

Basic concepts for microwave Radiometers and measurements useful for the EBB2 receiver's characterization are presented in this chapter. The first section covers the basics of radiometers' theory necessary to this work's operative steps, such as the important parameters to characterize the microwave receiver's output power. It then moves on to the physical principles of the receiver's fundamental parts, the Square-Law Detector Diodes and the Low Noise Amplifiers, with a focus on Gain Compression and the Y-Factor method for determining the receiver's noise temperature. The second and final part of this chapter introduce the Vector Network Analyzer (VNA), the instrument used to fully characterize the receiver's components, and the Scattering Matrix formalism, which offers the mathematical basis for the RF network analysis.

3.1 Elements of Radiometers Theory

Microwave receivers (MWRs) are devices capable of detecting the electromagnetic waves in the microwaves band, from centimeter wavelengths up to the sub-millimeter, corresponding to a frequency range between 1 GHz and 1 THz [13]. The receiver is responsible for amplifying, filtering, and combining the incoming signal to properly detect the signal itself with a Signal-to-Noise Ratio necessary to measure the astrophysical properties of the sources in the sky. The technology implemented in Solaris receivers is based on the total-power receiver's architecture and utilises HEMT-based Low Noise Amplifiers (LNAs) as the active components, thus amplifying the signal to detectable levels. In Fig.3.1, a simple sketch which depicts the detection process of a receiver, which is about to be treated in further details (the assumed structure is the one of the EBB2). Two fundamental relations regarding the microwave receivers, which

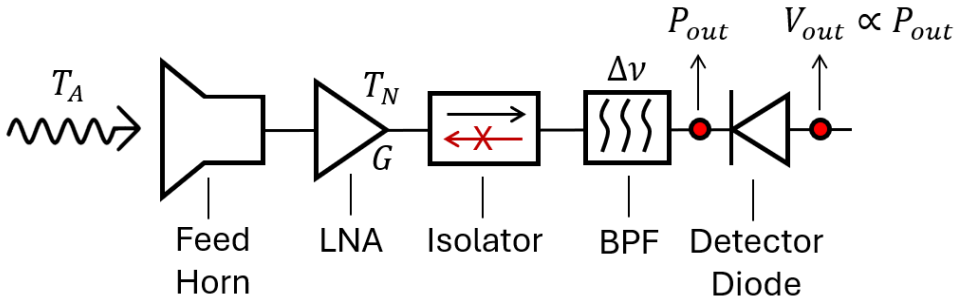

Figure 3.1: The block diagram of the EBB2 receiver and its detection process.

will be extensively used in this work, are the following [17]:

$$\Delta T_{min} = \frac{T_{sys}}{\sqrt{\Delta\nu \cdot \tau}} \tag{3.1a}$$

$$P_{out} = G \cdot (T_N + T_A) \cdot k_B \cdot \Delta\nu \tag{3.1b}$$

where

- T_{sys} is the **system temperature**, which is the sum of the receiver's total noise temperature, T_N, and the input Antenna Temperature T_A;
- τ is the **integration time** of a single measurement point;
- $\Delta\nu$ is The working frequency range of the receiver,
- P_{out} is the power at the output of the radiometer, after the aplification stage.
- G is the **Gain** of the system: it quantifies the overall amount of amplification of the input signal. Furthermore, as its unit of measure $[\frac{Volt}{Kelvin}]$ testifies, it represents the conversion factor within the output receiver's power and the total temperature of system;
- k_B is the The Boltzmann constant.

Eq. 3.1a, which will be employed during the discussion on the convolutions treated in Sec.5.2, refers to the *Radiometer Sensitivity*, being ΔT_{min} the minimum variation of temperature detectable by the receiver itself. Its dependence on the inverse of the square root of τ, i.e. the *integration time*, implies that the higher the integration time, the higher the amount of data collected and, consequently, the smaller the variation of temperature which can be detected by the receiver, resulting in a higher radiometric sensitivity. The same concept applies to the dependence on $\Delta\nu$, the overall bandwidth of the radiometer: the larger the bandwidth, the higher the sensitivity.
For what concerns Eq. 3.1b, it highlights the dependence of the output power of the receiver on input temperature : it is related to T_N and G, which are the most important characteristics parameters of the radiometer and have to be estimated with very high precision. An important post-processing anlysis of a radiometer detection data is to convert its output power P_{out} into the actual physical variable related to the observed source, T_A, by decoupling it from the internal noise produced by the instrument itself. For this reason, the aim of its characterization, as will be applied for the EBB2 receiver in this work, is to accurately determine the couple of values (G, T_N), so to identify the amount of noise equivalent temperature produced internally. In the T_N computation, the concept of Y-Factor is a key application, as will be discussed in Sec3.3.3. Moreover, in the total power architecture, a square-law detector converts the RF signal into a DC Voltage whose value is proportional to the RMS of the power entering the detector $V_{out} \propto P_{out}$. Equation 3.1b can be thus rewritten in a more general way:

$$V_{out} = G^* \cdot (T_A + T_N) \cdot k_B \cdot \Delta\nu \,, \tag{3.2}$$

where G^* in $[V/K]$ units, accounts for total gain of the receiver and the constant of the square-law detector. The equivalence between the Temperature and Power has been employed in this work too, especially during the application of the concept of linearity of a receiver, treated in the following sections: in 1928, J. B. Johnson and H. Nyquist proved that each resistive component of a circuit generates thermal noise, thus behaving as resistors and emitting a Noise Power which is linearly proportional to their physical temperature T_{phys}, in the bandwidth of operation [17]:

$$P_{noise} = k_B \cdot T_{phys}.\Delta\nu \tag{3.3}$$

A discussion about two types of RF components mounted in the EBB2 receiver will be now presented.

3.2 The Square-Law Detector Diodes

The *Square-Law Detector Diode* is a *passive* electronic device capable of detecting RF signals: in order to do so, it converts an input *Alternated Current* (AC), which is an oscillating signal, into a constant output *Direct Current*, or *DC*. In particular, this behavior can be described by the following relation [8]:

$$V_{out} \propto V_{in}^2 \,, \tag{3.4}$$

thus highlighting its denomination as "Square-Law" detector. Eq. 3.4 comes from the application of the *Ohm Law* to the power equation for an electric circuit, namely

$$\begin{cases} V = R \cdot I \\ P = V \cdot I \end{cases}$$

By plugging the current I from the Ohm Law ($I = V/R$) into the power equation, it results in $P = V^2/R$ and, thus, in the proportionality $P \propto V^2$. This last simple relation, if applied to Eq. 3.4, fully describes the behavior of Detector Diodes, since

$$V_{out} \propto V_{in}^2 \propto P_{in} \,. \tag{3.5}$$

Therefore, Eq. 3.5 underlines two important trends: a non-linear behavior within input and output *voltages* and, instead, a *linearity* w.r.t. the input power at the detector. Thus, the Diode, mounted as the last component of the RF Chain, possesses a linear proportionality between the power of the incoming oscillating signal entering the device itself and its output DC voltage, thanks to its nature as non-linear device. The range of input powers (units of dBm[1], or mW) hosting this particular response is characterized by the following relation [8]:

$$V = K(\sqrt{P_{in}})^{\alpha/2}, \tag{3.6}$$

and it describes the *Square-Law region*, where the working range is set for $\alpha = 2$: this relation comes from the Taylor expansion of the Diode behavior in the case of small input signals ($P_{in} < -20\, dBm$) only. Furthermore, K is an experimental proportionality constant which depends on several features of the Diode itself, such as the impedence of the system and, partially, on the frequency of the signal. In particular, in the Square-Law region, K provides a conversion factor between the output voltage and the input power:

$$K = \frac{V_{out}\,[V]}{P_{in}\,[W]} \tag{3.7}$$

Following Eq. 3.7, bigger values of K describe highly sensitive Diodes, for which to low input values of Power follow significant output voltages.

3.3 The Low Noise Amplifiers

The amplifiers employed in radioastronomy are called *Low Noise Amplifiers*, or *LNAs*. In this section, their properties will be discussed: by doing so, a detailed description of their functioning will be provided, in order to fully understand the practical application of these devices, employed in the receiver which have been developed during this thesis work.

[1] As opposed to the dB, unit of relative power, the dBm is a unit of absolute power which refers to the power level relative to 1 mW as it is expressed as $P_{dBm} = 10 \cdot \log_{10}(P/1\ mW)$

3.3.1 LNAs and HEMTs

A *High Electron Mobility Transistor*, or *HEMT* [8], is a device in which an applied voltage is able to rearrange the electrons allocated in a two-dimensional gas, feature which highly enhances their mobility since, by being forced to move in a quantum mechanically-confined plain, they are significantly less exposed to scattering phenomena. The result of this modification of the charge distribution is the creation of a privileged channel of electrons propagation. It is the most used technology for amplifying high frequency signals at microwaves. The HEMTs are controlled by a set of three variables:

- The *Drain Current*, I_d;
- The *Drain Voltage*, V_d;
- The *Gate Voltage*, V_g.

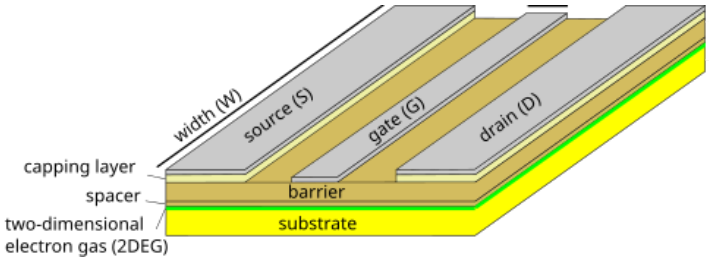

Figure 3.2: The HEMT structure with the three terminals: Source, Gate and Drain. In green, the two-dimensional electron gas (*2DEG*)

The latter is the one which, once applied to the *Gate Terminal*, i.e. one out of the three HEMTs' *Terminals*, is able to produce the above-mentioned charge rearrangement and, furthermore, to control the current between the other two terminals: the *Drain Terminal* and the *Source Terminal*. The overall set of values I_d, V_d and V_g is known as *Bias*, and its **tuning** can optimize the HEMT's performance and response, or, in other words, can improve the *amplification* of the incoming electromagnetic signal. A Low Noise Amplifier, or LNA, is a device structured as several cascaded HEMTs, stacked and packed into a compact configuration. As a matter of fact, the so called *LNA Packaging* is a fundamental aspect of amplifiers design, determining their final performance and capability of surviving in extreme condition too. This device is classified as an *active component* since, by being externally powered is able to provide a positive Gain to the RF chain of a receiver, thus *amplifying* an incoming signal. On the other hand, this does not happen with *passive components*, since they are not connected to any external power supply and thus they are only able to attenuate or at best conserve the signal flowing through them. In Fig.3.3 the so called power block unit, wired to a power supply to drive the LNA of Solaris receivers, is shown.

3.3.2 Gain Compression

The *Gain Compression* [8] is a topic which represents a key aspect of radiometer's design, for this reason, it is here discussed. It refers to the phenomenon through which an input power, P_{in}, exceeds the limit below which the output one, P_{out}, is *linearly* amplified. This effect acquires a very high relevance in the receiver employed in this work, since the Solaris project aims to perform solar observations in the W-Band: the very high solar radio brightness (already introduced in Sec.2.3) could easily lead to the effect of *saturation* by exposing the receiver to very high P_{in} input values.

In order to explain this phenomenon, the so-called *Amplification Curve* must be introduced: as displayed in Fig. 3.4, this plot shows the relation within an input value of power, in *absolute power* units, $[dBm]$, and its corresponding output one. When this relation is linear (highlighted by the orange area in the figure), a *constant Gain* condition is satisfied. Usually, as the input power keeps increasing, the real response starts to differ from the theoretical linear one: in this region, a saturation of the signal starts, thus reaching the condition of Gain Compression where, ultimately, the output power does not vary anymore, as the input power increases. This area of compressed Gain is called *Compression region*. A way to identify the threshold between the two areas explained so far is the so called $1\,dB$ *compression point*, or $P1dB$: this information is usually provided in the LNAs' Data sheets and it refers to the point in which the input power differs of $1\,dB$ w.r.t. the output one, signaling the very entrance of the saturation regime.

3.3.3 Y-Factor and Noise Temperature

The Y-Factor is the experimental procedure through which the receiver is characterized in terms of noise, thus through which the noise temperatureT_N, and gain, G, are measured [51]. Since the radiometer equation Eq.3.1b represents a linear behavior in the cartesian plane (P_{in}, P_{out}), as shown in Fig.3.4, the response can be measured in such linear region by providing two

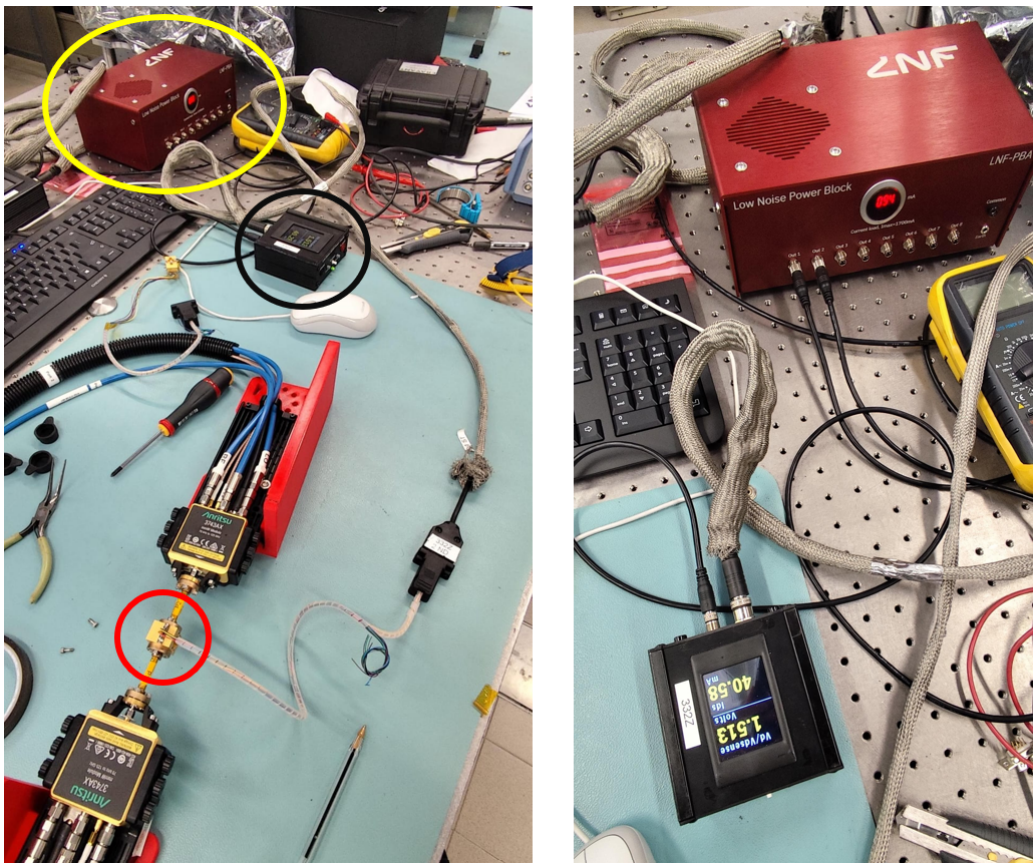

Figure 3.3: Left: power system of the LNA used in Solaris. The HEMT LNA device (red circle) is powered by a power block unit (yellow circle) which provides energy to the power supply (black circle), i.e. the device through which the bias levels can be controlled and tuned. **Right**: image of the power block - power supply system. The Low Noise HEMT Power Supply is the "switchboard" through which the Drain Current I_d and the Drain Voltage V_d can be tuned. The V_g can be instead measured with a multimeter. The LNAs commercial suppliers usually already provide the so called *Nominal Bias*: the best combination of V_d, I_d and V_g corresponding to the most optimized Gain value.

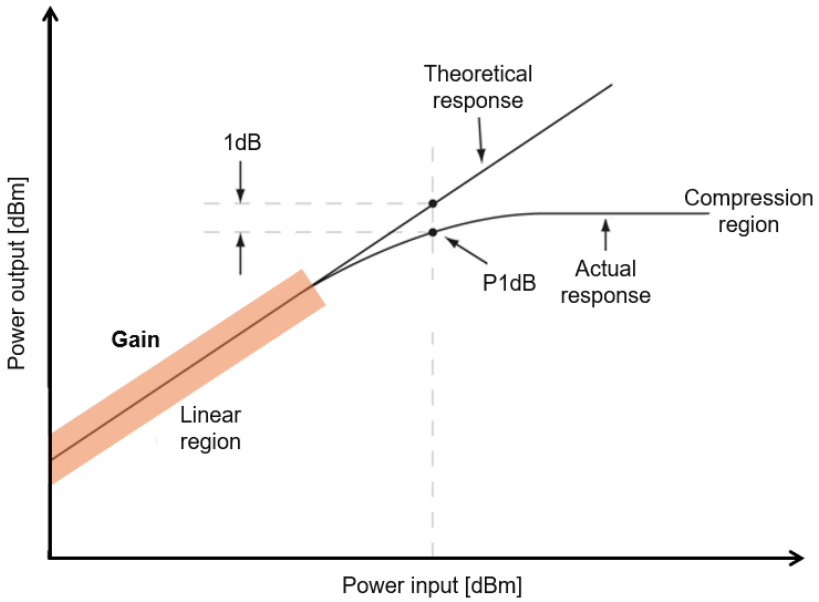

Figure 3.4: The Amplification Curve: highlighted in orange, the linear region of the curve, where the amplification linearly return an output power from an input one (absolute power units, $[dBm]$). Outside this region, the compression is showing the saturation of the amplification: the same output power results from higher an higher input ones (Compression region).

different levels of input antenna temperature, namely a *hot source* T_H and a cold *cold source* T_C, recoding then the respective output power. The Y-Factor is expressed as

$$Y = \frac{P_{out}^H}{P_{out}^C} , \tag{3.8}$$

where P_{out}^H and P_{out}^C are, namely, the output power of the receiver pointed at the hot source and its output power pointed at the cold one. Alternatively it can be defined in terms of Voltage outputs after the detection stage, so

$$Y = \frac{V_{out}^H}{V_{out}^C} . \tag{3.9}$$

In this work, the direct observation of the Sun will be used as hot source and the sky background signal as the cold one. To proceed with, if Eq. 3.1b is plugged in both numerator and denominator of Eq. 3.9, the Y-Factor becomes

$$Y = \frac{Gk_B\Delta\nu \cdot (T_H + T_N)}{Gk_B\Delta\nu \cdot (T_C + T_N)} = \frac{T_H + T_N}{T_C + T_N}$$

which, by multiplying both members for $(T_C + T_N)$ and by grouping by the Y-Factor, it transforms into

$$Y \cdot T_c + Y \cdot T_N = T_H + T_N$$

Finally, it is possible to obtain the relation of the noise temperature of a receiver as a function of the Y-Factor:

$$T_N = \frac{T_H - Y \cdot T_C}{Y - 1} \tag{3.10}$$

The implications of this last equation, related in particular to the concept of *Gain Compression*, will be reported in more detail in the next section.

3.3.4 Role of Y-Factor and T_N in Gain Compression

The Y-Factor, as already stated above, can be used to measure the T_N and, as it will be introduced in this section, the Gain of a radiometer too, both while in its the linear regime. Although, when applied to the concepts of Gain Compression and Amplification Curve just discussed, the Y-Factor acquires a new function: it can be employed to indirectly verify the *Linearity* of a receiver, i.e. wether it works in the linear regime rather than inside the compression one. Determining this information is of utmost importance, since the primary scope of the Y-Factor, finding the receiver's Noise Temperature, can be fulfilled only if the instrument works in its linear regime.

To proceed with the reasoning, it is necessary to manipulate the Amplification Curve in a new form: by applying the Johnson-Nyquist Law (Eq.3.3), for which $P \propto T_{phys}$, such Amplification Curve can be expressed as the visual expression of the relation P_{out} vs T_{phys}, i.e. the power coming out from a receiver versus the physical temperatures of the sources related to their powers, taken as inputs by the receiver itself. With this amplification curve new form, as

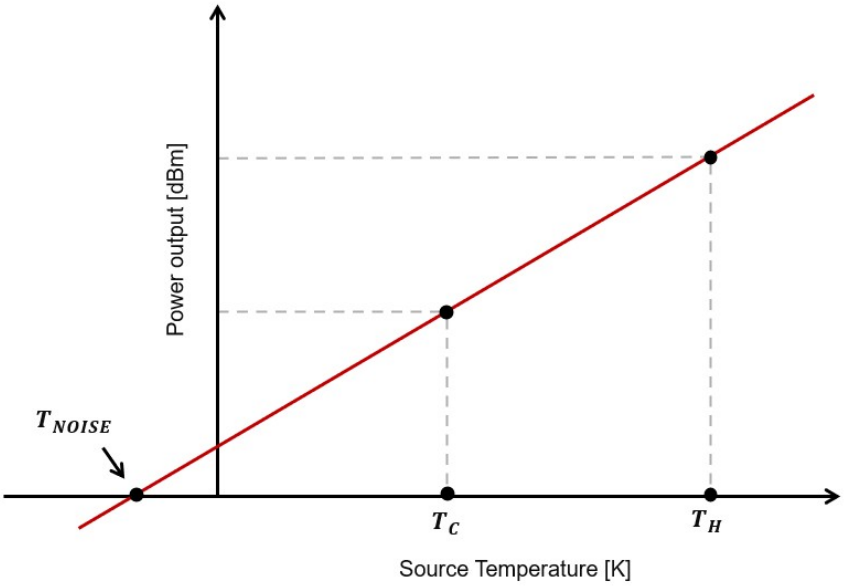

Figure 3.5: The T_N as the intercept of the straight line passing through the two test temperatures, hot and cold, with the Amplification Curve x-axis (turned into an array of sources temperatures instead of input powers).

displayed in Fig. 3.5, the T_N is none other than the intercept on the negative x-axis (now hosting temperatures) with the straight line passing through the two other temperatures appearing in Eq. 3.10 , T_H and T_C.
In order to better constrain the T_N resulting from this method, a wider set of temperatures not only would efficiently serve that purpose, but would make the computations of a Y-Factor for each combination of temperatures couples possible. Having said so, the correlation within Linearity study, Y-Factor and Noise Temperature is straightforward: in case of Linearity (Amplification Curve in linear regime), all the T_N values resulting from each of those Y-Factors should be comparable within the errors, highlighting the same intercept for each of the theoretical lines generated by the all the individual combination of the temperatures pairs, thus denoting the same *angular coefficient* among them all. For what concerns the case of Compression, most of the lines would instead end up in very scattered intercept values of the x-axis. This concept can be clearly visualized in Fig. 3.6.

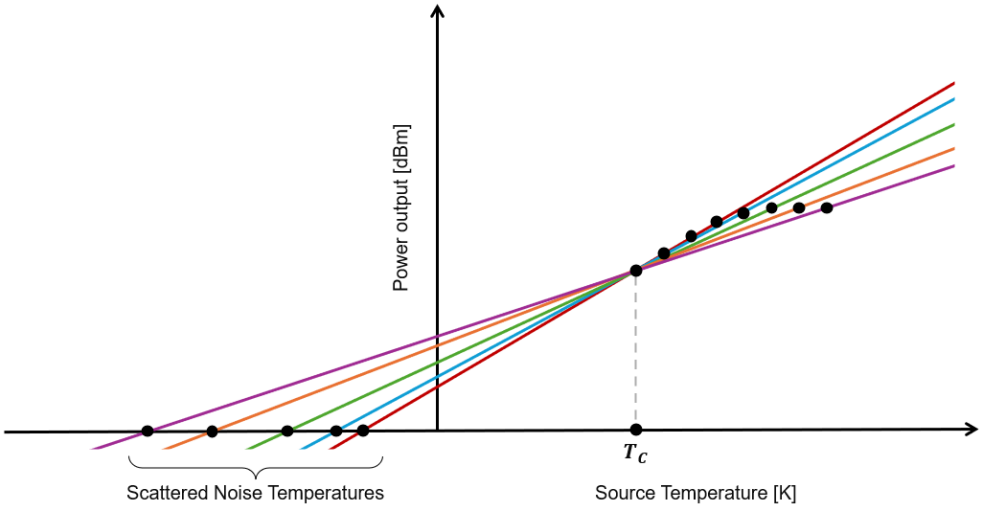

Figure 3.6: The effect of scattering of the T_N values resulting from a set of temperatures in the compression region. For the sake of visual clearness, instead of drawing a line for each of the combination of temperatures of a given set, the ones displayed are related to the pairs of all the temperatures coupled with the T_C only, so (T_C, T).

To conclude with, the last underlying concept is the slope of the straight line communal to all the temperatures sitting on the linear region and consequently identifying the system's T_N (the linearity is thus assumed): its very angular coefficient is exactly the Gain value G appearing in Eq. 3.1b, computed, so, thanks to the Y-Factor. Once both T_n and G have been thus graphically obtained, as it has been stated at the end of Sec.3.1, the measured value of P_{out} is then enough to properly decouple the artificial noise of the receiver from the real astrophysical signal, thus marking a final result in the radiometer characterization.
Lastly, it is noteworthy to explain what is really meant for the linearity study of an entire receiver: in the case in which a combination of active and passive elements are connected in a complex *RF Chain*, the Linearity which has to be tested is the one of the entire receiver and not only of the single component. In the receiver developed and tested in this work, the only internal components affecting their linear responses are the LNA and the Detector Diode: it is for this reason that the overall linearity of the EBB2 receiver must be checked in the area of input powers hosting both the LNA linear region and the above mentioned Detector Diode square-law region, has it will be treated in further detail in Sec.4.3.5.

3.4 The Vector Network Analyzer

The Vector Network Analyzer (VNA) showed in Fig.3.7 is laboratory instrument which is able to fully characterize a *Device Under Test*, or *DUT*, or rather to examine its response to a signal emitted by the VNA itself, which passes through it. The DUT can be a single RF component as well as both the entire RF chain of the receiver or composite parts of it, depending on the kind of analysis performed. The overall system of the DUT connected to the VNA ports is called Network and, depending on the number of ports included in the test, it can be called in different ways: if just one is employed, then it is the case of a One-Port Network (case of the EBB2 receiver's Horn characterization); if two of them are considered, then the system gets called Two-Ports Network and represents the most commonly used configuration, as it serves as basic building block to the expansion to larger networks [36](all the other characterizations in this work have been carried in Two-Ports Network setting).

The full characterization of a 2-Port network DUT is done by measuring the so called Scattering

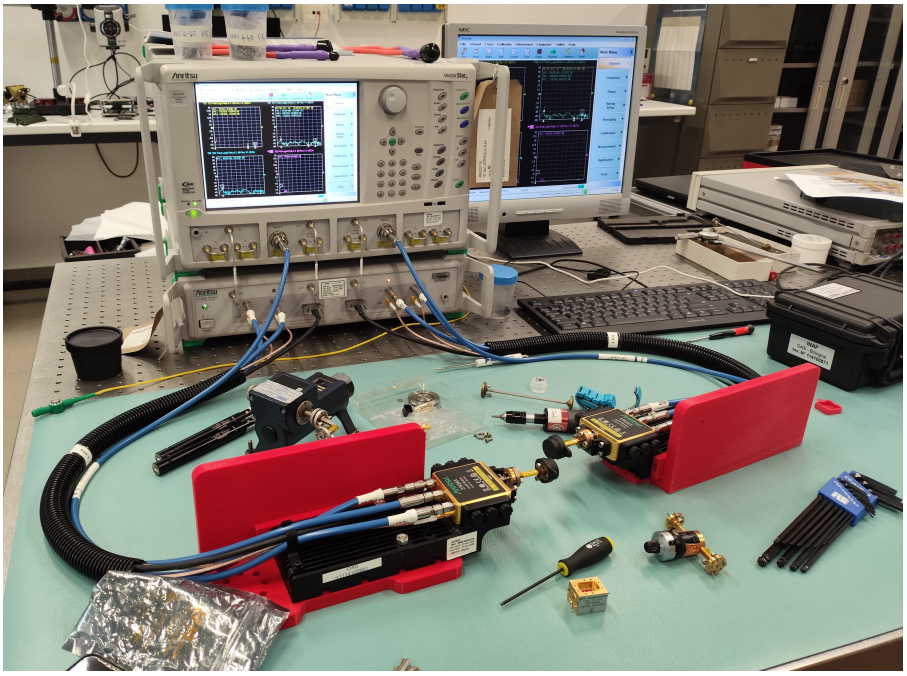

Figure 3.7: The *Vector Network Analyzer*, or *VNA*. The two red arms connected to the main instrument are the two ports, Port 1 (left) and Port 2 (right) through which a signal is injected in a given DUT.

Matrix, whose elements are the Scattering (or S-) parameters. The VNA injects and measures the signal at the two ports of the DUT during a frequency sweep in the bandwidth of interest and, in principle, this signal can approach each port in two different directions: inward or outward. As can be understood from Fig.3.8, the two inward directions are labeled by the

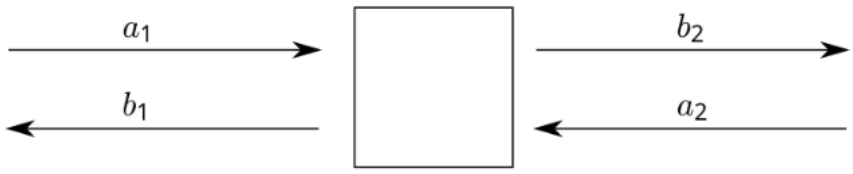

Figure 3.8: The *Two-Port Network*: the a vectors represent the incoming waves direction, while the b ones the exiting ones.

parameters a_1 and a_2, respectively at *Port* 1 and at *Port* 2, while the outward directions are, namely, b_1 and b_2. Those four parameters are correlated to the above-mentioned *Scattering Matrix* as follows:

$$\begin{pmatrix} b_1 \\ b_2 \end{pmatrix} = \begin{pmatrix} S_{11} & S_{12} \\ S_{21} & S_{22} \end{pmatrix} \begin{pmatrix} a_1 \\ a_2 \end{pmatrix}. \tag{3.11}$$

This matrix, a 2×2 one in the case of a 2-Port Network, is well characterized by the fundamental S-parameters: S_{11}, S_{12}, S_{21} and S_{22}. Thanks to this mathematical feature, the VNA is able to draw a relationship between all the signals passing through the Network, thus building a

direct link between the incoming and the exiting waves through the following expansion of the Scattering Matrix into equation forms:

$$\begin{aligned} b_1 &= S_{11}a_1 + S_{12}a_2 \ , \\ b_2 &= S_{21}a_1 + S_{22}a_2 \ . \end{aligned} \tag{3.12}$$

By now defining the a, b variables as the so called *incident voltage waves*, $a_1 = V_1^+$, $a_2 = V_2^+$ and *outgoing/reflected waves*, $b_1 = V_1^-$, $b_2 = V_2^-$, let's discuss the concept behind each of the S-parameters:

- $S_{11} = b_1/a_1 = V_1^-/V_1^+$, or **input port voltage reflection coefficient**. Namely, is the signal exiting from the input *Port* 1 normalized to the one incoming to the same port. If $b_1 = a_1$, so $V_1^- = V_1^+$, no signal passes through the network, resulting in a total reflection;
- $S_{21} = b_2/a_1 = V_2^-/V_1^+$, or **forward voltage gain**. That is the ratio between the wave exiting from *Port* 2 and the incoming one to *Port* 1. It represents the response of the network to a signal passing through it, carried in the forward direction (upper arrows path in Fig.3.8);
- $S_{12} = b_1/a_2 = V_1^-/V_2^+$, or **reverse voltage gain**. It follows the same concept of its counterpart S_{21}, but this time with inverse path direction through the network (lower arrows path in Fig.3.8);
- $S_{22} = b_2/a_2 = V_2^-/V_2^+$, or **output port voltage reflection coefficient**. It is again the ratio between the outgoing and the incoming signal from the same port, as for S_{11}, but this time considering the output *Port* 2. If the incident voltage wave equals the outgoing/reflected one, a total reflection will take place in this case too.

Thanks to these four parameters it is possible to define several quantities, useful to better understand the functioning and the physics behind the VNA. The first one is the fundamental (**Complex**) Gain, a complex number expressed now as the forward voltage gain:

$$G = S_{21} = \frac{b_2}{a_1} = \frac{V_2^-}{V_1^+} = Re(G) + i \cdot Im(G) \ ; \tag{3.13}$$

It is consequently possible to define the *scalar linear gain* both in decimal notation,

$$|G| = |S_{21}| \ , \tag{3.14}$$

as well as in the logarithmic one, expressed in dB units:

$$g = 20 \log_{10} |S_{21}| \ dB \ . \tag{3.15}$$

The second noteworthy parameter is the *Input* (or *Output*, depending on which port is taken into account) *Return Loss*, i.e. the effective percentage of outgoing signal w.r.t. the incoming one in a case of reflection by the port considered:

$$\begin{aligned} RL_{IN} &= 10 \log_{10} \Big| \frac{1}{S_{11}^2} \Big| = -20 \log_{10} |S_{11}| \ dB \ , \\ RL_{OUT} &= 10 \log_{10} \Big| \frac{1}{S_{22}^2} \Big| = -20 \log_{10} |S_{22}| \ dB \ . \end{aligned} \tag{3.16}$$

If the incident voltage wave is equal to the outgoing/reflected one, the reflection is total and characterized by a *null Return loss*.

Chapter 4

The Solaris EBB2 Receiver

This chapter presents the Elegant Bread Board #2, EBB2, Receiver developed within the Solaris project. An initial description of its RF components is followed by the core process of VNA-based characterization of the receiver's individual RF components, with the extraction of their main S-parameters and in particular of the S_{21}, or Gain, which allowed the construction of the receiver's fundamental preliminary gain budget. Thereafter, the optimal positioning order of the components, the receiver Response Curve and its Linearity regime have been investigated and, finally, the receiver noise temperature has been derived through dedicated python scripts specifically developed for this work, thus compared with the initial expectation provided by the preliminary budget itself.

4.1 EBB2 Receiver's configuration

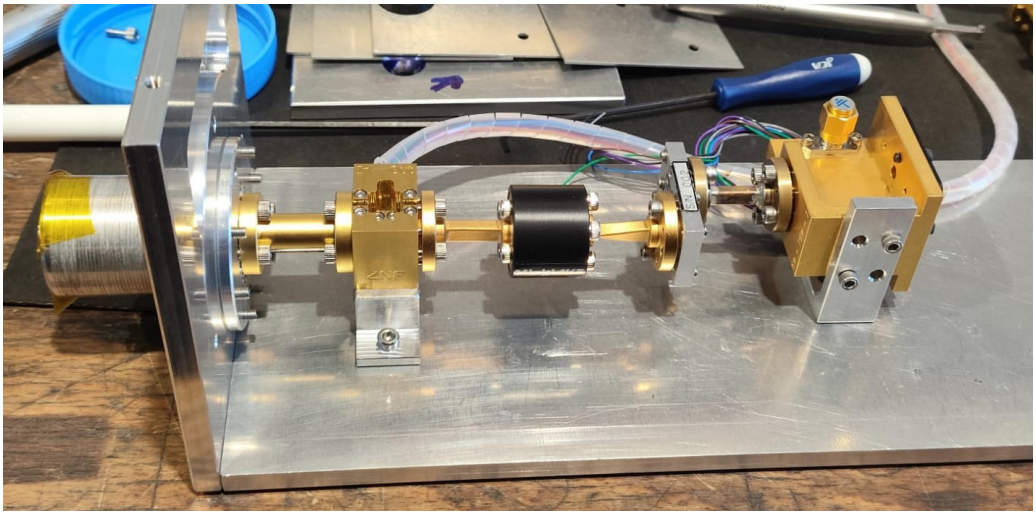

Figure 4.1: The EBB2 Receiver RF chain and its block diagram: the horn has been developed in Milano laboratories and it is the one which protrudes from the aluminum box containing the entire structure; it is then attached to the circular-rectangular transition and, in sequence, to the LNA, Isolator, Band Pass Filter, a small waveguide named here WG2630 and, lastly, to the Detector Diode.

The EBB2 Receiver configuration, displayed in Fig.4.1, is composed of a Feed Horn, designed for ALMA band 2 receiver [52] by the INAF-Osservatorio Astrofisico di Arcetri and manufactured at the University of Milan, followed by a commercial circular-to-rectangular WR10 waveguide transition, which collects the incoming radiation from the Horn (circular output), to a standard rectangular waveguide one, so to make the signal flow in the rest of the RF

Chain, characterized by the same cavity shape. Those two elements are then followed by the Low Noise Amplifier manufactured by the Low Noise Factory company, called LNF 005H, and the commercial Isolator, both leading the thus amplified radiation in a privileged direction to the Band Pass Filter, or *BPF*. Since the latter could produce a small amount of signal reflection, thus producing a stationary wave bouncing in the receiver, the LNA is shielded from this effect by the isolator, placed between them for this reason. All the chain described so far is then connected to the Detector Diode by the waveguide named "WG2630" after its length of 26.30 mm.

4.2 EBB2 Receiver's Box Design

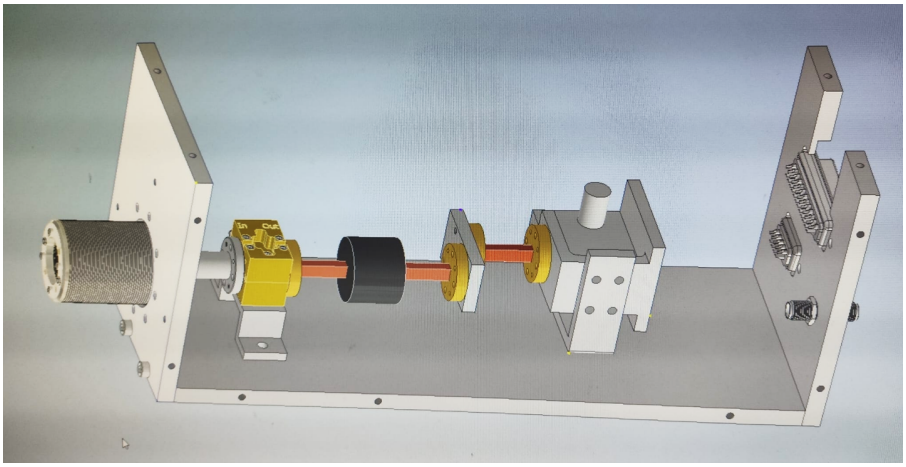

Figure 4.2: The ©Autodesk Inventor 2020 Receiver design inside its custom-designed and here opened aluminum box.

The receiver's aluminum box , shown in Fig.4.2, has been entirely designed during this work using the with ©Autodesk Inventor 2020 software. All the pieces have been specifically realised based on the size and structure of the EBB2 RF chain. For each RF element composing the chain, its exact dimension has been measured or acquired from the producer's relative datasheet (where possible), to be able to perfectly reproduce on the 3D CAD software the exact dimension of the receiver and, consequently, to build a well-fitting box where to keep it stored and mounted on the antennas for observations.

4.3 EBB2 Receiver's VNA analysis

4.3.1 Characterization of the single RF components

The first step to build a so called Gain Budget, an essential preliminary set of data to a receiver which will be treated in the next section, is to characterize each single RF component with the VNA. As already introduced in Sec.3.4, with these measurements, the S-Parameters composing the Scattering matrix of each element of the RF Chain can be ensured, thus isolating their individual S_{21}-parameter, or Gain. For this procedure, the VNA has been calibrated every morning: the calibration is a key procedure which generally lasts a day before incurring in small instrumental drifts, and it is necessary to approve a set of working values in which an analysis can be performed. For the EBB2 Receiver case, all the calibrations included the setting of:

- **Frequency working range**: $[67, 125]\,GHz$, wider than the bandwidth used in ALMA Band 2 receiver mentioned at the beginning of Sec.2.3;
- **Number of points**: it determines the resolution in frequency. X points has been set for this work;
- **Number of Ports**: 1-Port Network for the Horn characterization, 2-Ports Network for the remaining components;
- **Ports' Power Level**: amount of VNA Ports' output absolute Power (dBm units). A value of $-30\,dBm$ has been chosen for the reasons explained in Sec.4.3.4 and Sec.4.3.5;
- **Calibration Method**: *TRL* calibration method [36], the standard one for the *WR*-kind of waveguide, i.e. Waveguide Rectangular (referring to the rectangular shape of the components' cavity in which the signal flows). TRL stands for "Thru-Reflect-Line", i.e. the three procedures which has to be performed to conclude the calibration process. In particular, the waveguides mounted in the EBB2 receiver are *WR-10*, which are characterized by a $1:2$ ratio within width and height of the cavity, thus $0.10'' = 2.54\,mm$ long and $0.05'' = 1.27\,mm$ high (units of inches).

Reported below, the list of the EBB2 receiver's RF components and the resulting VNA characterization plots, which are arranged as S_{11}-parameter (top-left), S_{12}-parameter (top-right), S_{21}-parameter (bottom-left) and S_{22}-parameter (bottom-right). For what concerns passive components, both reverse and forward gains, namely S_{12} and S_{21}, are actually losses, with a negative dB gain value: as already anticipated, they act thus as attenuators. On the other hand, the S_{21} of the LNA, being an active component, is positive, meaning that the signal is amplified rather than attenuated. So, the gain term is used regardless wether it represents an attenuation or an amplification.

Horn - Transition WG

Since the horn antenna is a radiating element, it has been characterized in a 1-Port Network VNA configuration by connecting it only to the Port 1 through the Transition WG (needed to match the horn circular cavity with the VNA rectangular one). In Fig.4.3, the VNA output S_{11}-Parameter only, as well as an image of the two RF components and its characterization block scheme.

Transition WG

Component Data:

- Eravant, WR-10 to Circular Mode Transition
- Part number: SWT-101 10-SB
- Serial number: 45996-01

For this item, since its VNA characterization alone is not possible, it has been necessary to couple it to a completely equal piece, connected to it in the other way around. The VNA ports have rectangular cavities and for this reason the overall system of two consequent equal transitions guaranties both input and output to Port1 and Port2 WR-10 type, leaving the two circular ones in the middle. In Fig.4.4, the VNA output S-Parameters, as well as an image of the two RF components connected. A visual of their two different cavity extremities is provided

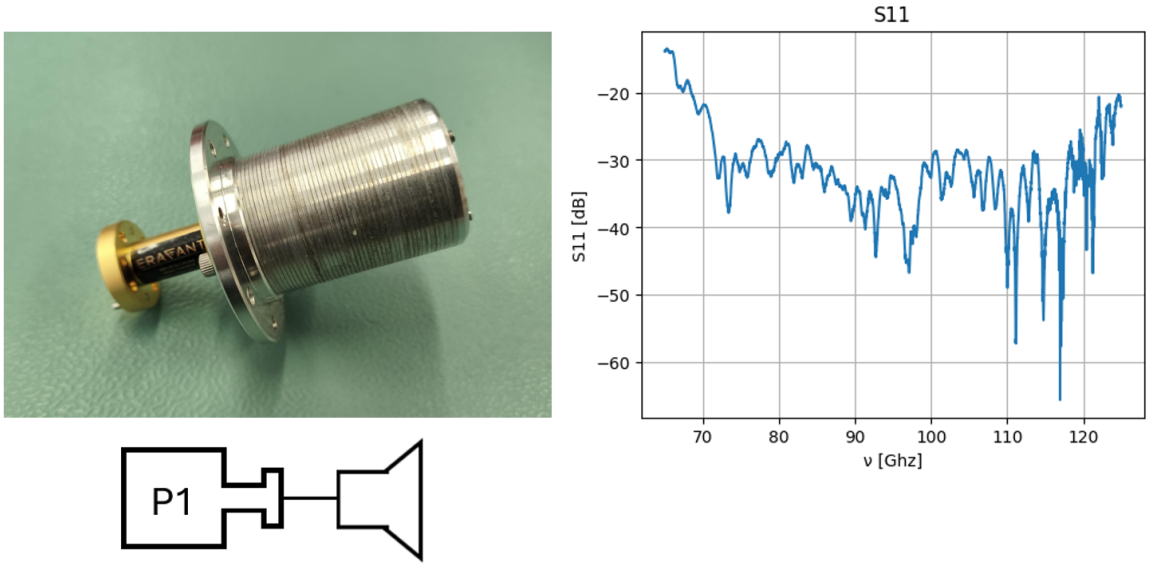

Figure 4.3: Left: Horn - Transition WG image and characterization block scheme; **Right**: VNA output S_{11}-Parameter, resulting from its 1-Port Network characterization.

too. The Gain of the single Transition WG can be extracted by dividing by two the average one of the S_{21}-Parameter resulting from the above-mentioned system's characterization.

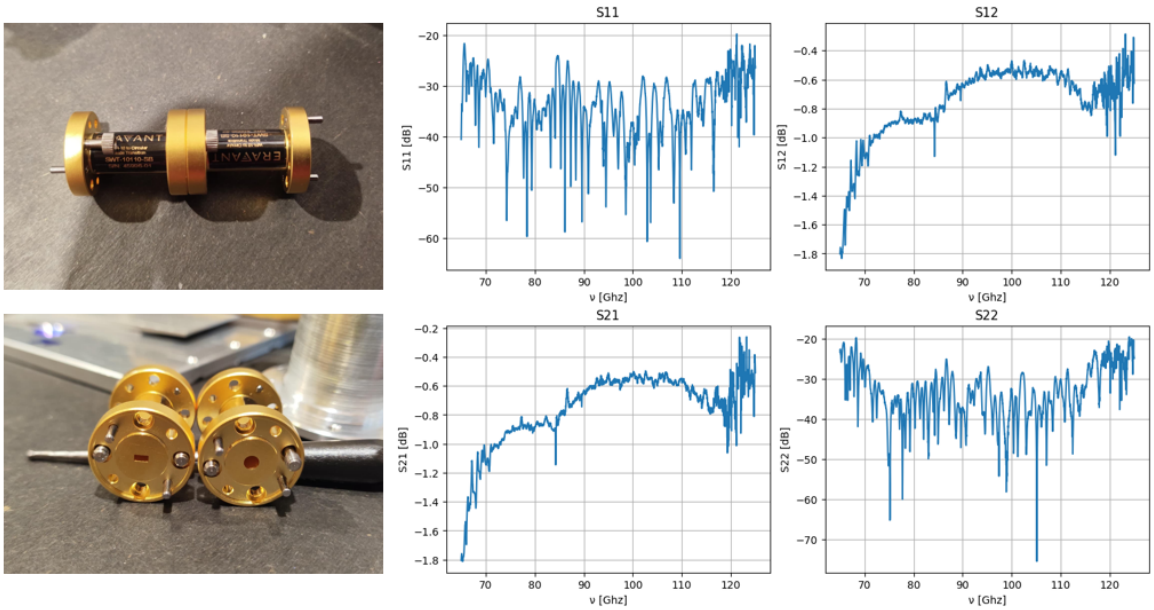

Figure 4.4: Left: the two Transition WG connected together and the view of their ends' cavities two different shapes. **Right**: the RF components' pair 2-Ports Network resulting S-parameters.

Isolator

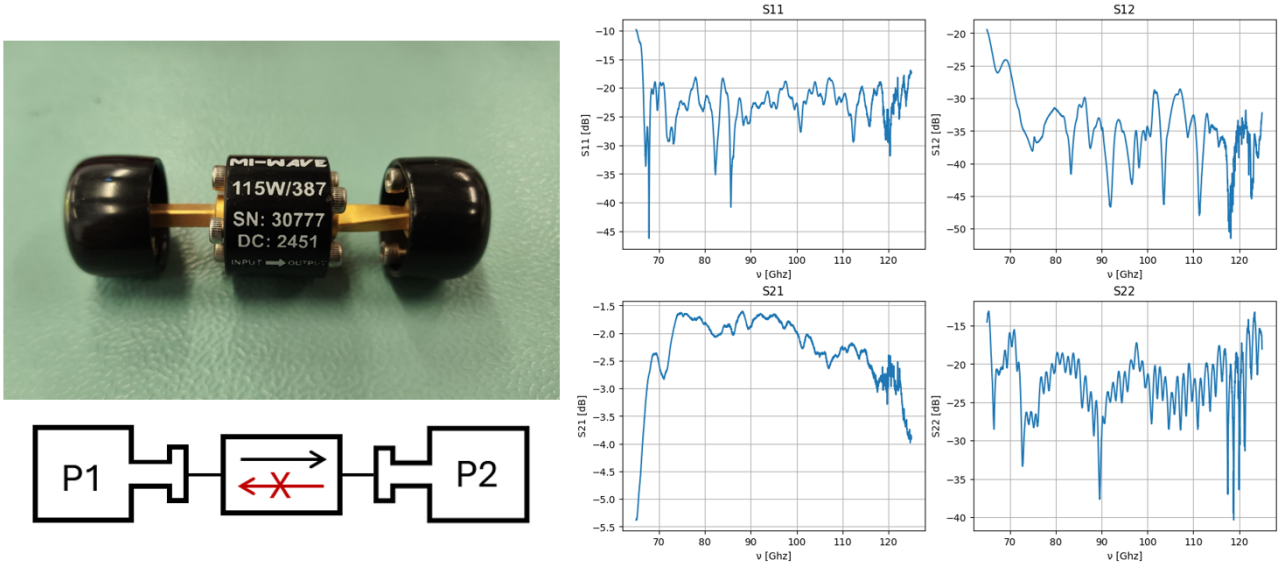

Figure 4.5: **Left**: Isolator image and characterization block scheme; **Right**: VNA output S-Parameter, resulting from its 2-Port Network characterization.

Component Data:

- Isolator Mi-Wave
- Part number: 115W/387
- Serial number: 30777

Fig.4.5 shows the image of such RF component, the block scheme of its 2-Port Network characterization and finally its resulting S-parameters. The behavior of the Isolator is well visible by observing the plot of the S_{21}- and S_{12}-parameters: the former, i.e. the Forward Gain shows the typical behavior of a passive components, thus letting the signal thru in the permitted direction dictated by the components itself with a minimum degradation of $\sim -2\,dB$, on average; the latter (Inverse Gain) shows instead the isolation effect: the signal, while trying to pass through the forbidden direction of the device gets attenuated by $\sim -35\,dB$, i.e. a power ~ 3162[1] times lower.

Band Pass Filter

Component Data:

- Pacific Millimeter Products W-Band Band Pass Filter
- Serial number: 002

The picture of The EBB2 receiver's Band Pass Filter, as well as the block scheme of its 2-Port Network characterization and its resulting S-parameters are displayed in Fig.4.6. Both the Gains plots show the expected behavior: all the frequencies not belonging to the BPF working range, i.e. $[80, 110]\,GHz$, gets attenuated by a factor of $\sim -50\,dB$ (a factor $\sim 10^5$), thus

[1] By the definition of decibel: $dB = 10 \cdot log_{10}(P_1/P_2)$, so $(P_1/P_2) = 10^{dB/10}$

pointing out the actual BPF most optimal and responsive frequency range of $[88, 101]\,GHz$, information which will be extensively exploited in the next steps of this work. As a matter of fact, the reflection parameters S_{11} and S_{22} show a perfect reflection effect outside the frequencies of interest, with an almost 0-level Return Loss, while instead the conduction of the signal is ensured for the same optimal range mentioned earlier. There, an irregular spike of power can be observed at $\nu \approx 114\,GHz$, later identified as a VNA instrumental defect.

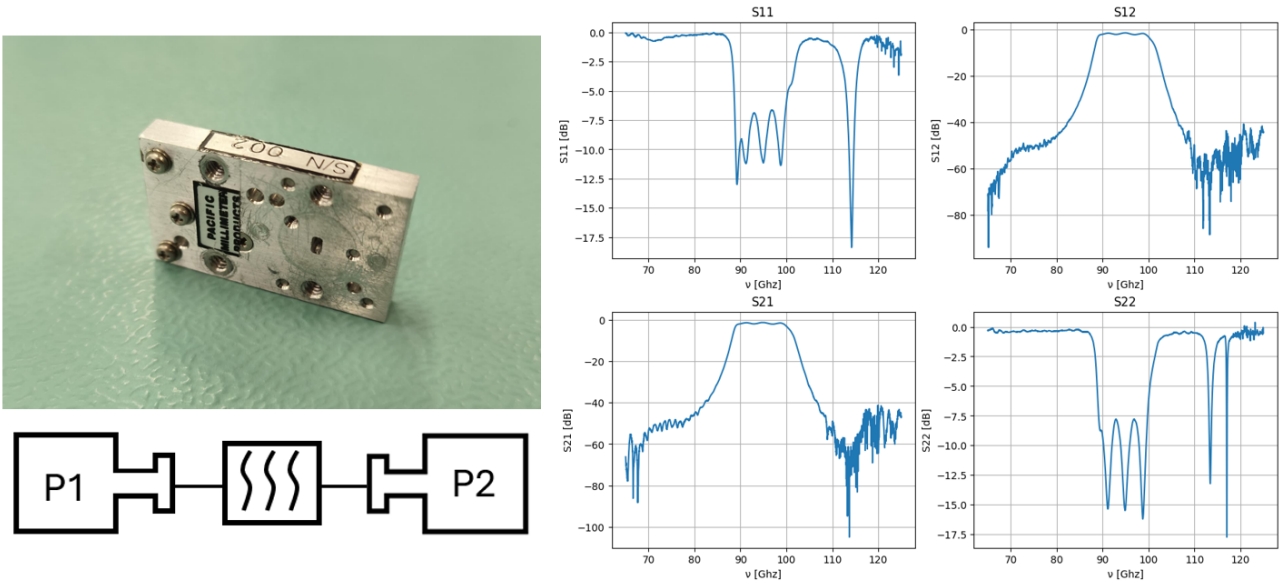

Figure 4.6: **Left**: BPF image and characterization block scheme; **Right**: VNA output S-Parameter, resulting from its 2-Port Network characterization.

Waveguide "WG2630"

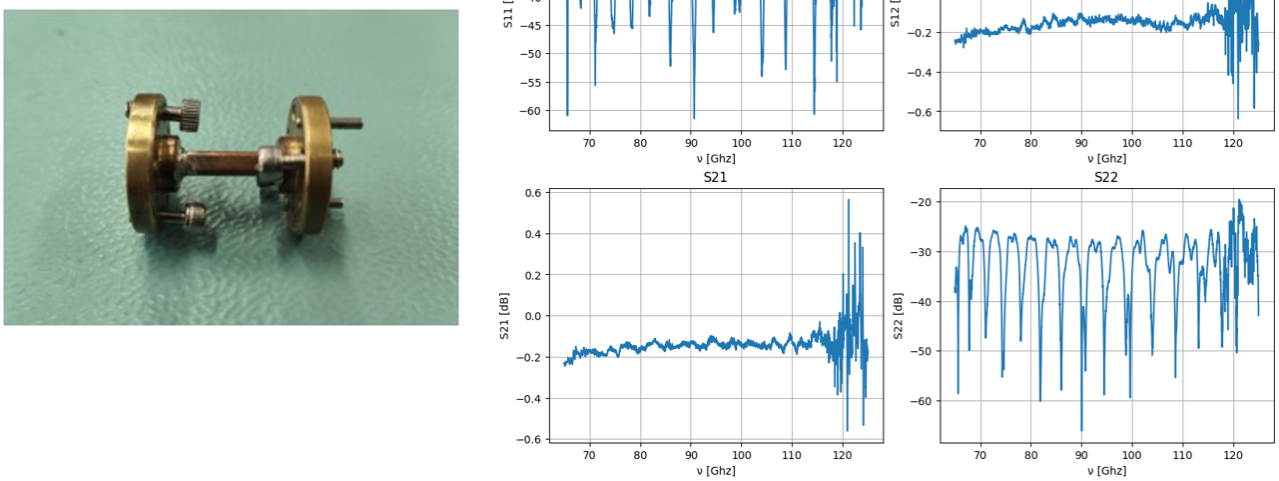

Figure 4.7: **Left**: the WR-10 waveguide "WG2630"; **Right**: VNA output S-Parameter, resulting from its 2-Port Network characterization.

A straight Waveguide type WR-10, dubbed in this work as "WG2630" for his 26.30 mm length. Fig.4.7 shows its image and its 2-Port Network characterization result. The classical passive components' behavior can be observed from the Gains parameters, since a small mean degradation of the signal of $\sim 1.4\,dB$ can be observed. One more noteworthy feature is the small slope these two curves show at lower frequencies, caused by the *cut-off frequency* of the waveguide, $f_c = c/2a$, i.e. speed of light over twice the length of the WG cavity. As already introduced, WR-10 guides have $a = 2.54\,mm$, resulting in a $f_c = 59\,GHz$: so, closer to the left end frequency of the W-Band the WG is not in a regime of full propagation yet, thus presenting a slightly lower level of relative power w.r.t. the rest of the ν-range.

LNA and Detector Diode

The LNA (produced by the LNF, "$LNF-LNC65\_115WB$" Serial Number 005H) as well as the Detector Diode (VDI company, Serial Number WR10R9 1-49, 3-44) shown in Fig.4.8, have been both left out from this procedure, since their Forward Complex Gains were already provided in their commercial producer's datasheet. Their values are reported in the table containing the *preliminary budget* of the EBB2 Receiver, main topic of the next section of this work.

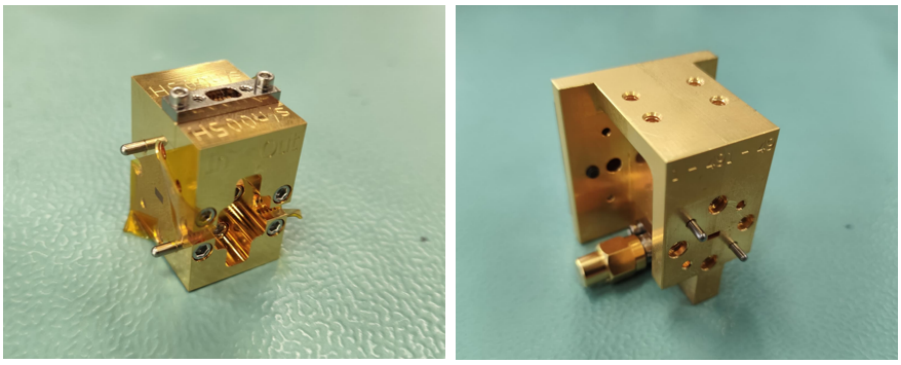

Figure 4.8: Left: EBB2 receiver's LNF Low Noise Amplifier; **Right**: EBB2 receiver's VDI ZBD Diode.

4.3.2 Preliminary Gain and Noise Budget

Now that each component has been characterized with the VNA, and thus their individual Gain values have been measured, a preliminary Gain and Noise Budget can be settled. This set of data represents the first approach to a cascade components architecture, providing a preliminary estimation of the overall receiver's Noise Temperature T_N and gain G.
In Tab. 3.1, the preliminary Gain and Noise Budget of the EBB2 Receiver is thus shown: it includes

- **Physical Temperature** of each RF component, PT;
- **Mean Gain values** in dB units;
- **Cumulative mean Gain**: the sum of all the Gains up to a given point in the RF Chain;
- **Mean Linear Gain**: obtained by the extraction of the Real and Imaginary part of the S_{21}-parameters through

$$G_{Lin,i} = \sqrt{Re(S_{21,i}) + Im(S_{21,i})}\,, \tag{4.1}$$

and then by computing the mean of all the $G_{Lin,i}$ values

- the **Noise Equivalent Temperature**, or *NET* (treated shortly);
- the **Cumulative NET**: sum of all the NET values up to a given point in the RF Chain.

Element	**PT** $[K]$	**Gain** $[dB]$	**Cumulat. Gain** $[dB]$	**Linear Gain**	**NET** $[K]$	**Cumulat. Noise** $[K]$
HORN	296	-0.100	-0.100	0.977	6.601	6.601
TR-WG	296	-0.369	-0.469	0.958	12.349	18.950
LNA	296	25.000	24.531	316.228	363.027	381.977
ISOLATOR	296	-2.058	22.472	0.789	0.207	382.184
BPF	296	-2.249	20.223	0.772	0.283	382.467
WG2630	296	-0.138	20.085	0.984	0.025	382.492

Table 4.1: The Gain Budget, containing sereval information about the single RF Component: Physical Temperature, or PT, all set to room temperature; the Gain; the Cumulative Gain, which is simply the sum of the Gain values of all the RF Elements preceding the one in analysis (included); the Linear Gain, in agreement with Eq. 3.15; the Noise Equivalent Temperature, or NET, computed by the action of all the preceding gains, according to Eq. 4.2; the Cumulative Noise, which is the sum of all the preceding NETs.

The Noise Equivalent Temperature (NET) derives from a physical property in the case of cascaded active and passive components, which is the case of the receivers' chains; in principle, along the signal's path, the collected radiation must pass through all the circuital elements composing the receiver itself, each one of them introducing their own noise (Eq. 3.3) and gradually decreasing the overall Gain of the system. That the noise introduced by each component gets cut down by the product of the Gains generated by all the elements preceding the one just crossed by the signal, or, in other words, cut down by the factorial of the second to last component's Gain encountered. This phenomenon can be described by the *Friis Formula* [17], i.e. a sum operation whose addends take into account the nature of the components themselves (active or passive). In the case of active components, the addend's numerator remains the Noise Temperature of the element, while if a passive one is considered, the quantity which will be divided by the factorial of the preceding gains will consist of the product between the physical temperature of the component, TP, and $(1-G)$, where G is its **Linear** Gain (always < 1, since most of the times, as already mentioned, passive components can only attenuate signals). All the Gains appearing in the Friis Formula on both the numerators, for passive components only, and denominators are intended as *Linear Gain* values, not the dB logarithmic one. Applying this concept to the EBB2 Receiver, i.e. Horn, Circular-Rectangular Transition waveguide, LNA, Isolator, BandPass Filter and the final waveguide 2630, each addend will be

- **Horn** (passive):
  $$NET_{horn} = PT_{horn}(1 - G_{horn}) \, ;$$
- **Transition WG** (passive):
  $$NET_{TRwg} = \frac{PT_{TRwg}(1 - G_{TRwg})}{G_{horn}} \, ;$$
- **LNA** (active):
  $$NET_{LNA} = \frac{T_{n,LNA}}{G_{horn} \cdot G_{TRwg}} \, ;$$

- **Isolator** (passive):
$$NET_{isol} = \frac{PT_{isol}(1 - G_{isol})}{G_{horn} \cdot G_{TRwg} \cdot G_{LNA}} ;$$

- **BPF** (passive):
$$NET_{BPF} = \frac{PT_{BPF}(1 - G_{BPF})}{G_{horn} \cdot G_{TRwg} \cdot G_{LNA} \cdot G_{isol}} ;$$

- **WG2630** (passive):
$$NET_{wg2630} = \frac{PT_{wg2630}(1 - G_{wg2630})}{G_{horn} \cdot G_{TRwg} \cdot G_{LNA} \cdot G_{isol} \cdot G_{BPF}} ,$$

this resulting in the Friis Formula for the EBB2 receiver:

$$T_{noise,tot} = NET_{horn} + NET_{TRwg} + NET_{LNA} + NET_{isol} + NET_{BPF} + NET_{wg2630} \tag{4.2}$$

The cumulative NET value of the overall system will be completely dominated by the presence of the LNA and by the Horn and Transition WG too, but both to a lesser degree w.r.t. the amplifier. This is mainly due to the fact that the Horn and the Transition WG are the first two RF components of the Chain: the Horn wont be affected by any Gain, while the Transition WG by the very small linear Gain value of the Horn itself, with a overall cumulative NET of $\sim 19\,K$. However, the very dominant effect is provided by the LNA since, by being an active component, not only it provides a positive and high Gain, but also a NET ($NET_{LNA} = T_{n,LNA}/(G_{horn} \cdot G_{TRwg})$) with a datasheet-provided $T_n = 340\,K$, which gets barely affected by the two preceding small linear Gains. In conclusion, as already anticipated, thanks to this preliminary Gain and Noise Budget it is possible to set an expectation on G and T_N of the EBB2 Receiver, resulting in $T_N \approx 382\,K$ and $G \approx 20\,dB$. These numbers shall be compared with the actual measured ones, further provided.

4.3.3 Elements positioning order

The first step of EBB2 Receiver VNA analysis has concerned the Isolator position in the RF chain. Usually, LNAs, detectors and filters outside the working band, exhibit a poor return loss creating standing waves in the RF chain. Those waves degrade the signal and could also damage some components in case of relatively high power. In the case of Solaris receiver the isolator could be placed between the LNA and the BPF (Configuration A), or alternatively just after the BPF in between the BPF and the Detector (Configuration B). The way to find the best out of the two is to test the above mentioned configurations, both displayed in Fig. 4.9, at the VNA, thus checking if significant differences emerge.
In Fig.4.10, the comparison between the S-parameters of the two configurations is displayed. Here, on both set of plots, the S_{11} is shown at the top-left position, the S_{12} at the top-right, the S_{21} at the bottom-left and, finally, the S_{22} at the bottom-right one. Clearly, since A and B are one the inverted case w.r.t. the other, while both forward and reverse voltage gains remain the same in the matrix of pictures, the two Reflection Coefficients visualization is instead swapped (S_{11} curve pattern of Configuration B can be found again in the S_{22} parameter of Configuration A, as well as for its S_{22} on the left, in Configuration A's S_{11}). Thus, in the incoming dissertation of those S-Parameters, only Configuration B will be treated, implicitly intending this just stated inverse symmetry of the reasoning. To begin with the input port voltage reflection coefficient, S_{11}, it is possible to observe the expected behavior of a receiver which includes a BPF: as explained in Sec.4.3.1, the function of this RF component is to strongly reflect all the signal emitted in the frequencies which do not belong to its working

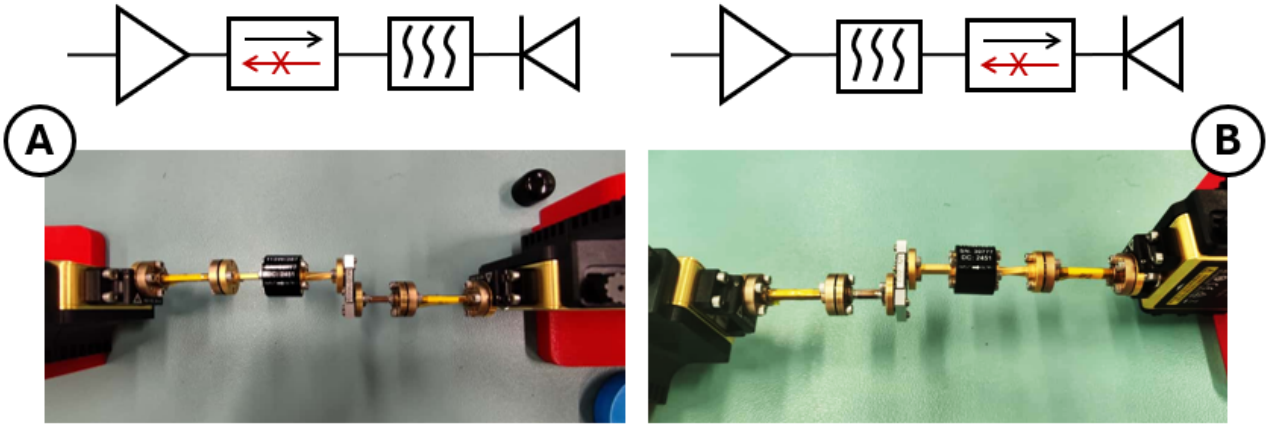

Figure 4.9: Left: block diagram of Configuration A (LNA, Isolator, BPF, Diode) and actual picture of the DUT sufficient to conduct the VNA analysis regarding the positioning order of its RF components (Isolator, BPF, WG2630); Right: block diagram of Configuration B (LNA, BPF, Isolator, Diode) and actual picture of the DUT (WG2630, BPF, Isolator).

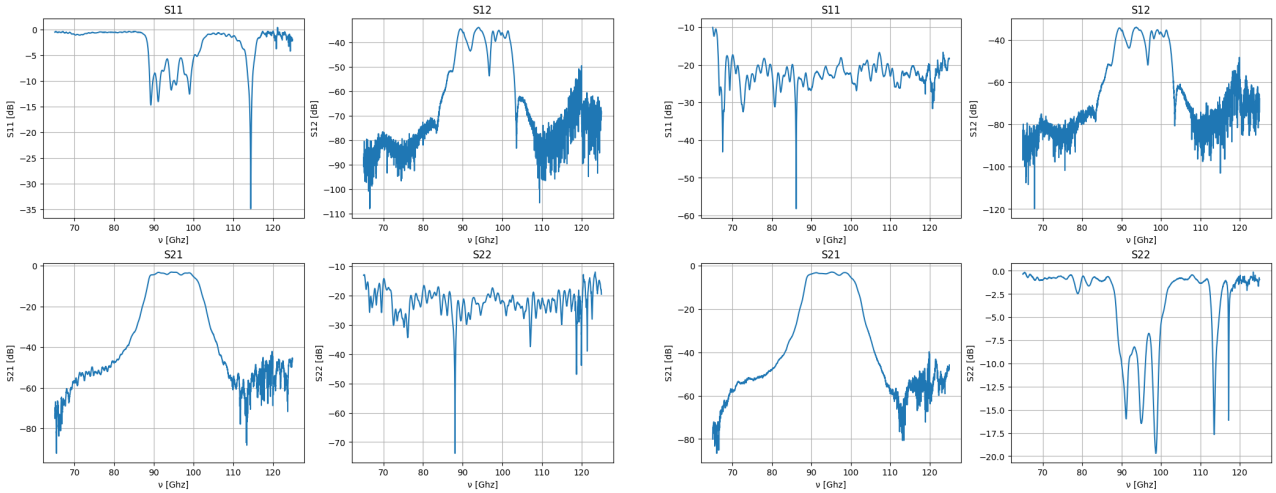

Figure 4.10: Left: VNA measurements of the S-parameters of the Configuration B. **Right**: VNA measurments of the S-parameters of the Configuration A. By the comparison of the plots, no significant change in the values of the S-parameters can be distinguished, thus denoting the two configurations' interchangeability.

range and, thus, to let through all the others. The Return Loss is, indeed, null ($\sim 0\,dB$) in the windows $[65, \sim 86]\,GHz$ and $[\sim 104, 125]\,GHz$, resulting in the total reflection of all these undesired signals. As a consequence, the forward gain, S_{21}, which represents the signal passing from Port1 to Port2, is dominated by this same behavior of the filter. Futhermore, given the response of the Isolator described in Sec.4.3.1, the behavior of the BPF is not visible in the S_{22} curve, since the signal traveling in the Port2-Port1 direction gets heavily attenuated by such component, thus presenting an almost flat trend. However, generally speaking, no significant discrepancies in the general shape of those curves can be noticed from configurations A and B and, therefore, both of them are well interchangeable for this work purposes. To conclude with, Configuration A has finally been chosen for mechanical integration reasons only, regarding the receiver orientation in its storage inside its box.

4.3.4 Response Curve

The Response Curve is a method which highlights the correlation between the input signal flowing into the RF Chain and its output, i.e. what comes out from the Chain itself, analyzed at each single frequency belonging to the working range (usually the one of the Filter). The two correlated units of measure, Input Unit and Output Unit, are based on the configuration under test, i.e. rather the Chain does not include the Detector Diode, or if it does. In the first case, the configuration can be plugged in the VNA Port1 as input (so the Input Unit is in dBm), while the output will be the absolute power measured at each frequency detected by the Power Meter, connected at the end of the RF Chain. To proceed with this measurement, the dynamical range of detection of the above mentioned device must be taken into account, since its proper functioning is guaranteed for absolute powers in the range $[-35, +20] dBm$. By now employing a rough approximation of the single elements' Gains in the preliminary Gain budget, it is possible to decide the best attenuation level so to work in the aforementioned working range: VNA Port1, $-30 dBm$; 90° twist wg, $\sim -1 dB$; LNA, $\sim +30 dB$; Isolator, $\sim -1 dB$; BPF, $\sim -1 dB$; WG2630, $\sim -1 dB$. By now adding up all those values, without any source of attenuation, the incoming power entering the Power Meter would be approximately between -4 and -6 dBm. Therefore, an attenuation of $-10 dB$ is enough to fulfill the scope: a power between $-14, -16 dBm$ can be perfectly read by the Power Meter and represents a safe value too, so to not getting close to the LNA's RF input drive level, i.e. the maximum dB signal the component is able to work with. Both the configurations stated above can be observed in Fig. 4.11. The Response Curve is thus a process which requires the power estimation at each

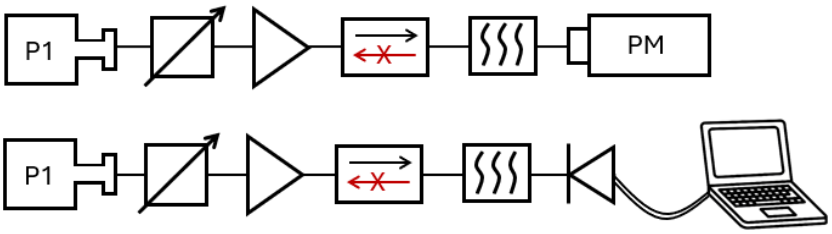

Figure 4.11: Top Configuration: Response Curve Configuration plugged to the VNA, signal detected by the Power Meter - VNA's P1, Attenuator, LNA, Isolator, BPF, Power Meter; Bottom Configuration (hypotetical): Response Curve Configuration plugged to the Noise Generator, signal detected by the Detector Diode, then digitalized - VNA's P1, Attenuator, LNA Isolator, BPF, Diode, Digital Multimeter.

frequency belonging to the working range: while the standard functioning of the VNA concerns a sweep of a band of frequencies, for the aforementioned aim it can be set to the so called *CW mode*, which is able to examine one input frequency at a time, thus collecting simultaneously the Power Meter power level detection at each one of them in the BPF's filtered band. Fig. 4.12 shows the result of such a process and, by observing it, it is possible to observe a general higher response of the RF Chain to a range of frequencies corresponding to $\sim [88, 101]\, GHz$, with a peak of power at $91\, GHz$. By performing a weighted average operation, with as accounted weights the dBm level for each ν, an optimal individual frequency of $94\, GHz$ has been found and then assumed as central most responsive ν-value of the filter. This information will be particularly important in the last chapters of the Solaris Optical Models. Finally, Tab.A.1 , which contains the numerical values of the Power Meter that have generated such result, can be found in appendix. Furthermore, even if only the method just explained has been applied in this work, the second way in which, theoretically speaking, the Response Curve of the entire

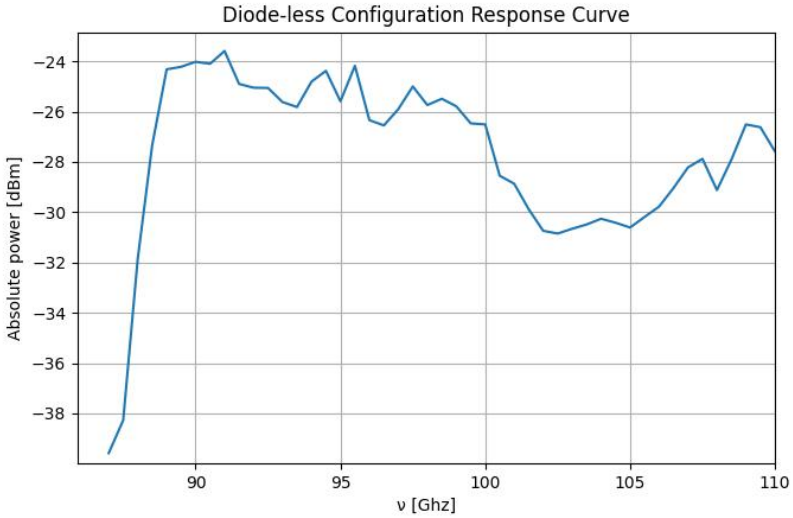

Figure 4.12: The Response Curve resulting from Fig. 4.11 Top Configuration, taken in the VNA CW mode of the BPF's frequency range $80 - 110\ GHz$.

RF Chain could be performed, Detector Diode included, would involve the VNA plugged into the input extremity while, this time, the output would be recorded in Voltages by a digital acquisition electronics cabled directly to the Diode. In this scenario, the Response Curve refers on how the Receiver turns the input absolute power (Input Unit) into Output Voltages (Output Unit). The two configurations treated in this section can be observed in Fig4.11.

4.3.5 Linearity

It is now time to test the already introduced concept of Linearity on the EBB2 Receiver. The linearity of an active RF element is thus studied through the already discussed Y-Factor. This is for what concerns single elements; when they are connected in a complex RF Chain, the Linearity of the overall configuration has to be checked (dominated thus by the linearity of its single active components). The two methods which are about to be investigated, can be both applied to analyze not only the Linearity of the RF Chain up to the WG2630, so without the Detector Diode (Y-Factor dominated by the only active element of this "truncated" configuration: the LNA), but also to check the absence of compression for the entire chain, so from the amplifier to the diode, where the Linearity will be a combination of the response of these two components:

- **Combination of Noise Generator and Attenuator**:

  The *Noise Generator* (*NG*, Fig.4.13, left image) is a device capable of producing a certain level of signal (measured in units of absolute power, dBm) for each specific frequency in a range for which the device is calibrated. The actual set of data corresponding to the calibration at a given frequency, which can be found in its commercial datasheet, is the so called *ENR*, or *Excess Noise Ratio*, described by the following relation [36]:

  $$ENR = 10 \log_{10} \left(\frac{T_H}{T_0} - 1 \right) \ , \tag{4.3}$$

  where T_0 is the literature reference room temperature of $290\ K$. The ENR is, formally, a measurement of the excess of power (so in dB units) that a Noise Generator emits w.r.t.

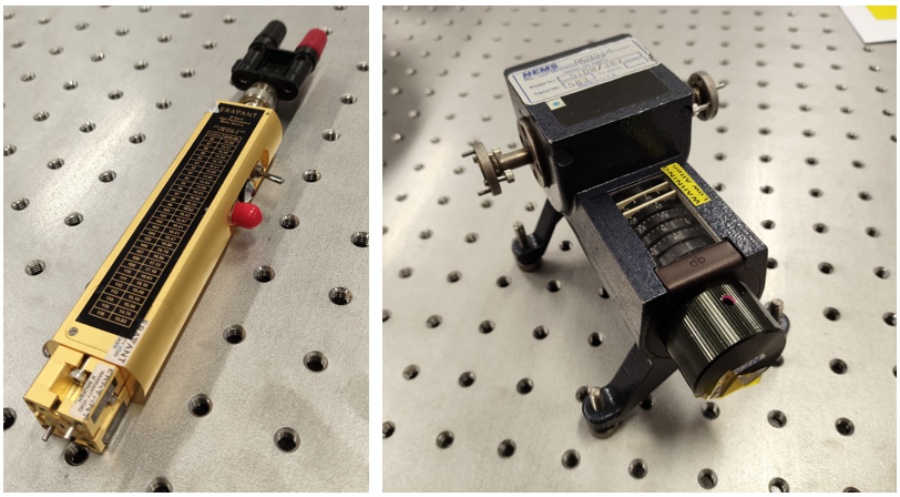

Figure 4.13: The W-Band Noise Generator (left) and the Attenuator (right) employed in the EBB2 Receiver tests. **Left**: Eravant, Serial Number 28797-01; **Right**: Attenuator, Part Number 510W 387, Serial Number 583

the power produced by a source at room temperature. In other words, the ENR is that exponential factor which allows to derive the temperature T_H of a source which emits with an excess of a given amount of decibels w.r.t. the dB-power emitted at T_0, following that same Eq. 4.3, but solved for the T_H instead:

$$T_H = \left(1 + 10^{\frac{ENR}{10}}\right) \cdot 290 \tag{4.4}$$

Thus, once T_H is known, the relative emitted absolute power (dBm units) can be obtained by employing the Johnson-Nyquist Law. To proceed with, as opposite to the second method enlisted in this paragraph, this case-study of NG + Attenuator has not been directly applied to this work, but an extended description of this process is provided anyway for completeness. To begin with, the way in which a Noise Generator can be employed to simulate different *Black Body emissions* of sources at different temperatures is by plugging it directly to the Attenuator itself: in this way, since the output radiation of the NG is modified (attenuated) by the latter, the signal flowing into the RF Chain will correspond to a number of different sources equal to the number of different attenuation levels chosen. The formula describing the process of attenuation of a signal is the following [36]:

$$P_{out} = \alpha \cdot P_{in} + (1 - \alpha) \cdot T_{phys}, \tag{4.5}$$

where P_{out} is the attenuated output power, T_{phys} is the physical temperature of the system (in this work, set always to Room Temperature) and α is the linear attenuation coefficient, $\alpha = 10^{dB/10}$, where dB is the negative attenuation dB-level.
As already introduced in Sec.3.3.4, in order to build a consistent Y-Factor to reproduce the RF Chain Linearity, it is thus necessary to provide a set of powers emitted by a range of sources whose Temperatures are distributed as homogeneously as possible between a maximum one of 10 000 K (corresponding to the NG output without the Attenuator) and the physical temperature of the chain itself, $296K$ (RT). The former case is obtained by applying a null attenuation of $0dB$, so that in Eq.4.5, $\alpha = 10^0 = 1$ and so the term $(1 - \alpha) \cdot T_{phys} = 0$, leaving just $P_{out} = 1 \cdot P_{in} = 10000K$; the latter is instead produced by setting the maximum level of attenuation possible: if Eq.4.5 is considered once again, by applying the just mentioned conditions, the linear attenuation coefficient goes to zero,

since its power is a very high negative number, resulting in $P_{out} = (1-0) \cdot T_{phys} \simeq 300K$. Displayed in Tab.4.2, the set of power values and their converted temperatures selected for those purposes. As already forewarned, this method can be applied to check both the

Attenuation $[dB]$	**Temperature** $[K]$
0	10000
-1	8000
-2	6400
-3	5150
-6	2700
-10	1300
-15	605
-20	307
MAX	300

Table 4.2: Power values and converted temperatures from the Johnoson-Nyquist formula to compute the Linearity of the RF Chain (Configuration A).

linearity of the configuration including the LNA-only, and on the one ending with the diode itself.

In the former case, a Power Meter is employed to acquire the powers outflowing from the last waveguide of the configuration, WG2630. To analyze the entire chain, instead, the tool directly cabled to the Diode which is responsible for the signal acquisition is a digital multimeter, a device which reads the power not in dBm units but in voltages. Here, the application of the concept of ENR is quite fundamental, since it is necessary to compute the real input power entering the Diode in order to verify that it lies in its linear working regime indicated in its datasheet, i.e. $[-25, -60]\, dBm$. The block diagram of this configuration is the one indicated in Fig. 4.14 and it can help to visualize how the different stages of power showed in that same figure, *step A* and *B*, lead to the derivation of the approximated dBm-value order of magnitude at the entrance of the Diode in both NG on and NG off cases. To begin with the former one, the $-51\, dBm$ absolute power

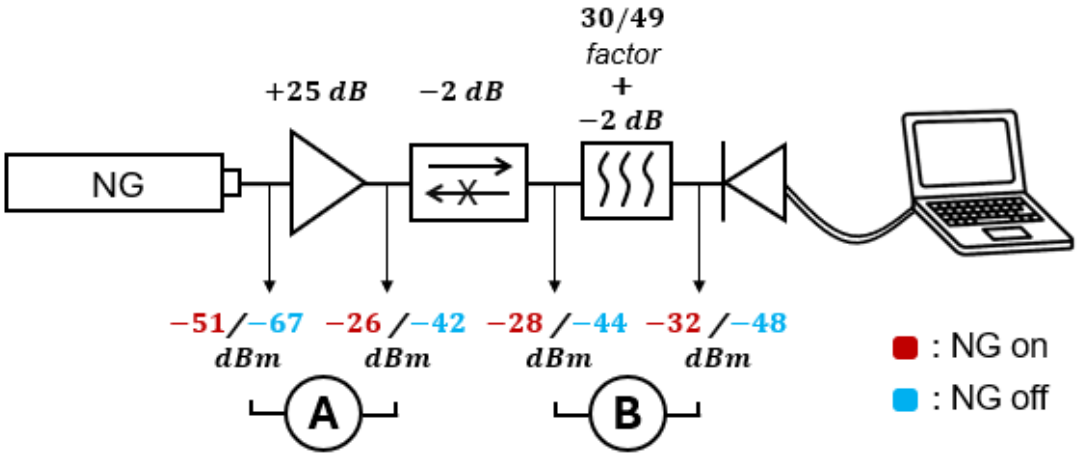

Figure 4.14: Sketch of the Configuration with NG in the lead and the Detector Diode, cabled to a digital multimeter, on the end of the RF Chain. Step A and Step B are necessary to simulate the power entering the Detector Diode, thus checking wether the signal (in both cases NG on, NG off) belongs to its linear regime, $[-25, -60]\, dBm$, or not.

outflowing from the NG (beginning of step A) is computed with the already mentioned Eq. 4.3 by adopting a value of frequency corresponding to the maximum response of the RF Chain's filter at 91 GHz, which refers to the NG's ENR calibrated value of 15.61 dB; thus, the emission temperature derived through the second form of the ENR relation, Eq. 4.4, results to be

$$T_H = \left(1 + 10^{15.16/10}\right) \cdot 290 = 9804.76\ K\ .$$

By now plugging this temperature value in the Johnson-Nyquist Law, assuming the NG working bandwidth of $\Delta\nu = 49\ GHz$ $(67 - 116\ GHz)$, then, the temperature just found correspond to an equivalent emission power of

$$P = k_B T \Delta\nu = 6.76 \cdot 10^{-6}\ mW\ ,$$

which, following the definition of dBm, corresponds to an absolute logarithmic power of

$$P_{dBm} = 10 \log_{10}\left(\frac{P\ [mW]}{1\ [mW]}\right) \simeq -51\ dBm\ . \tag{4.6}$$

This amount of power, passing through the LNA, gest amplified by 25 dB, resulting to a total value at the end of *step A* of $-26\ dBm$. The passage of the signal through the Isolator causes an additional loss equal to its Gain, so of $\sim 2\ dB$, resulting in a $-28\ dBm$ signal entering the BPF. Here, the filtration process of the signal corresponds to a lossy stage too since, by lowering the number of input frequencies, the filter is removing part of the signal itself. In order to parametrize this *step B*, one has to convert the dBm power value back to the mW one by reverting Eq. 4.6 and, then, by multiplying it by a factor which testifies the change of bandwidth from $\Delta\nu = 49$ to $\Delta\nu_{filt} = 30$:

$$P_{mW,filt} = 10^{-28/10} \cdot \frac{30}{49} = 9.7 \cdot 10^{-4}\ mW \Rightarrow P_{dBm,filt} \simeq -30\ dBm\ . \tag{4.7}$$

Finally, to this last value is necessary to add the Gain provided by the physical device itself[2], resulting in a final power of $\sim -32\ dBm$. To conclude with, this same procedure can be applied to the case in which the NG is turned off (room temperature source case) and, as testified from the final values of Step B showed in Fig.4.14, the simulated input powers to the Diode belong to its above-mentioned linear working regime in both the considered cases. The presence of the waveguide WG2630 has been neglected in this computation due to its very small negative Gain ($-0.138\ dB$, value from Power Budget), resulting thus irrelevant in both this rough estimations of orders of magnitudes.

- **Combination of VNA and Attenuator**: it is the process actually employed to obtain a confirmation of the EBB2 Receiver's Linearity. If this condition was previously provided by the computation of a Y-Factor which would have testified a linear working regime by the manifestation of its constant value, the method which is about to be examined follows a different path: this time, the Linearity of the RF Chain has been checked by a combination of only the VNA, which emits a constant input signal and does not provide an absolute output power value (as opposed to, for example, a Power Meter), and the Attenuator, which will cover the same role as different sources simulator, by continuously varying the VNA power emission. The RF Chain Configuration showed in Fig. 4.15 is, thus, considered as the DUT of this case study. It is important to keep in mind the VNA fucntionality which allows to modulate the intensity of the Ports' output power:

[2]Taken directly from the Power Budget

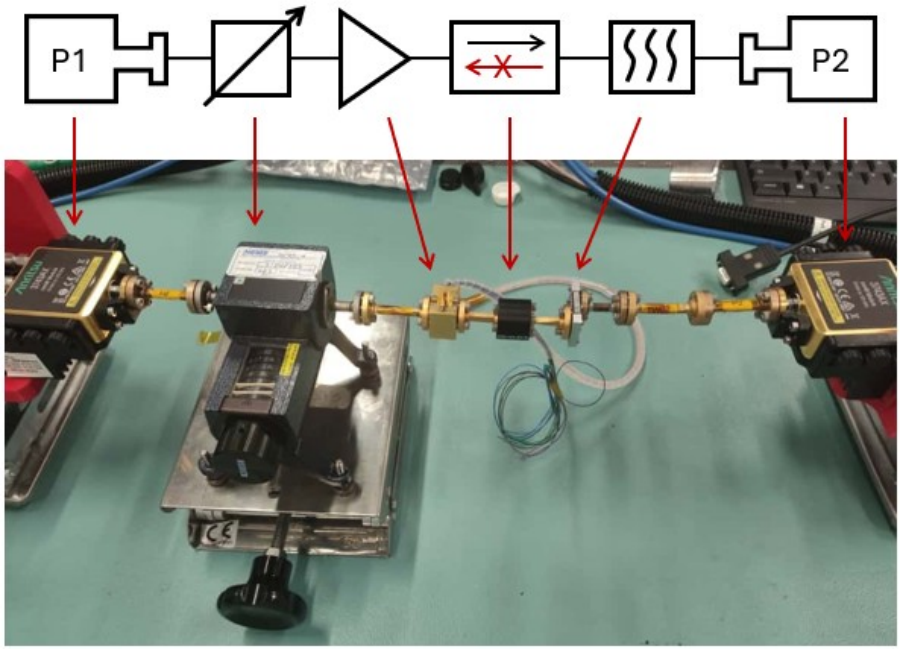

Figure 4.15: Top: block diagram of the configuration characterized by the combination of VNA and attenuator. Between Port1 and Port2, the DUT composed of attenuator plugged to the RF Chain LNA, Isolator, BPF and WG2630; Bottom: actual picture taken during the laboratory Linearity test of the just mentioned configuration.

it is of utmost importance to always check the amount of power flowing into the chain's LNA, so to avoid to cross the breaking point of this device, provided in its datasheet ($-10dBm$ maximum for the one employed in the EBB2 Receiver) and, for this reason, the ports' power level has been set to a safe value of $-30dBm$. Following this premise, the first step to achieve the Linearity verification is to *simulate* the power level which has to be collected by the Diode since, as mentioned above, the Linear regime in cases like this one refers to the region in which both the LNA and the Diode itself behave linearly. However, in this configuration, both ends of the DUT are connected to ports 1 and 2, thus excluding, since it can be only cabled, the presence on the VNA of the Detector Diode. That said, as already anticipated, the Linear region of the latter can be obtained with incoming signals ranging from -25 to $-60dBm$ and, thus, it is necessary to sample an homogeneous distribution of powers in the aforementioned interval. Therefore, the computation to keep in mind is the following: starting from the first power which would arrive to the Diode of $-25dBm$, considering a port power of $\sim -30dBm$ and, at first, a LNA amplification of $+30dB$, the attenuation, not taking into account the remaining RF Components of the chain, has to be set to $-25dBm$, since VNA ports and LNA almost cancel out each other. It is possible to look at this reasoning from an other point of view: if a power of $-25dBm$ is necessary at the Diode entrance and an amplification of $+30dB$ is added to the chain, then, theoretically, an absolute power of $-55dBm$ is needed as total input in the chain. Since the VNA is providing at minimum $-30dBm$ through its ports, to reach that mentioned total value, the attenuator has to cover the remaining $-25dBm$. This exact logic is then applied to all the other powers belonging to the set pointed out earlier, enlisted in Tab.4.3. The last two power levels in Tab.4.3 have not been tested since the relative level of attenuation (third column) fall beyond the limit of the employed instrument's dynamical range. Furthermore, it is possible to observe a higher *crowding* of power values in the first half of the chosen set (first column): this solution has been

Diode Linear range of absolute powers $[dBm]$	**Total input power needed** $(+30dB$ **LNA amplification)** $[dBm]$	**Attenuation levels** $(-30dBm$ **ports power)** $[dB]$
-25	-55	-25
-27	-57	-27
-30	-60	-30
-33	-63	-33
-35	-65	-35
-37	-67	-37
-40	-70	-40
-45	-75	-45
-50	-80	-50 (MAX)
-55	-85	/
-60	-90	/

Table 4.3: First column: set of powers belonging to the linear range in the diode's datasheet; Second column: total input power needed, considering an amplification of $+30dB$ (LNA); Third column: amplification level, added to the ports' $-30dB$, to reach the corresponding value in the second column.

adopted to simultaneously have both a higher statistics and a far more detailed analysis of the initial part of the curve, where the Linearity begins to stabilize. The measured S-parameters curves for attenuation levels displayed in Tab.4.3 are reported in the figures in appendix, second section.

The next step to the Linearity verification achievement, once the levels of attenuation have been selected, is now to understand how the linear regime can be tested without a set of output absolute powers and their Y-Factors, provided by different devices combinations (previous method). The answer to that question lies in the concept of response of the RF Chain when it undergoes different values of attenuation: in principle, if one conducts two measurement on a VNA with two different attenuation levels, when a system (DUT) is perfectly linear, *the difference within the two dB output powers must be equal to the difference within the two dB attenuations*, namely

$$\Delta P = \Delta A \,. \tag{4.8}$$

For example, if a first measurement results in a mean Gain of $-5\,dB$ from a $-15\,dB$ attenuation and a $-10\,dB$ Gain if attenuated by $-20\,dB$ from the second one, then it is clear that to an increase of attenuation of a certain amount, a linear system must respond with that same deviation between the output powers too ($\Delta P = \Delta A = -5\,dB$). As a consequence, the violation of such principle is a symptom of Compression of the Chain response. Having said so, it is now possible to dive into deeper details of the process applied in this case study, through a customized Python script. This code can be subdivided in four main steps:

1. Collection of the VNA output .s2p files, one for each level of attenuation enlisted in Tab 3.3, third column, and extraction of the arrays containing the dB gains for each frequency $(80 - 110\,GHz)$;
2. Generation of an array containing all the possible combinations of pairs of arrays

obtained from point (1) and, thus, production of the set of all the possible ΔP, as well as all the possible associated ΔA;

3. Collection of all the ΔP arrays, ΔP_{tot}, sharing the same value of ΔA (for example, a $\Delta A = 10\,dB$ is shared by the ΔP generated by attenuation pairs of $(-25, -35)\,dB$, $(-35, -45)\,dB$, $(-27, -37)\,dB$ and so on) and, denoting as j the number of ΔA values (ΔA_j) and i the number of ΔP in each single $\Delta P_{tot,j}$ box-array, the derivation of a mean value $\overline{\Delta P}_j$ for each ΔA_j as follows:

$$\overline{\Delta P}_j = \frac{\sum_{i=1}^{N_j} w_{j,i}(\Delta P)_{j,i}}{\sum_{i=1}^{N_j} w_{j,i}} \,, \tag{4.9}$$

This relation describes an average whose weights, a $w_{j,i}$ for each $(\Delta P)_{j,i}$ single value, is based on the vicinity of the distribution of the $(\Delta P)_{j,i}$ points w.r.t. their reference value ΔA_j, so that

$$w_{j,i} = \frac{1}{|(\Delta P)_{j,i} - \Delta A_j|} \,. \tag{4.10}$$

The absolute value on the denominator is fundamental in order to preserve the physical meaning of distance w.r.t. the reference value, since one must consider its module and not the actual position of the point: without this precaution, the distance could be both positive (i.e. the point is above the reference value) or negative (point below reference) and, in the latter case, the thus produced very small (negative) weight could result in a far smaller contribution of a point which could be instead very relevant in the average itself. The uncertainty associated to Eq. 4.9 is provided by the following relation of its standard error $\sigma_{\overline{\Delta P}_j}$:

$$\sigma_{\overline{\Delta P}_j} = \frac{\sigma_{std,j}}{\sqrt{N_{eff,j}}} \,, \tag{4.11}$$

where $N_{eff,j}$ is the effective number of values of each j-th array which actually participate to the relative weighted average, i.e. the points with the higher weights among all the $(\Delta P)_{j,i}$, estimated as

$$N_{eff,j} = \frac{(\sum_{i=1}^{N_j} w_{j,i})^2}{\sum_{i=1}^{N_j} w_{j,i}^2} \,, \tag{4.12}$$

while σ_{std} is instead

$$\sigma_{std,j} = \sqrt{\frac{\sum_{i=1}^{N_j} w_{j,i}((\Delta P)_{j,i} - \overline{\Delta P}_j)^2}{\sum_{i=1}^{N_j} w_{j,i}}} \tag{4.13}$$

and it describes the standard deviation of the j-th array of $(\Delta P)_{j,i}$ values w.r.t. the weighted average of that distribution, $\overline{\Delta P}_j$. The results of this third step are enclosed in Tab 3.4;

4. Derivation of the Best-Fit line through the built-in python function `curve_fit`, which take into account the linear model $y = mx + q$, with x being the ΔA_j values and y the $\overline{\Delta P}_j$ ones, and returns the angular coefficient m and the intercept q of the line, as well as their associated variances contained in the covariance matrix, produced by the python function itself.

ΔA_j $[dBm]$	$\overline{\Delta P}_j$ $[dBm]$
-25	-24.825 ± 0.100
-23	-22.849 ± 0.105
-20	-19.857 ± 0.048
-18	-17.950 ± 0.311
-17	-16.974 ± 0.071
-15	-14.924 ± 0.063
-13	-12.961 ± 0.047
-12	-11.949 ± 0.206
-10	-9.950 ± 0.057
-8	-7.942 ± 0.085
-7	-6.984 ± 0.055
-6	-5.968 ± 0.146
-5	-4.985 ± 0.079
-4	-3.990 ± 0.033
-3	-2.986 ± 0.020
-2	-1.997 ± 0.024

Table 4.4: First column: set of ΔA_j values derived by the difference of each possible combination of pairs taken from the nine attenuation values reported in the first column of Tab 3.3, up to -50 dB; Second column: mean weighted values of all the $(\Delta P)_{i,j}$ merged from all the arrays sharing the same corresponding value of ΔA_j, provided with the associated uncertainties, $\overline{\Delta P}_j \pm \sigma_{\overline{\Delta P}_j}$. As expected from a linear response, the quantities belonging to the $\overline{\Delta P}_j$ column are comparable within the errors with the relative ΔA_j set of data, providing the actual confirmation of Eq. 4.8.

Displayed in Fig. 4.16, the final result proving the Linearity of this configuration: as it was already possible to deduct from the values in Tab. 3.4, the Best-Fit of $\overline{\Delta P}_j$ vs ΔA_j data is coincident within the errors with the bisector of the first quadrant, showing an angular coefficient and an intercept equal to

$$\begin{cases} m = (\ 0.994 \pm 0.002) \\ q = (-0.010 \pm 0.017) \end{cases} \tag{4.14}$$

thus firmly confirming Eq. 4.8: the differences within the dB output powers are indeed comparable to the relative differences within the dB attenuation levels.

4.3.6 Y-Factor and Noise Temperature of the System

Once the Linearity region of the RF Chain has been discovered, it is possible to perform its Y-Factor and, thus, to compute the overall Noise Temperature of the system. To do so, the already treated method involving a combination of Noise Generator and an attenuator has been chosen, since the test has been carried at the University of Milan, where no VNAs were available at the moment. This Configuration can be observed in Fig. 4.17. A digitizer, connected to the Diode, has been able to convert the overall RF Chain output power signal into *Analog Digital Units* (or *ADU*), so to be read by the digital acquisition electronics. As for the Y-Factor, not only at least two output powers are needed, but the ADU value of the offset is necessary too: it represents the reading value of the acquisition electronics when nothing is plugged to

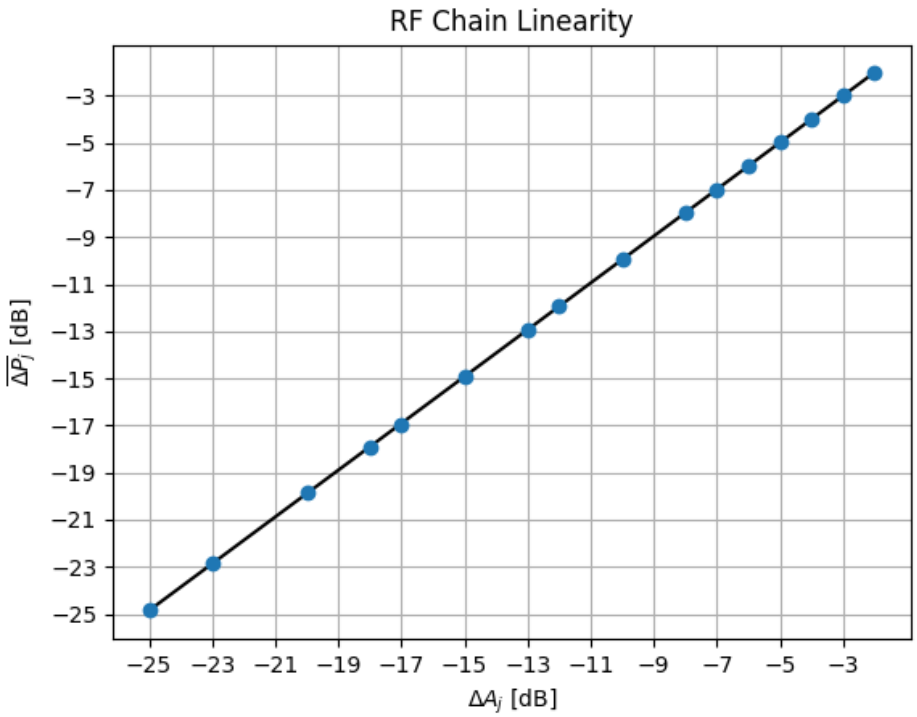

Figure 4.16: The Best-Fit $y = 0.994\,x - 0.010$ obtained through the built-in python function `curve_fit` as the first quadrant bisector, which thus proves the Linearity of the Fig. 4.15 Configuration.

it, therefore an instrumental offset which has to be removed in any case, since it does not correspond to any input physical quantity:

$$Y = \frac{P_H - P_{offset}}{P_C - P_{offset}} = \frac{ADU_H - ADU_{offset}}{ADU_C - ADU_{offset}} \tag{4.15}$$

This different expression of the Y-Factor is derived from the fact that ADU_H and ADU_C, which are the output power values in ADU units of the receiver, so ADU_{out}, are expressed as a modified version of Eq. 3.1b which includes exactly that instrumental offset:

$$ADU_{out} = Gk_B\Delta\nu(T_N + T_A) + ADU_{offset}, \tag{4.16}$$

and so

$$\begin{aligned} ADU_H &= Gk_B\Delta\nu(T_N + T_H) + ADU_{offset} \\ ADU_C &= Gk_B\Delta\nu(T_N + T_C) + ADU_{offset} \end{aligned} \tag{4.17}$$

If those two formulas are plugged in Eq. 4.15, the classical relation for the T_N is reached (Eq. 3.10). As a matter of space occupation, it has been decided to perform the tests with a different and much more compact attenuator (Fig. 4.17, the component connected right after the NG, with the silver control knob on top) with respect to the one employed in Bologna's laboratory, so this new device needed its own characterization and its own attenuation levels chosen to complete the above-mentioned task. For each of these latter ones, the Chain output ADU values of the Configuration have been registered in both the case of the Noise Generator turned on (the T_H, computed with Eq. 4.5) and turned off (T_C, Eq. 4.5). The attenuation values, taken as the control knob notch of the attenuator and their relative actual level of

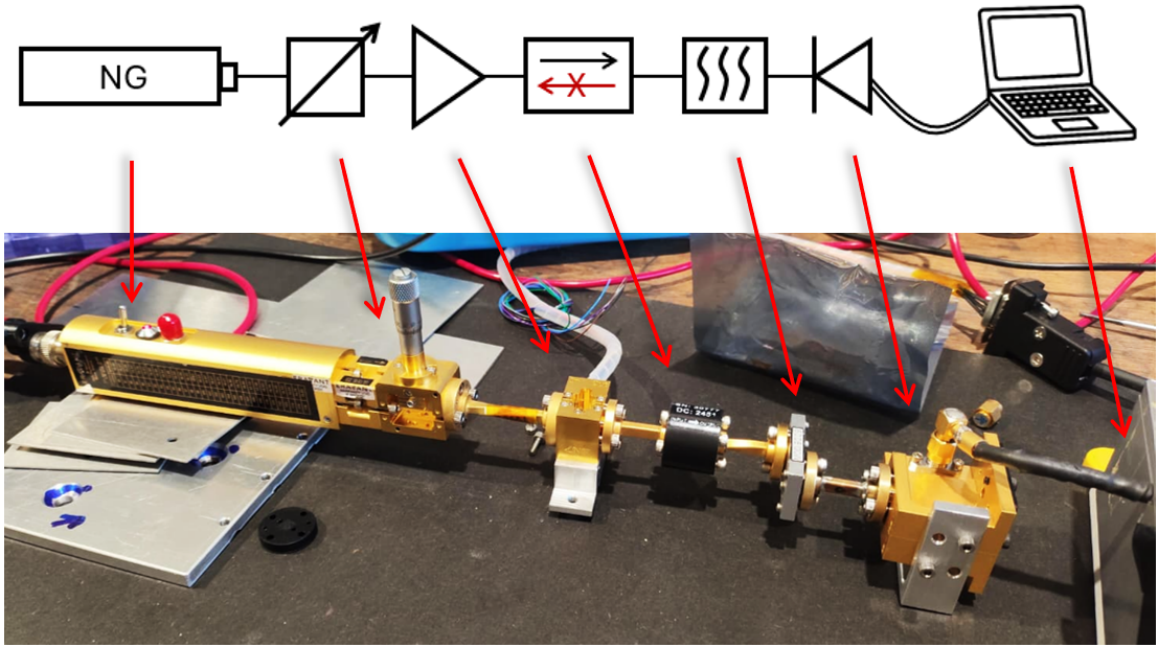

Figure 4.17: Top: Block diagram of the Configuration employed to study the Noise Temperature of the receiver - Noise Generator + attenuator plugged to the RF Chain up to the Detector Diode, cabled to the analog-to-digital acquisition electronics and software. **Bottom**: actual photo of this Configuration. Test carried at the University of Milano.

dB attenuation, as well as the corresponding values in ADU units (NG off and NG on), are contained in Tab. 3.4. Only the ADU values with the NG on are reported, since the NG off case correspond to a costant value of $\sim$ 8000 ADU, no matter the attenuation. The ADU values

Control knob notch	**Attenuation level** $[dB]$	ADU_{on} **value** $[ADU]$
0	-47.65	7987.02
0.5	-21.74	8580.87
0.6	-17.21	9657.54
0.7	-12.76	12475.50
0.8	-8.52	19662.18
0.9	-4.91	34853.50
1.0	-2.18	58401.81
1.1	-0.66	80313.43
1.2	-0.21	88884.31
1.3	-0.17	89611.86

Table 4.5: First column: control knob notch on the attenuator; Second column: actual value of dB attenuation corresponding to the knob levels; Third column: ADU output values of the chain with the NG turned on at certain level of attenuation (previous column).

reported above have been obtained by computing a average between all the ADU values in the 10 seconds bin, each one corresponding to a different level of attenuation in the analog digital electronics output file. Such an attenuation bins' duration has been chosen so to be able to identify them during the file reading.
The process which resulted in the EBB2 receiver's T_N computation has been carried by a *ad hoc* Pyhton code, produced in this work and presented in the next section.

4.3.7 The T_N *ad hoc* Python Code

The complex Python code which allowed the final computation of the sought-after EBB2 receiver T_N is divided in several sections:

a) **The Twist Gain**: The first step of the code concerns the extraction of the mean Gain of particular form of wave guide: a 90° *Twist WR-10 waveguide*, which is visible from Fig. 4.17, connected between the attenuator and the LNA, which has been introduced in the chain just to maintain a preferred spatial rotation of the receiver. It is important to underline that rather than being part of the RF Chain itself, this WG has to be considered as an extension of the attenuator, i.e. its small negative Gain (it is a passive component) has been added to the already negative dB value of attenuation. The obtainment of the Gain values belonging to a given device characterized at the VNA can be achieved in Python through a built-in package called `Scykit-RF`, an Open Source package for RF / Microwave engineering which is able to work with the VNA `.s2p` output files [REF.: https://scikit-rf.readthedocs.io/en/latest/]. Those text files contains numerous key values such as the frequency band chosen during the VNA calibration and, most importantly, the real and imaginary parts of each S-Parameter of the DUT. Clearly, the one of interest is, as usual, the S_{21} Forward Complex Gain. In the first place, the real and imaginary pairs have been filtered in the frequency band of maximum response of the filter introduced in Sec.4.3.4, $88 - 101\,GHz$. Then, it is necessary to compute the *scalar Linear Gain* for each couple of those filtered values

$$G_{Lin} = \sqrt{Re(G_{filt})^2 + Im(G_{filt})^2} \tag{4.18}$$

and, finally, by performing the average of this array of values, the mean linear gain of the twist is achieved, $\overline{G_{Lin}}$. At this point, the application of Eq. 3.15 (in which $|S_{21}|$ in this case is the mean linear gain) is sufficient to compute the the logarithmic mean Gain value in dB units, the one which will be added to the attenuation. The error on this quantity is obtained as follows: **(1)** computation of the standard error on the mean linear gain - $\sigma_{\overline{G_{Lin}}} = \sigma_{G_{Lin}}/\sqrt{N}$, where $\sigma_{G_{Lin}}$ is the standard deviation of the array of linear gains and N is the length of that array (number of linear gains); **(2)** propagation of errors on Eq. 3.15, since it refers to a logarithm of a mean value - $G = 20\log_{10}(\overline{G_{Lin}})$, so the it is necessary to deal with the propagation of a single variable:

$$\sigma_G = \left|\frac{dG}{d\overline{G_{Lin}}}\right| \cdot \sigma_{\overline{G_{Lin}}} \qquad , with \qquad \left|\frac{dG}{d\overline{G_{Lin}}}\right| = \frac{20}{\ln 10} \cdot \frac{1}{\overline{G_{Lin}}}, \tag{4.19}$$

thus reaching the final form of the error associated with the mean gain of the twist through a few simple mathematical passages:

$$\sigma_G = \frac{20}{\ln 10} \cdot \frac{\sigma_{G_{Lin}}}{\sqrt{N}} \cdot \frac{1}{\overline{G_{Lin}}} \tag{4.20}$$

The resulting Gain of the twist with its associated error is

$$G_{TWST} = (-0.1639 \pm 0.0013)\,dB$$

b) **Mean Instrumental Offset**: This second part of the code focuses on the computation of the mean instrumental offset which, as anticipated above, must be removed from the output ADU values of the digital acquisition electronics. This time the data come from the `.txt` file returned from the multimeter itself, which contains the ADUs detected when

all the instrumentation is turned off. An average of those values has been performed, as well as its standard error (standard deviation over the square root of the number of values), resulting in a offset of

$$ADU_{offset} = (2841.75 \pm 14.32)\ ADU$$

c) **Real Output Temperature of the Noise Generator**: The third step consists in computing the actual temperature of the Noise Generator which enters the RF Chain; the 10000 K value used so far was an approximation of the NG equivalent emission relative to the ENR, calibrated for the already introduced EBB2 receiver's mean frequency of 94 GHz (Sec.4.3.4). This portion of the Python script is instead dedicated to the derivation of the mean temperature emitted by the NG corresponding to the set of those produced in the band $[88 - 101]\ GHz$ of maximum response of the BPF. Thus, by applying the concept of Excess Noise Ratio enclosed in both Eq. 4.3 and Eq. 4.4, the above mentioned set of i-temperatures $T_{NG,i}$ has been computed as follows:

$$T_{NG,i} = \left(1 + 10^{\frac{ENR\,i}{10}}\right) \cdot 290\,, \tag{4.21}$$

from which the average NG output temperature $\overline{T_{NG}}$. The associated error of the latter concerns the following errors propagation:

$$\sigma_{\overline{T_{NG}}} = \sqrt{\sum_{i=0}^{N_i} \left(\frac{\delta \overline{T_{NG}}}{\delta T_{NG,i}}\right)^2 \sigma^2_{T_{NG,i}}} = \sqrt{\sum_{i=0}^{N_i} \left(\frac{1}{N_i}\right)^2 \sigma^2_{T_{NG,i}}}\ . \tag{4.22}$$

Since the $T_{NG,i}$ values have been obtained through Eq. 4.21, thus, the error $\sigma_{T_{NG,i}}$ for each $T_{NG,i}$ is

$$\sigma_{T_{NG,i}} = \left|\frac{dT_{NG,i}}{dENR_i}\right| \sigma_{ENR_i} = \left[290\left(10^{\frac{ENR_i}{10}} \cdot \frac{\ln 10}{10}\right)\right] \cdot \sigma_{ENR_i}\ , \tag{4.23}$$

where the $\sigma_{ENR_i} = \pm 2\ dB$ is provided in the Data sheet of the Noise Generator.
The mean NG Temperature resulting from this third step is thus

$$\overline{T_{NG}} = (11551.67 \pm 1388.34)\ K \tag{4.24}$$

d) **Mean ADU Value at each Attenuation Bin and Mean Attenuation Gain Values**: the mean ADU value corresponding at each level of attenuation has been extracted. This process, as well as its results, has already been explained in the previous section, with the support of Tab 3.4. In the same table, the second column contains the actual Gain values of attenuation, computed by employing the same procedure on the VNA `.s2p` files of the Attenuator through Scykit-RF, described in step *a)*.

e) **Equivalent Temperatures to each Attenuation Value**: given the already computed main Gain values of the attenuation levels and of the twist, it is possible to derive the equivalent temperatures corresponding to the hypothetical sources emitting at the always different power values (arising from the several attenuation values applied to the Noise Generator output temperature from point *c)*). These temperatures are fundamental to the T_N inference, since they represent the x-values in the amplification curve, in which the

T_N itself is mathematically derived through the x-axis intercept of the temperatures' best-fit line. The values to be obtained through this process are the results of the attenuation equation described above, Eq. 4.5, in the temperature-related form

$$T = T_{IN} \cdot \alpha + (1 - \alpha) \cdot RT \, , \tag{4.25}$$

where T_{IN} is the temperature entering the attenuator, i.e. the Noise Generator actual temperature obtained through point *c)*, α is the attenuation coefficient and RT the physical temperature of the Attenuator, the Room Temperature. As anticipated in point *a)*, the exponent of the attenuation coefficient $\alpha = 10^{G_{TOT}/10}$, G_{TOT}, must take into account both the attenuation levels in the second column of Tab 3.4, named here G_{ATT}, and the Gain of the Twist, thus resulting as $\alpha = 10^{(G_{ATT}+G_{TWST})/10}$. For what concerns instead the derivation of the errors associated to the array of the temperatures just computed, a multiple-step errors' propagation is necessary: (1) the first source of error is the already discussed attenuation coefficient. Its exponent as the sum of two mean values need an error expansion of a function $f(x, y) = 10^{(x+y)/10}$, with an uncertainty

$$\sigma_\alpha = \sqrt{\left(\frac{\delta f}{\delta x}\right)^2 \sigma_x^2 + \left(\frac{\delta f}{\delta y}\right)^2 \sigma_y^2} \quad , \tag{4.26}$$

where x and y are G_{ATT} and G_{TWST}, namely. Proceeding with the computation, the two partial derivatives under square root result to be

$$\frac{\delta f}{\delta x} = 10^{\frac{x+y}{10}} \cdot \ln 10 \cdot \frac{1}{10} = \frac{\ln 10}{10} \cdot 10^{\frac{x+y}{10}} = \frac{\delta f}{\delta y} \, . \tag{4.27}$$

Given now Eq. 4.27, the relation for the uncertainty associated with the attenuation coefficient, with $x = G_{ATT}$ and $y = G_{TWST}$, can be expressed as follows:

$$\sigma_\alpha = \frac{\ln 10}{10} \cdot 10^{\frac{x+y}{10}} \sqrt{\sigma_{G_{ATT}}^2 + \sigma_{G_{TWST}}^2} \quad , \tag{4.28}$$

where both $\sigma_{G_{ATT}}$ and $\sigma_{G_{TWST}}$ are derived through the same exact procedure conducted in point *a)* and described by Eq. 4.20. To conclude with, the propagation of errors carried by Eq. 4.26 does not include the covariance factor under square root, since $x = G_{ATT}$ and $y = G_{TWST}$ result to be independent quantities.

f) **Uncertainties on the amplification curve y-values**: Speaking of errors, the previous point concerned the derivation of the σ-values associated with the x-points of the amplification curve. The same approach must be adopted in order to provide the full set of errors, y-axis ones included. The points which lie on that axis are the ADU values of the powers detected by the digital acquisition electronics and reported in the third column of Tab. 3.4 (ADU_{on} value $[ADU]$), from which though the ADU_{offset} value still needs to be removed. The function whose errors needs to be propagated is, thus, $f = ADU_{on} - ADU_{offset}$ (point *b)*), a function containing the difference between two mean values. Clearly, such a function presents unitary values of both the partial derivatives and, thus, a $\sigma_{ADU_{on}-ADU_{offset}}$ equal to

$$\sigma_{ADU_{on}-ADU_{offset}} = \sqrt{\sigma_{ADU_{on}}^2 + \sigma_{ADU_{offset}}^2} \quad , \tag{4.29}$$

where both those σ-values are the already obtained standard errors on the means;

g) **The Value of T_N from the ODR Method Best-Fit**: Now that a complete set of uncertainties in both axis has been provided, it is finally time to produce the main result of this python code, the EBB2 receiver's noise temperature, starting from the *Best-Fit line*. Instead of using the standard *OLS*, or *Ordinary Least Squares* method, in which the residuals which arise from the vertical experimental-theoretical deviation (on the y-axis) are minimized, the method chosen to perform this procedure is the so called *ODR Method*, or *Orthogonal Distance Regression*: it takes into account the orthogonal distances on both axis w.r.t. the model curve. When this method is fed with a linear model $y = mx + q$ and with the array of σ_x and σ_y, the values of m and q are returned, as well as the full *covariance matrix*

$$cov = \begin{pmatrix} \sigma_m^2 & cov(m,q) \\ cov(m,q) & \sigma_q^2 \end{pmatrix}, \tag{4.30}$$

where σ_m^2 is the *variance* (i.e. the uncertainty squared) on the linear model slope, σ_q^2 the variance on the intercept and, finally, $cov(m,q)$ the parameter which points out how much the quantities m and q are correlated: in general, if $cov(m,q) > 0$ the two values are correlated, while anti-correlated (typical in linear fits) otherwise. With the elements of the covariance matrix, it is possible to compute the *Correlation Parameter* ρ between m and q:

$$\rho = \frac{cov(m,q)}{\sigma_m \cdot \sigma_q}. \tag{4.31}$$

If $-0.5 > \rho > 0.5$ then there is a strong correlation ($\rho > 0.5$) or anti-correlation ($\rho < -0.5$) within m and q; if $-0.8 > \rho > 0.8$ then one is in front of a very strong correlation/anti-correlation between the two parameter, while, instead, $\rho = \pm 1$ refers to a perfect correlation/anti-correlation. This step of the Python code returned the following results:

$$\begin{cases} m = (7.71 \pm 0.05) \\ q = (2885.56 \pm 21.04) \\ cov(m,q) = -0.80 \end{cases} \tag{4.32}$$

producing, thus, the following linear model and correlation parameter:

$$\begin{cases} y = 7.71\, x + 2885.56 \\ \rho = -0.826 \end{cases} \tag{4.33}$$

In agreement with what just anticipated about the Correlation Parameter, the classic behavior of linear model emerged, with a very strong anti-correlation between its slope and its intercept, meaning that with the increase of one of them, the other necessarily decreases to counterbalance and viceversa. Finally, by recalling the theory included in Sec.3.3.4, for which

(a) the slope of the Best-Fit m provided above is the Gain value (Eq. 3.1b) which allows the astrophysical-instrumental noise decoupling;

(b) the T_N is the intercept of the negative x-axis with the Best-Fit passing through the couples of values (T, ADU_{on});

The receiver T_N can be computed, since the intercept computation is performed through the $y = 0$ condition, thus turning the linear relation into $0 = mx + q \Rightarrow x = -q/m$, where x is exactly the noise temperature. Displayed below in Fig. 4.18, thus, the final result. The Best-Fit obtained through the ODR method has identified an intercept value of

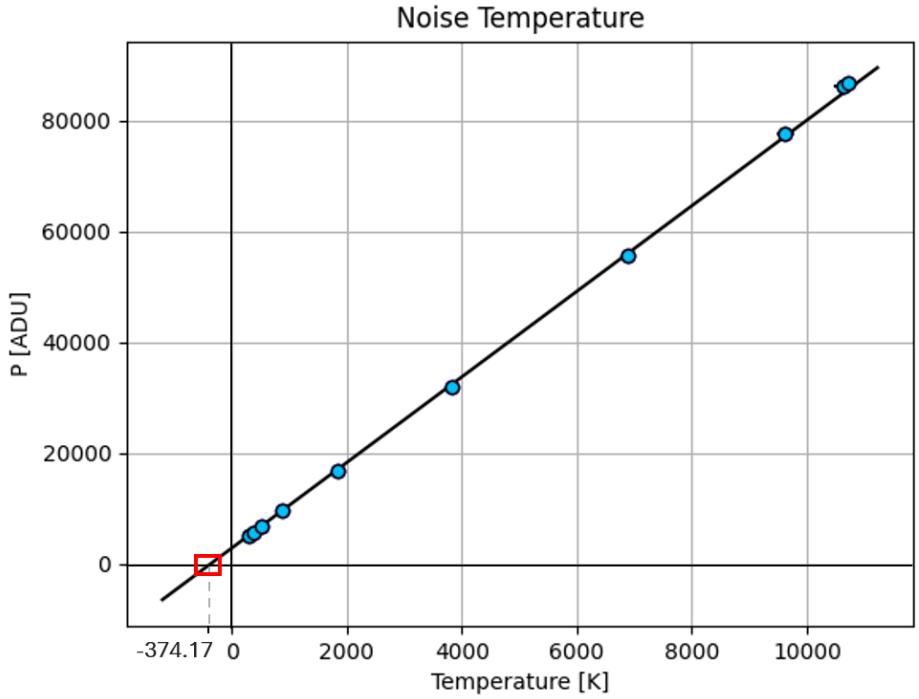

Figure 4.18: The linear Best-Fit $y = 7.71\ x + 2885.56$ obtained through the ODR method and its intercept with the x-axis, corresponding to a total Noise Temperature of the EBB2 Receiver equal to $|T_N| = 374.17\ K$ (errors included, covered by the point markers).

$$T_N = \left| -q/m \right| = (374.17 \pm 4.75)\ K \quad , \tag{4.34}$$

with an uncertainty of $\pm 4.75\ K$ arising from the following propagation of errors:

$$\sigma_{T_N} = \sqrt{\left(\frac{\delta T_N}{\delta m}\right)^2 \sigma_m^2 + \left(\frac{\delta T_N}{\delta q}\right)^2 \sigma_q^2 + 2\left(\frac{\delta T_N}{\delta m}\right)\left(\frac{\delta T_N}{\delta q}\right) cov(m,q)} \quad , \tag{4.35}$$

being m and q dependent variables.
As final observation, the resulting T_N of Eq. 4.34 is very close to the expectation set at the beginning of the EBB2 Receiver dissertation, during the production of the RF Chain preliminary Gain Budget, namely of $382\ K$. This successful comparison not only proves the importance of the above mentioned Budget, but also satisfies the physical requests imposed by the Friis Formula (Eq4.2, Sec4.3.2), confirming the already anticipated dominant effect of the LNA as the T_N results to be almost completely leaded by the NET of the amplifier itself (and by the NETs of Horn and Circular - Rectangular Transition, to a lesser degree), actually not so different from its Noise Temperature reported in the fragment of its datasheet shown below, in Fig. 4.19 .

h) **Second T_N computational method**: The second way in which the Noise Temperature of the system can be derived, considered in this work as more of an instructive exercise, is the one suggested in Sec.3.3.4 and depicted in its Fig.3.6: in principle, instead of the intercept of the overall best-fit of the entire set of data, it would be also possible to plot all the best-fits passing through each single combination of temperatures' pairs belonging to that set. If those data lie in the linear region of the receiver, the average value of T_N resulting from all the intercepts of the whole set of best-fits should still be comparable with the dominant LNA's NET. Fig.4.20 provide the graphic result of this method: it is possible to observe, in particular on the right zoom-in image, a quite wide scatter

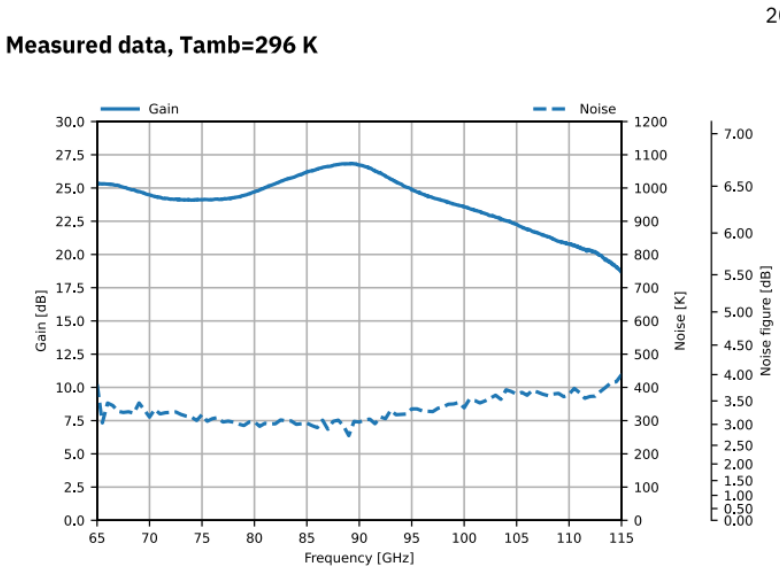

Figure 4.19: A fragment of the LNA 005H datasheet: the Noise Temperature of the amplifier has been chosen of $\sim 340\ K$ as an approximation of the average T_N in the filter maximum response frequency working band of $88 - 101\ GHz$ (dashed cyan lower line).

between all the linear models generated by each pair of temperatures, leading to several different values of T_N located at all the x-axis intercept points. The average of these Noise Temperatures results to be

$$\overline{T_N} = (272.63 \pm 37.25)\ K \ , \tag{4.36}$$

a value which well-represents the juts mentioned scatter effect: this method results to be very sensitive to all the possible experimental fluctuation, since the closer the temperatures in a best-fit pair, the higher the probability of producing a best-fit with an anomalous slope with respect to the reference one of the main ODR linear model produced in the previous code step. Furthermore, this effect gets thus maximized for the pairs of consecutive temperature values, heavily affecting the average T_N by introducing an enormous variance within all the best-fits' intercepts ($\pm 37.25\ K$ versus the previous $\pm 4.75\ K$), and being able in this way to lower the average value by a lot. For the reason just enlisted, even if this method is applied in the linear region of the receiver, its result is not wrong, but neither very comparable w.r.t. the one rigorously derived by applying the ODR method: the average of the pairs' intercepts systematically underestimates the real T_N by introducing a bias over the lower intercepts[3], thus implying a quite large uncertainty.

i) **ODR T_N *vs* ON/OFF T_N**: Unfortunately, further routine tests which have been conducted on the receiver resulted in an irreparable malfunctioning of the LNA 005H, causing the complete loss of control of the Drain Current through the Gate Voltage. For this

[3]The T_N positive values are unphysical results, since the method allows mathematically negative temperatures only as valid (physical) results. Those very high (positive) T_N values are the one which sistematically lower the effect of the negative T_N in the average computation

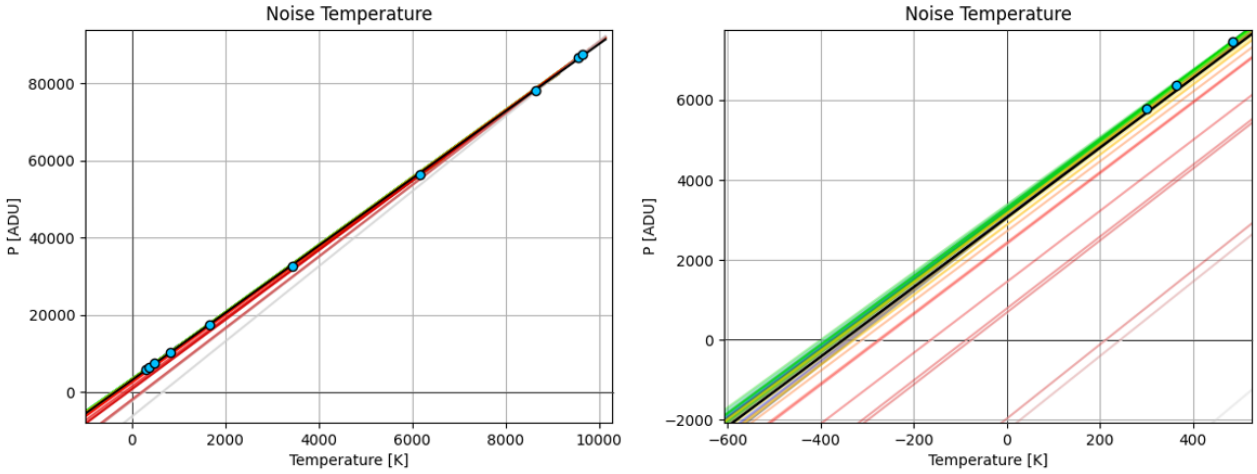

Figure 4.20: The best-fit lines produced by the set of all the possible combination of each temperatures' pair. The wide scatter effect produced by the positive T_N values is quite evident, especially in the zoom of this phenomenon provided by the left plot.

reason, this amplifier has been replaced with the spare LNA $003H$, characterized by a slightly different bias of $V_g = 1.5V$ and $I_d = 35mA$, instead of the nominal $V_g = 1.5V$, $I_d = 25mA$ of the previous $005H$. In order to follow the deadline for the receiver shipping to Antarctica, the same whole set of tests conducted for the former LNA could not be run. However, has it has already been extensively asserted so far, the fastest way to produce a Y-Factor (thus a test on linearity) and a Noise Temperature, is to perform two measurements regarding both a Hot and a Cold Temperature and their relative detected power (still in ADU units), so to be able to employ Eq 4.15 and, thus, Eq. 3.10. Maintaining the Configuration reported in Fig. 4.17, with the exception of the attenuator presence, this can be achieved by simply turning on the noise generator (T_H) and collecting the output power of the receiver and then by repeating the measurement with the NG turned off, in order to detect the power emitted by a source at room temperature (T_C). Thus, a simple but nevertheless effective approach has been adopted: since the LNA $005H$ rigorous result of T_N is available, one could in principle simulate the quick process just described by using the pair of temperatures corresponding exactly to the cases of NG turned on and turned off, computed as reported in Sec.4.3.5 (Eq.4.5) when the attenuator is set to the minimum and maximum attenuation levels namely, and then successively compare this less rigorously-derived Noise Temperature thus obtained, with the one resulting from the ODR method. By doing so, it is possible to check the reliability of the faster T_N estimation and, eventually, to be aware of the possible deviation between the two to be applied to the ON/OFF cases conducted on the LNA $003H$. In order to compute the uncertainty of this new value of Noise Temperature for the LNA $005H$, a two steps computation has been performed: (1) derivation of the Y-Factor error, σ_Y, through the errors propagation formula, regarding the three ADU measurements (NG On, NG Off and instrumental Offset)

$$\sigma_Y^2 = \left(\frac{\delta Y}{\delta ADU_{on}}\right)^2 \sigma_{ADU_{on}}^2 + \left(\frac{\delta Y}{\delta ADU_{off}}\right)^2 \sigma_{ADU_{off}}^2 + \left(\frac{\delta Y}{\delta ADU_{offset}}\right)^2 \sigma_{ADU_{offset}}^2 \quad (4.37)$$

with such partial derivatives:

$$\begin{cases} \dfrac{\delta Y}{\delta ADU_{on}} = \dfrac{1}{ADU_{off} - ADU_{offset}} \\ \dfrac{\delta Y}{\delta ADU_{off}} = -\dfrac{Y}{ADU_{off} - ADU_{offset}} \\ \dfrac{\delta Y}{\delta ADU_{offset}} = \dfrac{Y-1}{ADU_{off} - ADU_{offset}} \end{cases}$$

(2) final computation of the T_N error, σ_{T_N}, based on σ_Y:

$$\sigma_{T_N}^2 = \left(\frac{\delta T_N}{\delta Y}\right)^2 \sigma_Y^2 + \left(\frac{\delta T_N}{\delta T_H}\right)^2 \sigma_{T_H}^2 + \left(\frac{\delta T_N}{\delta T_C}\right)^2 \sigma_{T_C}^2 \tag{4.38}$$

with such partial derivatives:

$$\begin{cases} \dfrac{\delta T_N}{\delta Y} = \dfrac{T_C - T_H}{(Y-1)^2} \\ \dfrac{\delta T_N}{\delta T_H} = \dfrac{1}{Y-1} \\ \dfrac{\delta T_N}{\delta T_C} = -\dfrac{Y}{Y-1} \end{cases}$$

Before showing the resulting quantities, it is necessary to point out that, differently from the complications described in the point *h)* method, the Pair of temperatures corresponding to the ON/OFF cases of the Noise Generator is the one which gets less affected by the above-mentioned bias, since those temperatures are the two extremes of the set, thus located at the maximum distances w.r.t. each other. For this reason, this pair is the one which best singularly approximates the slope of the ODR method linear model among all the other best fits. This last statement is strongly proved by the comparison between the ODR-derived T_N and the one resulting from this last method of a single temperatures' pair emerging from the ON/OFF state of the Noise Generator:

$$\begin{aligned} T_{noise,ODR} &= (374.17 \pm 4.75)\ K \\ T_{noise,ON/OFF} &= (363.31 \pm 10.86)\ K \end{aligned} \tag{4.39}$$

These values show a perfect comparability within the uncertainties provided, thus guaranteeing full reliability in performing the Noise Temperature of the new LNA $003H$ with just two measurements of output power taken with the Noise Generator turned on ($\sim 10000 - 11000\ K$) and then turned off ($\sim 290\ K$), based upon a preliminary check of the linearity with a new Y-Factor which must remain near the one related to the linear regime of the Receiver.

Reported in Tab. 4.6, all the collected data belonging to the Configuration in Fig. 4.17 with the LNA$005H$ replaced by the LNA$003H$, set to three different Bias values:

- **BIAS 35**: $V_d = 1.5\ V$, $I_d = 35\ mA$;
- **BIAS 30**: $V_d = 1.5\ V$, $I_d = 30\ mA$;
- **BIAS 25**: $V_d = 1.5\ V$, $I_d = 25\ mA$.

BIAS 35	
ADU_{off} $[ADU]$	17700
ADU_{on} $[ADU]$	260800
T_C $[K]$	294.15
T_H $[K]$	11551.67
Y-Factor	17.36
T_N $[K]$	393.91

BIAS 30	
ADU_{off} $[ADU]$	14250
ADU_{on} $[ADU]$	196950
T_C $[K]$	294.15
T_H $[K]$	11551.67
Y-Factor	17.02
T_N $[K]$	408.80

BIAS 25	
ADU_{off} $[ADU]$	9470
ADU_{on} $[ADU]$	116800
T_C $[K]$	294.15
T_H $[K]$	11551.67
Y-Factor	17.19
T_N $[K]$	401.07

Table 4.6: Main values related to the three BIAS settings of the LNA 003H mounted on the EBB2 receiver during Milano test obervations, October 2025.

Chapter 5

Optical Models of Solaris telescopes

In this chapter, the electromagnetic (EM) models of the 1.5 m Milano test telescope and the 2.6 m ROSA telescope are presented, with the goal of calculating the beam patterns for the current configurations with the EBB2 installed. After a brief introduction of the software used and general concepts of the study, the EM models are described and the results reported. Finally, the convolutions of the two telescopes power patterns with different Sun models are provided, so to simulate an observation with ROSA, while for Milano to compare them with the real solar observation acquired.

5.1 Introduction to the GRASP Software

GRASP (General Reflector Antenna Software Program), a state-of-the-art widely recognized commercial software part of the TICRA Tools suite [44] , is a software dedicated to the design of single- and dual-reflector antennas systems. It permits an extremely accurate simulations of the radiated (or received) electromagnetic fields of reflector antenna systems, using advanced computational electromagnetic methods, such as Physical Optics (PO) and Geometrical Theory of Diffraction (GTD).

In this thesis' work, the GRASP software has been employed not only to simulated as precisely as possible the response of the two Solaris telescopes (i.e. the Milano Test and Antarctica Concordia ROSA optics), but also to study further optimization of the optical coupling between the telescopes and the receivers, in order to find the best configurations in terms of main angular resolution, the so called Full Width Half Maximum (FWHM), and sidelobes levels. The setup of each telescope EM model can be divided in the following steps [45]:

1. the implementation of the telescope geometry, i.e. relevant coordinates systems, mirrors' shape and locations;

2. the electromagnetic definition of the feed horn located at the telescope focus. In GRASP this is the origin of the electromagnetic waves that scatter through the reflectors to the sky (far-field);

3. definition of the calculations methods, such as Physical Optics (PO) and Physical Theory of Diffraction (PTD)

4. setting of the calculation commands' sequence to compute the final beam patterns for the configurations studied

In the following paragraph, those steps are described in detail, as applied to the two optical configurations studied for Solaris Project.

Figure 5.1: The ROSA Antenna in Concordia Station, Antarctica (Left) and the Milano Test Antenna (Right): the two Cassegrain configurations and their metallic support struts supporting the subreflector.

.

5.1.1 Telescopes' Models

The first step, which has to be dealt with during the design of this work's complex antenna configurations, is the *reflectors geometry*. Both optical systems are on-axis Cassegrain configurations, i.e. optical systems that mount a parabolic primary mirror and a hyperbolic secondary mirror. For these simulations we used mathematical ideal surfaces composed of perfect conductors (i.e. infinite conductivity). Tab.5.1 reports the geometric parameters of the two telescopes.

Milano Test Antenna			
Primary Mirror		Secondary Mirror	
Shape	Paraboloid	Shape	Hyperboloid
$D[mm]$	1500.0	$D[mm]$	296.0
$R_{hole}[mm]$	150.0	$2a[mm]$	293.3
$f[mm]$	1500.0	$2c[mm]$	880.0
-	-	e	3

Concordia ROSA Antenna			
Primary Mirror		Secondary Mirror	
Shape	Paraboloid	Shape	Hyperboloid
$D[mm]$	2600.0	$D[mm]$	294.0
$R_{hole}[mm]$	125.0	$2a[mm]$	424.0
$f[mm]$	1300.0	$2c[mm]$	700.0
-	-	e	1.65

Table 5.1: The optical parameters of Solaris' Milano Test Antenna and Concordia ROSA Antenna configurations required to their construction on GRASP. Primary mirror: shape, reflector diameter, central hole radius and focal length; Secondary mirror: shape, reflector diameter, vertex distance ($2a$), foci distance ($2c$) and eccentricity e.

For each telescope, two different configurations have been implemented in GRASP. The first one, as shown in Fig.5.2, is composed by the primary mirror, the secondary mirror and the Feed Horn placed in the respective Cassegrain focal point (Tabulated horn and then in Hybrid mode Conical horn). The second configuration, a more realistic one, included the presence of the *subreflector support struts* which sustain the secondary mirror in front of the primary one, as shown in Fig.5.3 (GRASP model) and in Fig.5.1 (Photos of the two antennas). The two configurations lead to different beam pattern calculation procedures, as will be explained in Sec.5.1.4.

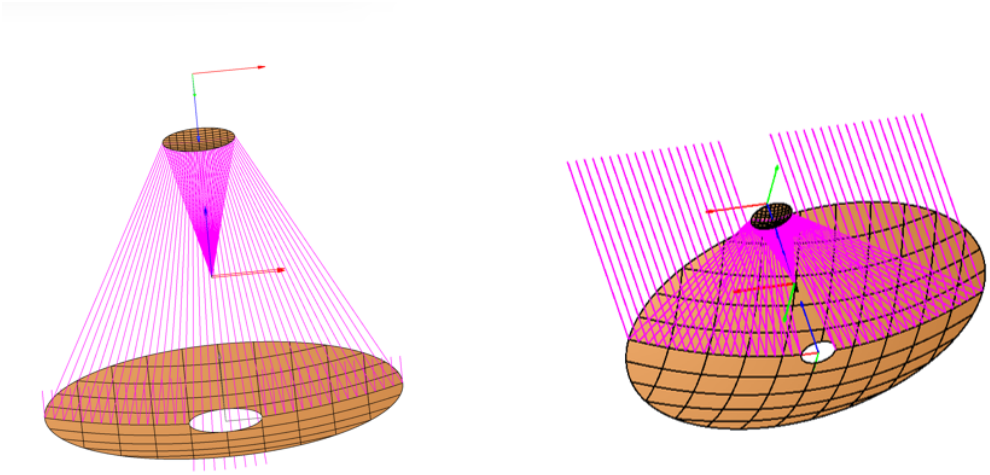

Figure 5.2: Struts-less optical configurations of Milano Test Antenna (Left) and Concordia ROSA Antenna (Right).

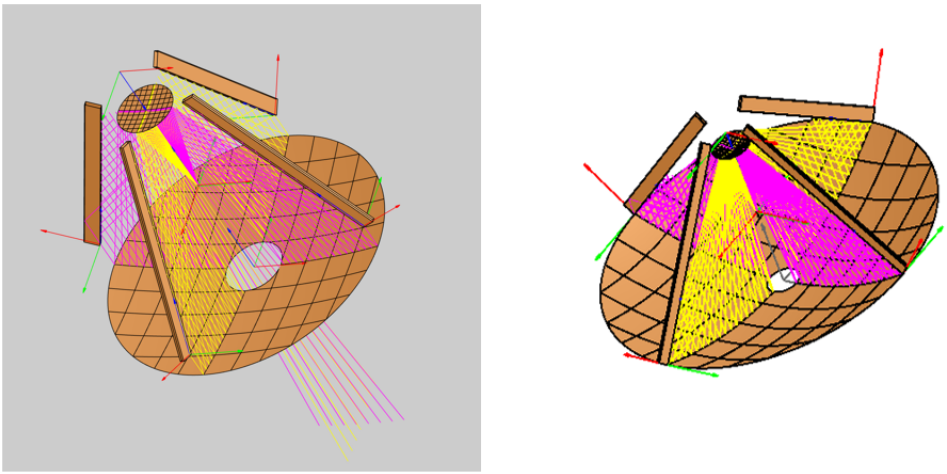

Figure 5.3: Optical configurations of Milano Test Antenna (Left) and Concordia ROSA Antenna (Right) with their relative struts support systems.

Hybrid mode Horn		
$ET\ [dB]$	$R_a\ [mm]$	$L\ [mm]$
-10	7.39	51.93
-11	7.82	54.97
-12	8.25	57.96
-13	8.67	60.91
-14	9.09	63.83
-15	9.50	66.75
-16	9.91	69.65
-17	10.33	72.55
-18	10.74	75.45
-19	11.15	78.37
-20	11.57	81.31

Table 5.2: Geometrical parameter ([46]) relative to each given ET value in the $ET = [-20, -10]\ dB$, i.e. horn aperture radius, R_a and horn length, L. Horns' constant aperture angle and taper angle fixed at 8.1° and 13.996°, namely.

5.1.2 Feed Horns Models and Edge Taper

For what concerns the feed (in emission) illuminating the reflectors, in both case studies of Milano and ROSA two different kinds of feed horn have been tested:

- **Hybrid mode Conical Horn**: this *electrical object*, in GRASP terms, is able to simulate the output of a horn given its aperture and its length, as well as its so called *semi-flared* angle, which represents the angle subtended to the aperture itself starting from the central axis of the horn. More importantly, this model could represent a corrugated conical horn very well under balanced hybrid conditions [7]. It should be noted that it is possible to set different values of *Edge Tapers* (see below for the definition of this important parameter) by varying the aperture diameter and the length of the horn model. Reported in Tab.5.2, such geometrical features of the horn models for each value of ET, computed by following Section 3.2 of [46]. These values have been derived by assuming the horns as cones with a constant aperture angle of 8.1° (following the Alma Band-2/3 corrugated circular horn model in [29]), and with a taper angle value of $\theta_{ET} = 13.996°$ (related to the telescopes' secondary mirror, Fig.5.5)

- **Tabulated Horn**: this specific kind of horn provides a far more realistic model,since it takes in input a data file of its realistic radiation pattern derived form measurements or real horn geometry simulations as in the case of the horn used in Solaris.

The comparison among these different feeds can be appreciated in Fig.5.4: while the beam patterns of the set of horn models at different edge taper values show the typical behavior of a linear conical corrugated horn under the perfect hybrid-mode condition, the beam pattern of the tabulated horn derive from a specific electromagnetic design optimized for a different optics (ALMA band 2, [52]). An important quantity that describes the electromagnetic coupling between the horn and the reflector is the so-called *Edge Taper* (ET). By definition, it is the power value of the pattern illuminating the rim of the reflector, normalized to the pattern at the center of the reflector. In this case of the on-axis Cassegrain optics, the ET can be represented by the level of the feed horn normalized beam pattern at the angle subtended by the secondary reflector. This angle is usually called *Taper Angle*, as shown in Fig.5.5, and the ET is expressed in dB units.

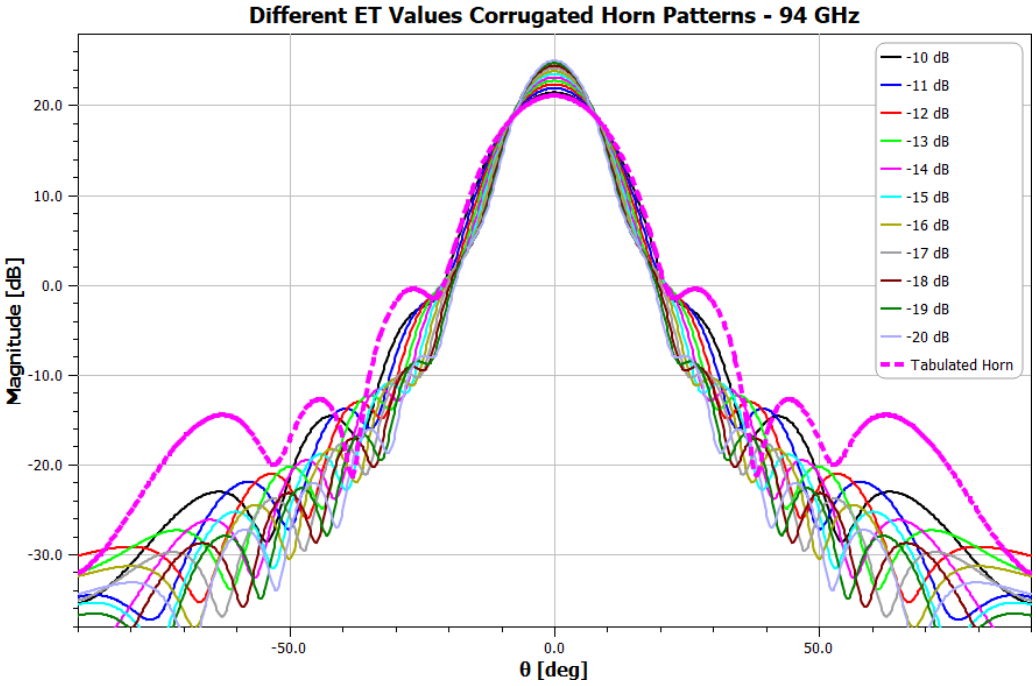

Figure 5.4: Comparison among the different Mixed mode conical feed horns radiation outputs at different ET values. The purple dashed lines represents instead the Tabulated Horn one, whose higher sidelobes arise from its more realistic response.

In case the radiation pattern of the horn can be approximated by a Gaussian shape, the ET fully defines the Gaussian profile [12]. In the case of a horn antenna, such as corrugated horns, the ET can be set by an appropriate diameter of the horn.

The ET is one of the main parameters of reflector antenna design and optimization process, since it impacts the angular resolution and the sidelobe levels [41].

5.1.3 Choice of Frequencies for the Simulations

The choice of the simulation's frequencies is fundamental since it depends on the receiver sensitivity as reported in Sec4.3.4. Two cases have been investigated. The first one concerned a frequency of 94 GHz, as the ν characterized by the higher dB response in the EBB2 receiver's Response Curve (Sec4.3.4) and, thus, considered as the mean frequency of the EBB2's BPF. This case of a single frequency is used to simulate the effects of the supporting struts because of the time consuming calculations. The second case is a range of frequency between 88 and 101 GHz, as the one of maximum response of the above mentioned receiver's BPF (Sec4.3.4) and here used to simulate the optics responses at various edge taper.

5.1.4 Beam Pattern Calculations

As already anticipated, the beam patterns of the two configurations, with and without struts, have been simulated in GRASP in different ways for both Milano and ROSA telescopes. A list of the commands used in the software [45] is hereafter reported and briefly discussed with the corresponding source (input) and target (output) of each one of them:

- **Struts-less Antennas configurations**: this is the most simple layout. The calculation procedure foreseen the simulation of the currents induced on the secondary mirror by the feed horn-emitted field and, consequently, the calculation of the currents induced by the

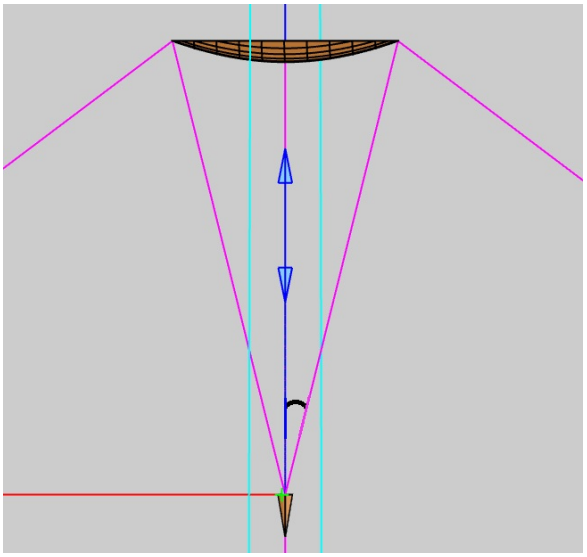

Figure 5.5: Taper angle: angle in black between half the reflector and its edge.

feed horn + secondary mirror on the primary one, before projecting the field into the sky. To do so, the Physical Optics (PO) method is used: it approximates the reflectors, under the Huygens Theorem, as the sum of n-elements each acting locally as infinite plane reflector illuminated by a plane wave. In order to include also the points at the edges of the reflector in analysis, the Physical Theory of Diffraction (PTD) is applied too. By first assuming the case of a Mixed mode conical Horn in a Cassegrain configuration, a cascade of commands is generated to provide the full implementation of the overall Power Pattern's simulation:

- ☐ `Get Currents`, **source**: beam of the feed at given Taper value, aperture width and semi-flared angle,**target**: secondary mirror, turned into an electrical object by the PO analysis;
- ☐ second `Get Currents`, **source**: electrical secondary mirror (the induced currents computed in the first Get Currents), **target**:primary mirror, turned into an electrical object by the PO analysis;
- ☐ `Get Field`, **source**: electrical primary mirror (the induced currents computed in the second Get Currents), **target**: spherical cut in the sky under the same theoretical treatment discussed in Sec.5.1.2;
- ☐ `Add Field`, **source**: electrical secondary mirror + feed gaussian beam pattern (the induced currents computed in the second Get Currents), **target**: the spherical cut mentioned in the previous point; this is an important correction to be applied in order to have as the final output the overall total field described by

$$E_{tot} = E_{scatt} + E_{inc} \,, \tag{5.1}$$

where E_{inc} is the field produced by the system secondary mirror + feed, incident on the primary one. Without this command, the software would simulate as the field projected into the sky and visualized through the spherical cut the one scattered by the primary mirror only, so E_{scatt}. However, thanks to this correction, the incident field E_{inc} is added to the latter, in order to obtain as final field output in the spherical cut the total one, E_{tot}, thus following Eq.5.1 [45].

- **Configurations with struts**: GRASP is actually able to perform a computation of the currents induced on those metal structures too and, for this reason, their thus produced field must be added on the total field storage method in the sky, either spherical cuts or grids. In order to do so, to the group of cascaded commands enlisted in the struts-less case, a smaller subgroup of commands has to be integrated:

  - ☐ `Get Plane Wave Expansion` (or PWE), **source**: the electrical primary mirror (under PO analysis), **target**: the electrical PWE object; in principle, the induced struts currents could be calculated by a `Get Currents` command using the main reflector as source. However, the struts are located in the very near field and, for this reason, the plane wave expansion method is much more efficient;
  - ☐ `Get Currents`, **source**: the electrical PWE object, output from the previous command, **target**: the geometrical object containing all the construction of the struts;
  - ☐ `Add Field`, **source**: the now electrical struts object, **target**: the preferred field storage modality (in this work, two Add Field command have been employed, for both Spherical cuts and grids).

  Such addition to the ideal struts-less optical layout will demonstrate on both the Antennas object of this work the effect of the smaller illumination provided by the shadows on the sky field of the struts, as will be observed in the results presented shortly.

5.1.5 Fields' Representation

The output fields (beam pattern) produced by the simulations are calculated in two different coordinate systems. The first one, called *spherical cut* in GRASP, is the one-dimensional spherical cuts taken in the $\theta - \varphi$ usual spherical coordinate system, where θ is the *polar angle* and φ the *azimuthal angle* [45]. The output telescope fields has been computed by assuming, in both Milano and ROSA cases, cuts of polar angles ranging from $-5°$ to $5°$, so to visualize the closest region to the main lobe and the first side lobes of the beams, and with three different azimuthal angles:

- $\varphi = 0°$, which allows to study the variation of the θ-angle in the xz plane;
- $\varphi = 45°$, θ-angle variation in the xy plane;
- $\varphi = 90°$, θ-angle variation in the yz plane.

The second coordinate system is used to represent the beam pattern in a map instead of single cuts. In GRASP, that is called *spherical grid* and in this case the field points are now located on the (x_0, y_0) plane, i.e. the projection of a portion of the spherical surface surrounding the reference system, as shown in Fig.5.6. This is represented by the (u, v) plane, where u and v are the two *pure* first coordinates of the unit vector to the field point [45]:

$$\hat{r} = (u, v, \sqrt{1 - u^2 - v^2}) \tag{5.2}$$

and are further characterized by the following trigonometric functions of the spherical angles (θ, φ):

$$\begin{cases} u = \sin\theta\cos\varphi \\ v = \sin\theta\sin\varphi \end{cases} \tag{5.3}$$

In other words, the (u, v) grid constitutes a regular grid when projected on the (x_0, y_0) plane. Furthermore, both the Full Width Half Maximum (FWHM) and the main beam peak value can be derived more accurately on the grid w.r.t. the cuts one, since the latter's results are obtained under the ideal assumption of perfectly spherical symmetric rotation of the beam.

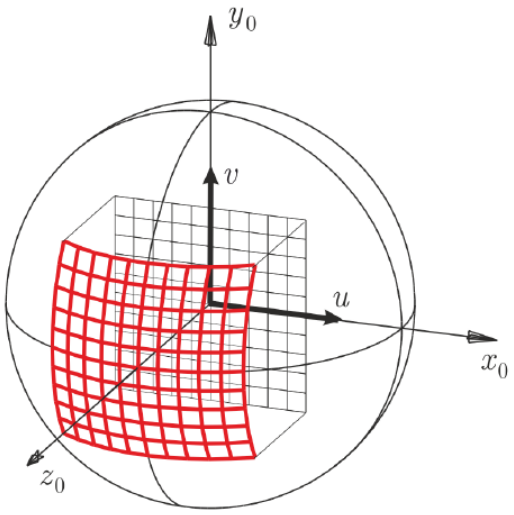

Figure 5.6: The (u, v) grid is the one projected on the (x_0, y_0) plane, while the red grid shows the far-field directions over the spherical surface described by the θ, φ angles. Credits: [45]

5.1.6 Beam Calculations of Milano telescope

Based on the model setup explained above, this section reports the beam pattern results for the Milano telescope. As shown in Fig.5.7, they have been calculated with and without struts (black beam and red beam, namely), so to compare and evaluate the diffraction effects induced by the telescope's support structure. This set of beam patterns has been computed in the case of Tabulated Horn only, since no work of optimization has been intended for the Milano Test Antenna, implying just a focus on a comparison with the realistic observation held in Milano, which will be discussed in Sec.5.2.2. The clear effects of the struts presence are evident in Fig. 5.7: the black pattern shows slightly higher side lobes in the first $\pm 1°$ region, while instead is provided with by far much higher ones in the more external angular region, thus stressing a lower level of illumination caused by the struts shadows on the primary mirror. For the struts case, spherical grid has been produced too and, so to provide better insights on the real effect of these metal structures presence, seven different spherical cuts have been produced alongside the map, with an azimuthal angle φ in the range $[0°, 90°]$ and a step of $15°$. By comparing their plots contained in Fig.5.8, it is possible to explain such phenomenon: the reasoning follows a $90°$ counter clockwise imaginary rotation on the spherical grid representation. On its (u, v) plane, let one suppose to first sit on the horizontal line given by the points $(u, 0)$; in this case, the line lies on the horizontal arm of the cross pattern produced by the struts shadow on the field storage in the sky. Since the effect of such lack of illumination is at its maximum, the height of the side lobes will be at its peak, as can be observed from the black power pattern on the seven cuts image, i.e. the $\varphi = 0°$ spherical cut. If now that imaginary line starts rotating counter clockwise from the previous horizontal position, it is possible to note that the effect of the struts will be lower and lower since the more far away from the cross pattern arms, the less the effect of the under-illumination. As a matter of fact, the lowest side lobes levels can be appreciated in the $\varphi = 45°$ spherical cut, as being equidistant from the cross arms. By following such reasoning, the struts effect will start to increase once again as a function of increasing angle φ, thus finding again a maximum effect in the $\varphi = 90°$ cut. To conclude this Section with, a zoom of the main lobe area of the spherical grid is provided, along with its peak's dB level which can be read from the colorbar provided aside (Fig.5.9).

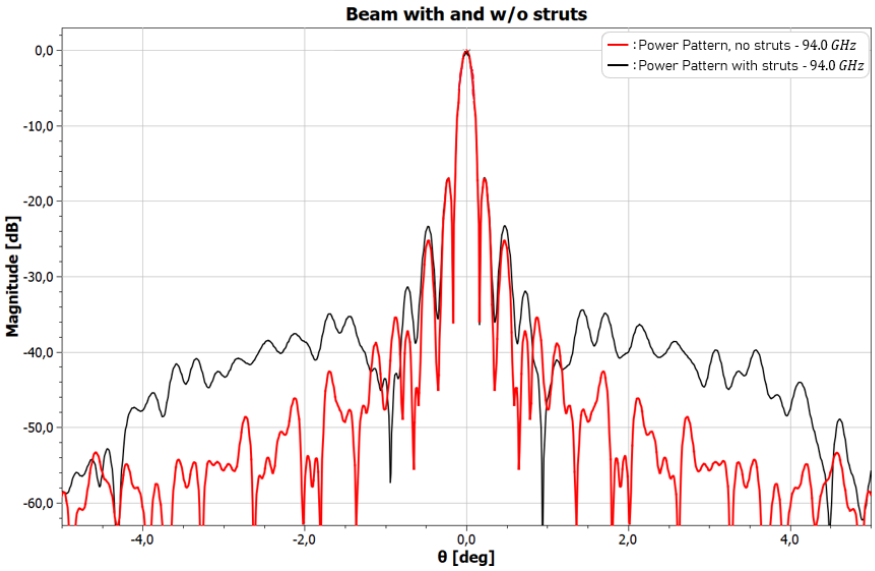

Figure 5.7: Comparison between the Power Patterns of the Milano Test Antenna in the cases of Struts presence (black curve) and struts-free layout (red curve), both produced at 94.0 GHz in range of $\theta = [-5, 5]^\circ$, 1001 points in a $\varphi = 0^\circ$ visualization, Tabulated Horn case only. The latter clearly shows an overall lower side lobes level, caused by the lack of the struts shadows upon the main reflector.

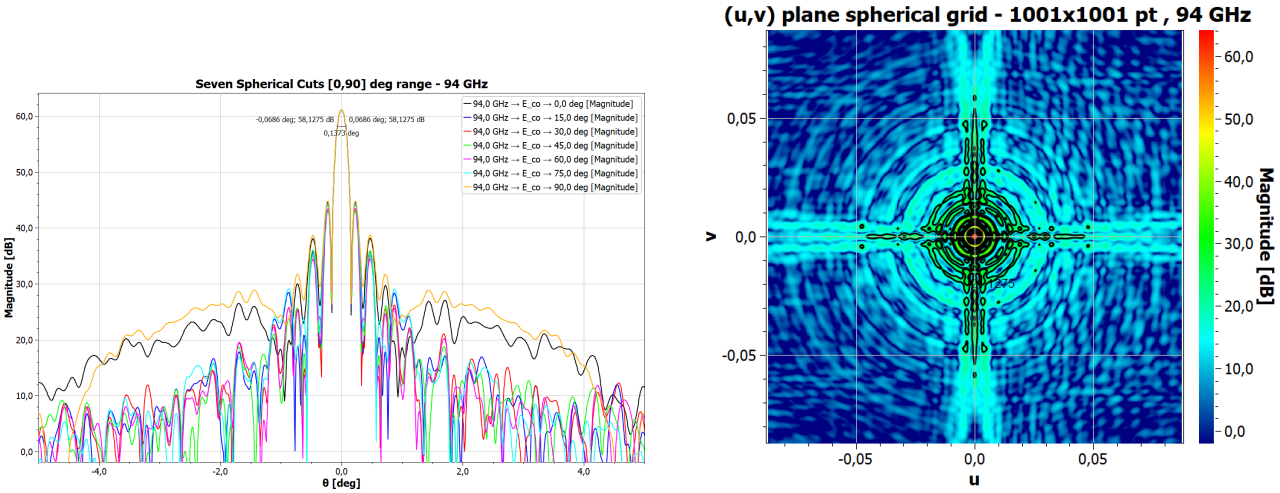

Figure 5.8: Left: the seven spherical cuts $\varphi = (0^\circ, 15^\circ, 30^\circ, 45^\circ, 60^\circ, 75^\circ, 90^\circ)$, $\theta = [-5, 5]^\circ$ reported so to explain by rotation the effect of the struts presence; **Right**: the spherical grid output of the GRASP struts configuration. The cross pattern is given by the subreflector supports shadows in the filed storage process in the sky.

5.1.7 Beam Calculations of ROSA telescope

For the ROSA antenna installed in the Concordia Base, different sets of beam patterns have been computed. The first set concerns the beams computed under the *Tabulated Horn* case in all the usual frequency range of maximum response of the EBB2 receiver's BPF, $\nu = [88, 101]$ GHz. Both the cuts and the maps were calculated for both the struts-less and with struts configuration. As a reference, the struts-less spherical cuts in the range $[-1, +1]^\circ$ are displayed in Fig.5.10, so to show the frequency dependence of main beam and sidelobes. Such beams are in

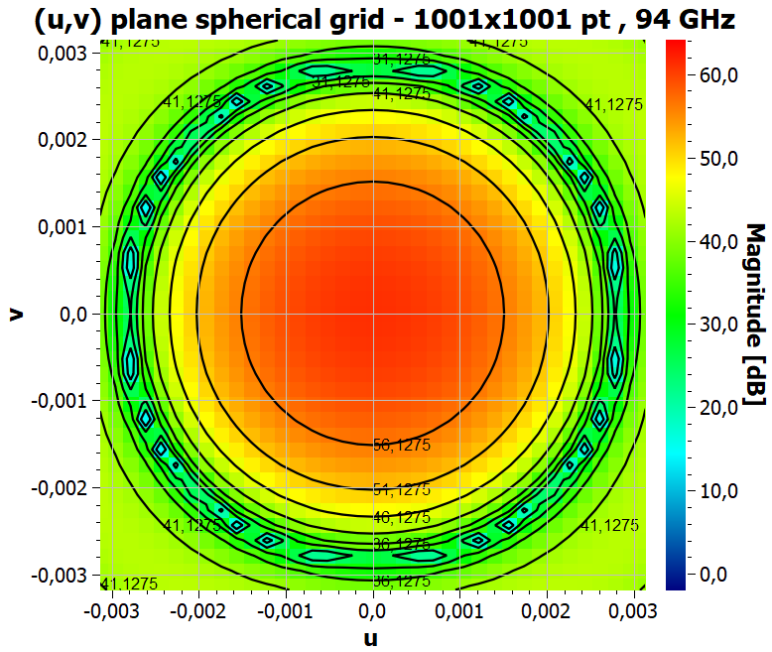

Figure 5.9: Zoom of with-struts Milano telescope spherical grid on the region containing the main lobe, as well as the very first sidelobes. 94.0 GHz, 1001 points spherical grid.

agreement with the general angular resolution relation

$$\theta \propto \frac{\lambda}{D}, \tag{5.4}$$

since the patterns produced by higher frequencies (i.e. lower wavelengths) show narrower main beams (thus lower FWHM). The second set of ROSA's beams computed in this work, displayed in Fig.5.11, has been still obtained in the case of struts-less configuration by using as feed model the *Hybrid mode conical Horn* case with a variation of the Edge Taper values in a range of $ET = [-20, -10]\, dB$, so to analyze the effect of the ET in simulated observations: this could be epmloyed to identify the configuration presenting the most optimal trade-off between sidelobes level and angular resolution (FWHM) in real sun observations. As expected, lower ET values correspond to a lower sidelobes level, because of an overall lower illumination. On the other hand, the lower illumination causes a degradation of the angular resolution. To quantify this illumination effects on beam patterns, the angular resolution, the sidelobes level and the antenna efficiency were calculated and reported in Tab.5.3 for each Edge Taper value in the range $ET = [-20, -10]\, dB$.Such patterns have been computed in the frequency range $\nu = [88, 101]\, GHz$ and, in Tab.5.3, the minimun and maximum values obtained in that ν-interval are reported. In order to study the dependence with the frequency, Fig.5.13 shows the plots of the same quantities as a function of ν at different values of edge taper. The three plots of Figure 5.13 are explained as follows:

- **FWHM vs Frequency**: this set of curves represents the variation of the FWHM as a function of the frequency at different Edge Tapers. the FWHM increases as the ET value decreases. This is given by the lower and lower level of illumination produced by narrower beams of the feed model, thus meaning lower angular resolutions corresponding to lower ET values. In general, a negative variation of the FWHM for an increasing frequency value can be readily seen as $FWHM \propto \lambda/D$;

- δL **vs Frequency**: This plot shows instead the phenomenon through which the Fourier Transforms of narrower beams (produced by lower ET values) are characterized by lower

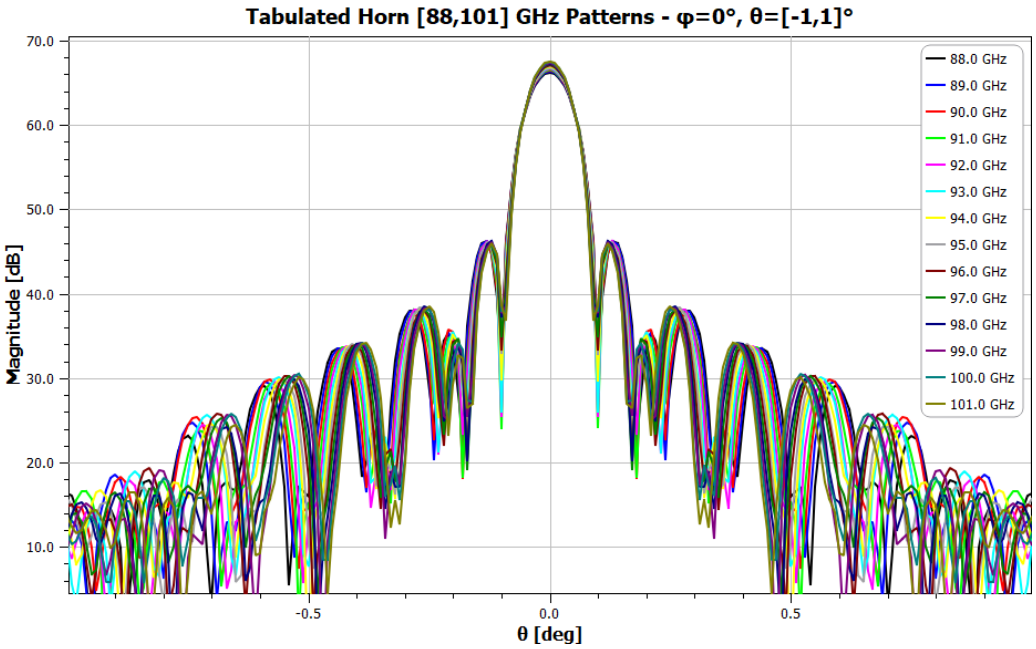

Figure 5.10: Zoom in the $\theta = [-1, 1]°$ region of the struts-less Power patterns of ROSA telescope, computed at each frequency in the EBB2's BPF, $88 - 101\ GHz$, $1\ GHz$ step. 1001 angle points spherical cuts, $\theta = [-5, 5]°$ original dimension.

sidelobe levels, thus by higher δL, i.e. the distance within main beam's peak and sidelobes' peaks. In this case the behavior in the frequency-varying case is the opposite as earlier. This is given by the fact that the *directivity*[1] $D \propto (D_{ant} \cdot \nu)^2$ and, thus, as the frequency increases, the main beam itself increases much faster w.r.t. the sidelobes, resulting in bigger δL values [38]. Tabulated and $-10\ dB$ cases present, finally, very similar behaviors;

- η_A **vs Frequency**: the last bottom-left plot points out the variation of the antenna efficiency[2] as a function of both varying ET and frequency. The first case shows the typical behavior of such quantity, finding a maximum efficiency between $-10\ dB$ and $-15\ dB$ [38]; its generally negative variation w.r.t. to the frequency, instead, is given in realistic cases by the increase of ohmic losses, roughness and phase errors [39]. Overall, the highest antenna efficiency is reached by the $-16\ dB$ ET value in the first $88-92\ GHz$ freq., followed by $-15\ dB$ for the intermediate $92-96\ GHz$ range and, finally, in the last $96-101\ GHz$ frequencies, the $-14\ dB$ ET value. In this set of antenna efficiency values, a perfect superimposition between the $-10\ dB$ and the $-11\ dB$ sets can be observed.

[1] Potentially, it indicates how much the instrument is able to focus the radiation through one direction w.r.t. the ideal isotropic antenna

[2] $\eta_A = \eta_{spill} \cdot \eta_{ill}$ [38]

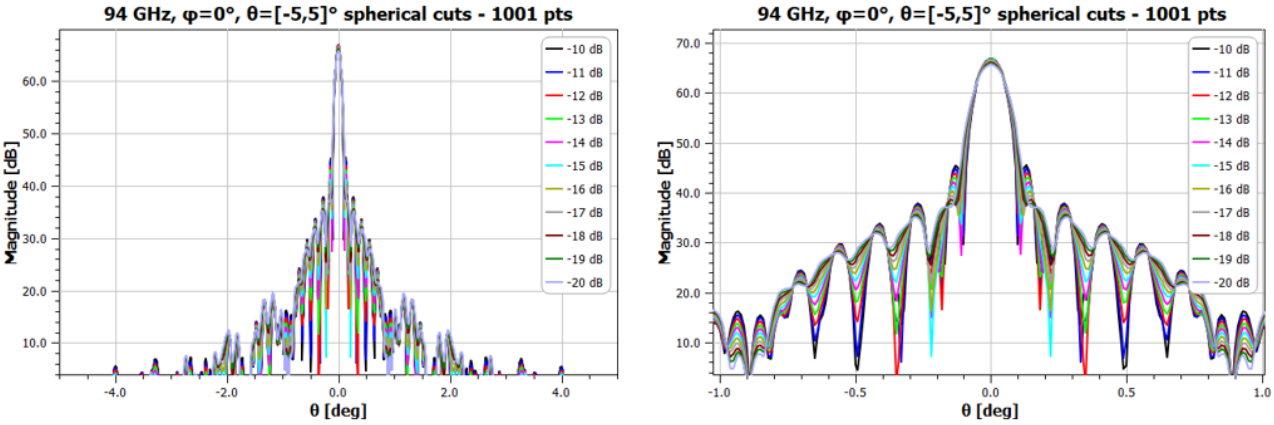

Figure 5.11: Left: ROSA beams, Hybrid mode conical horn in eleven different ET values in the range $ET = [-20, -10]\ dB$. Spherical cuts with $\theta = [-5, 5]°$, $\varphi = 0°$, 1001 points, 94.0 GHz, struts-less configuration; **Right**: Zoom in the $\theta = [-1, 1]°$ region.

$ET\ [dB]$	$FWHM\ [arcmin]$	$\delta L\ [dB]$	η_A
Tabulated	$[4.56, 5.04]$	$[19.885, 21.592]$	$[0.404, 0.445]$
-10	$[4.56, 5.10]$	$[20.615, 22.304]$	$[0.420, 0.455]$
-11	$[4.62, 5.16]$	$[20.615, 22.304]$	$[0.420, 0.455]$
-12	$[4.74, 5.22]$	$[21.844, 23.986]$	$[0.448, 0.471]$
-13	$[4.80, 5.28]$	$[22.496, 24.835]$	$[0.457, 0.473]$
-14	$[4.86, 5.34]$	$[23.193, 25.686]$	$[0.464, 0.474]$
-15	$[4.98, 5.40]$	$[23.906, 26.533]$	$[0.468, 0.473]$
-16	$[5.04, 5.52]$	$[24.629, 27.331]$	$[0.466, 0.473]$
-17	$[5.16, 5.58]$	$[25.344, 28.06]$	$[0.461, 0.472]$
-18	$[5.22, 5.64]$	$[26.03, 28.696]$	$[0.455, 0.469]$
-19	$[5.28, 5.76]$	$[26.698, 28.714]$	$[0.448, 0.466]$
-20	$[5.40, 5.82]$	$[27.326, 30.53]$	$[0.441, 0.462]$

Table 5.3: Table displaying the range of the main values between their minimum and maximum ([min,max]) of ROSA power patterns for each ET value, i.e. the Full Width Half Maximum on the main beam in degrees unit, the difference in height between the main beam peak and the first two sidelobes' peaks, δL, and finally the antenna efficiency η_A.

In conclusion, not only the $-15\ dB$ presents the best antenna efficiency values, but on top on that it shows relatively high δL values and on the same time a low range of FWHM, thus representing the best trade-off within the three quantities of interest analyzed so far for its optical configuration.

Finally, Fig.5.12 shows the power patterns of ROSA telescope's struts configuration, where the same trend of Milano case study is spotted: a maximum diffraction effect in the $\varphi = 0°,\ 90°$ along the grid cross pattern's arms and a minimum effect along the $\varphi = 45°$ one. The small difference within the higher sidelobes level patterns is given by the beam not being symmetrical, implying a slightly stronger diffraction along the 90° direction w.r.t. the 0° one. Those beams have been obtained under a Tabulated Horn condition.

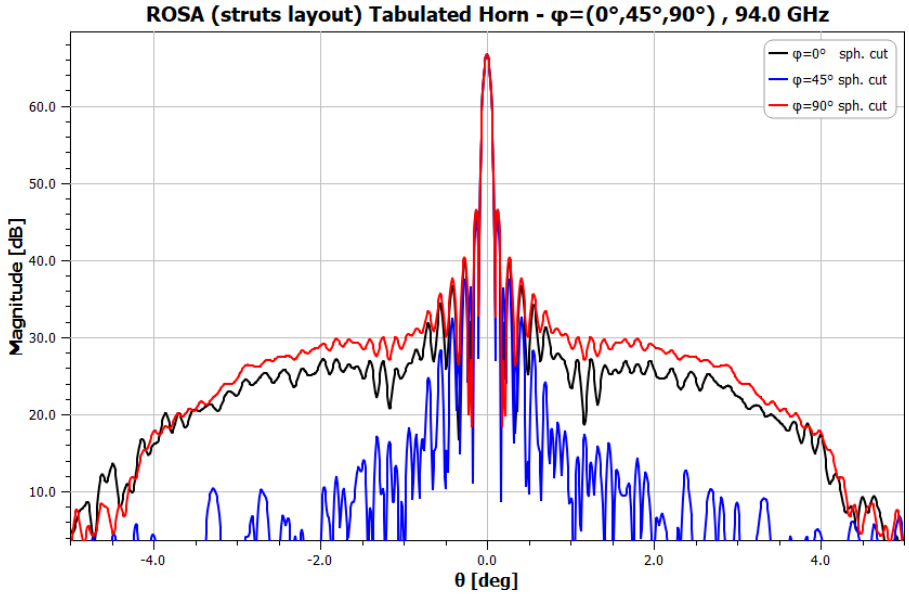

Figure 5.12: ROSA struts optical layout's beams, Tabulated Horn. Spherical cuts with $\theta = [-5, 5]°$, $\varphi = (0°,\ 45°,\ 90°)$, 1001 points, 94.0 GHz.

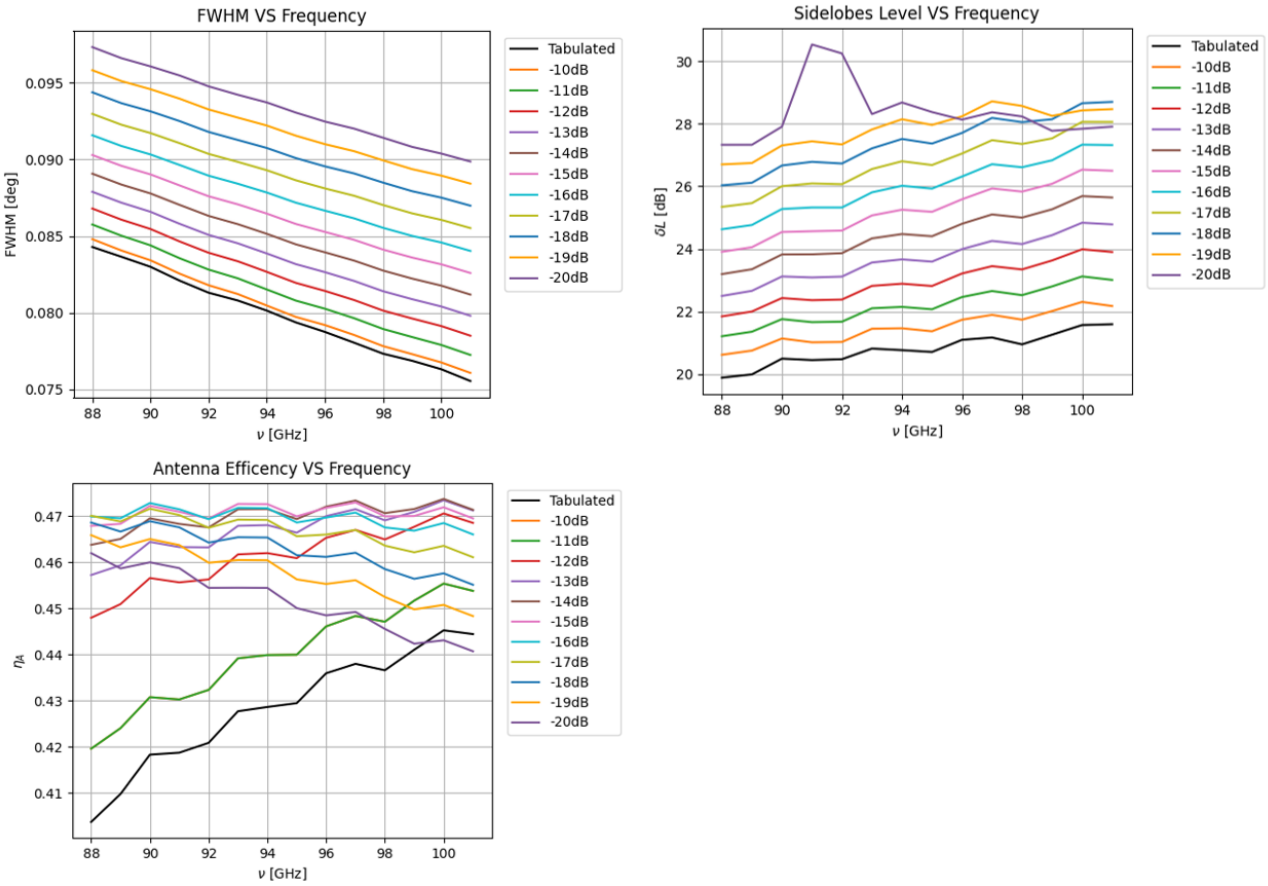

Figure 5.13: Graphic visualization of the whole values' ranges contained in Tab.5.3.

5.2 Convolutions Beam Patterns - Sun models

The aim of this paragraph is to present the convolutions of the calculated beam patterns of Milano and ROSA configurations with the brightness temperature profiles of different Sun con-

ditions, introduced shortly. While for ROSA's case the convolutions are executed to simulate the observation results of such optical configuration, the main goal of Milano telescope's convolutions is to compare them with the real solar observations taken by the EBB2 receiver mounted on such instrument during the Milano INAF mission held in October, 2025.

5.2.1 The Simulated Sun Brightness Temperature Profiles

Three different Sun models have been taken into account in order to extract their brightness temperature profile and convolve it with the telescopes power patterns:

- The **Synthetic Flat profile**: The ideal condition of Quiet Sun is well described by a synthetic flat solar brightness temperature. As shown in Fig. 5.14, its construction is

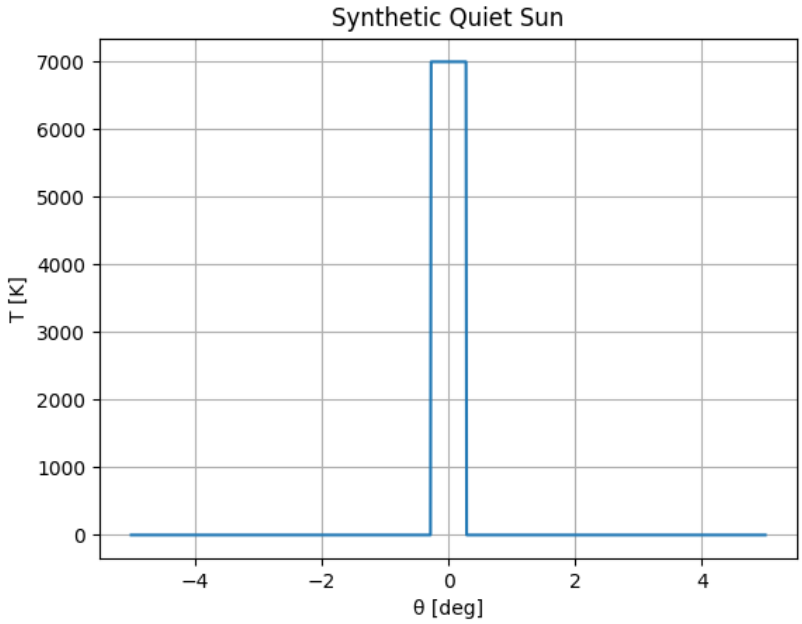

Figure 5.14: Synthetic flat Quiet Sun model, as a uniform celestial body of 7000 K over all the extension of the solar disk ($\pm 0.28°$, $33'$).

set by imposing a constant 7000 K temperature along all the extension of the radio solar disk of approximately $33'$ long [25], so within $\pm 0.28°$. It is noteworthy specifying that the temperature data on this particular profile, as well as all the others enlisted below, has been interpolated on a x-axis containing the same range and steps of degrees in which the power pattern of the Antenna has been computed ($\pm 5°$), so to be able to perform the final convolution between profiles and patterns;

- The **ALMA Quiet Sun (QS) profile**: this temperature profile has been extracted from a `.fits` file of an already existent ALMA Band-3 ($84 - 116\,GHz$, observation of the Sun, taken from the `SALSA` archive [31] of the instrument. The above mentioned observation refers to the specific frequency of $95.9\,GHz$. Shown in Fig.5.15, the Solar Map resulting from the work of [47]. In order to obtain its Brightness Temperature profile, the .fits file has been processed by a ad-hoc designed python code divided in the following steps:

  1. **Pixels' dimension extraction** - obtained from the `.fits` file header, corresponding to $6''$ ($0.001\,67°$) in both x- and y- directions;

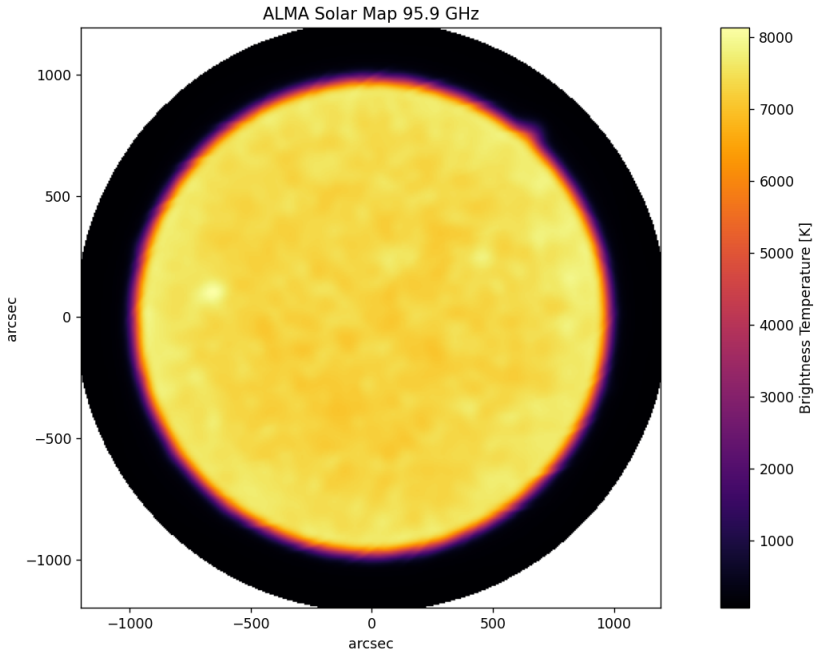

Figure 5.15: The ALMA Radio Solar Map from Band-3 observations of [47], 400x400 pixels, 0.001 67° (6 arcsec) each.

2. **Mean T_B profile extraction method** - in order to extract a profile, a binning operation has been applied, so to collect all the data by enclosing all the information of the pixels falling in the columns (bins) encountered on an equatorial scan of the image. Specifically, by considering this 400x400 pixels image, 400 vertical (along Y) 1 pixel-wide bins have been filled with all the temperatures information carried by each single pixel falling on each vertical bin, thus producing an array of 400 mean brightness temperatures values (one for each bin). Moreover, it was necessary to specify that the T_B values, before being collected, went through a masking process (described in the next point), since, as it is possible to notice from the ALMA Solar Map shown in Fig.5.15 , a ring of empty space lies around the Sun;

3. **Solar disk identification** - a Radio Solar Astrophysics (QS case) relation has been employed to extract solar disk pixels only [19]:

$$\log T_{\odot} = a + b \cdot \log \nu \, ; \tag{5.5}$$

   Eq.5.5 represents a linear relation between $\log T_{\odot}$ and $\log \nu$ and, with the parameters $a = 6.43$ and $b = -0.236$, it is able to empirically best fit the so called Differential Emission Measures (DEM) derived from Radio data, valid for $\nu \geq 10\, GHz$. In order to filter the solar disk pixels, all the values for which $T_{\odot,pix} \geq 0.5 \cdot T_{\odot,95.5GHz}$ have been included, with $0.5 \cdot T_{\odot,95.5GHz}$ being the threshold radio disk temperature obtained by plugging the $95.9GHz$ ALMA Radio Solar Map's observation frequency in Eq.5.5 [19];

4. **Profile data filling** - synthetic $0\, K$ points has been added to the profile's x-axis so to reach $\pm 5°$ and, thus, the same dimension of the above-mentioned patterns to be convolved with;

5. **Data interpolation** - in order to perform the convolution with the beam patterns,

the initial 6″ step of the solar profile has been resampled to the 0.01° step used in all the Antenna beam patterns.

The final profile obtained from these steps is displayed in Fig.5.16: it shows no features related to Solar Active Regions activities, thus resulting in a flat profile much more realistic w.r.t. the synthetic one.

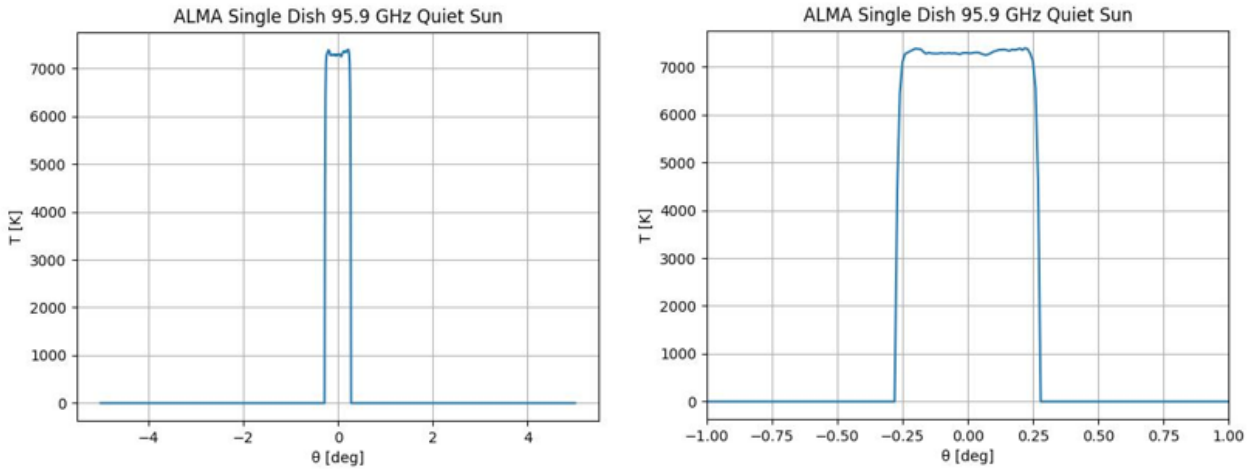

Figure 5.16: Left: the final brightness temperature profile extracted from the 95.9 GHz ALMA Radio Solar Map, De la Cruz et al. 2018, in a range of $\theta = [-5, 5]°$, 0.01° step, 1001 points; Right: the same exact profile in a zoom between $\theta = [-1, 1]°$.

- The **Solaris Active Sun profile**: this profile has been derived from the astrophysical images (Fig.5.18) obtained by the 2025 Solaris observation campaign, held in the Mario Zucchelli Station (MZS), Antarctica. Just before this campaign, the solar activity increased dramatically[3], providing a set of solar maps with active regions, from which a brightness temperature profile of such Active Sun has been extracted. It is clear from Fig.5.17 the poor angular resolution given by a beam of 4.88′, about five times wider w.r.t. the 56.6″ of ALMA. Moreover, the image has approximately four times less pixels (125x125 grid), each one one order of magnitude bigger w.r.t. the ALMA's one (0.02° vs 0.001 67°). Thus, the ARs shown in the maps are already convolved with the beam in real observations. The brightness temperature profile of this Solar Map has been extracted by following the same previous procedure and can thus be seen in Fig.5.18, which represents the observed convolved profile during intense solar activity.

By observing the shape of the last two solar temperature profiles described, it is possible to note that the ALMA QS one suggests a complete opposite behavior w.r.t. the Solaris Active profile, with an increasing T_B as one gets close to the limbs of the disk. That discrepancy is due to two radically different aspect, both rising from the fact that the solar maps from which the $T_\odot$ profiles have been extracted already represent a convolution with the beam of the instrument itself: the higher angular resolution of ALMA, characterized by a beam almost five times smaller w.r.t. the Solaris one ($\sim 52''$ vs $\sim 4.8'$), allows such instrument to resolve higher regions of the solar chromosphere (which accounts for the predominant solar emission in the observational band of this work), where the temperature increase as a function of the distance (Sec.1.1.2, Fig.1.1) from the photosphere and thus, producing a profile as the one displayed in

[3]see for instance https://svs.gsfc.nasa.gov/14683 and https://www.swpc.noaa.gov/products/solar-cycle-progression

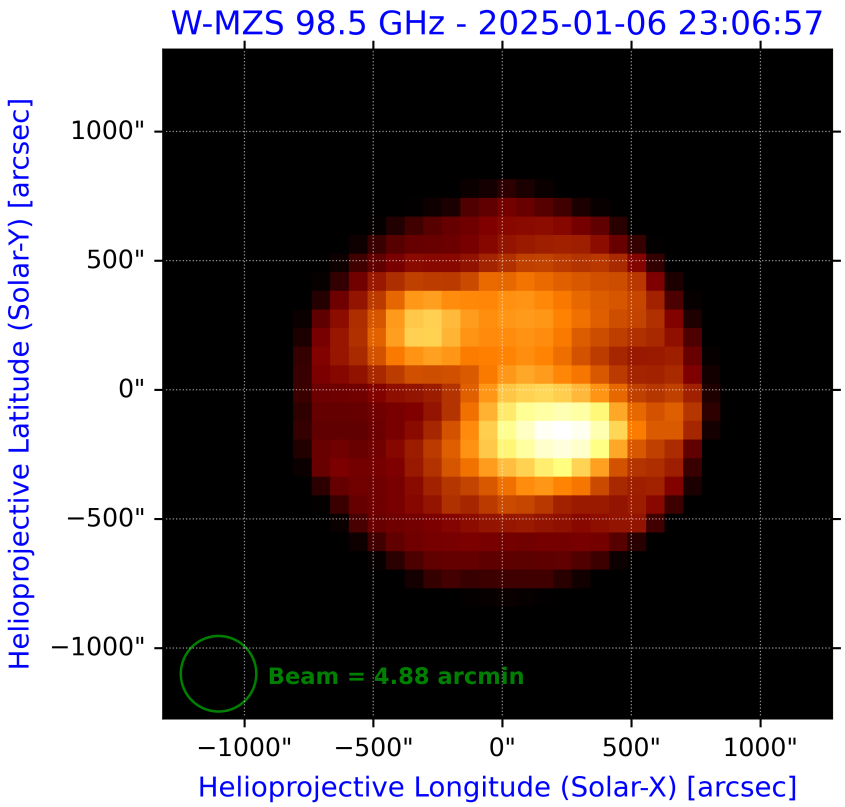

Figure 5.17: The Solaris Active Solar Map produced during the 2025 Antarctica expedition (MZS), 125x125 pixels, 0.02° each. Two visible Active regions are clearly observable on the solar disk.

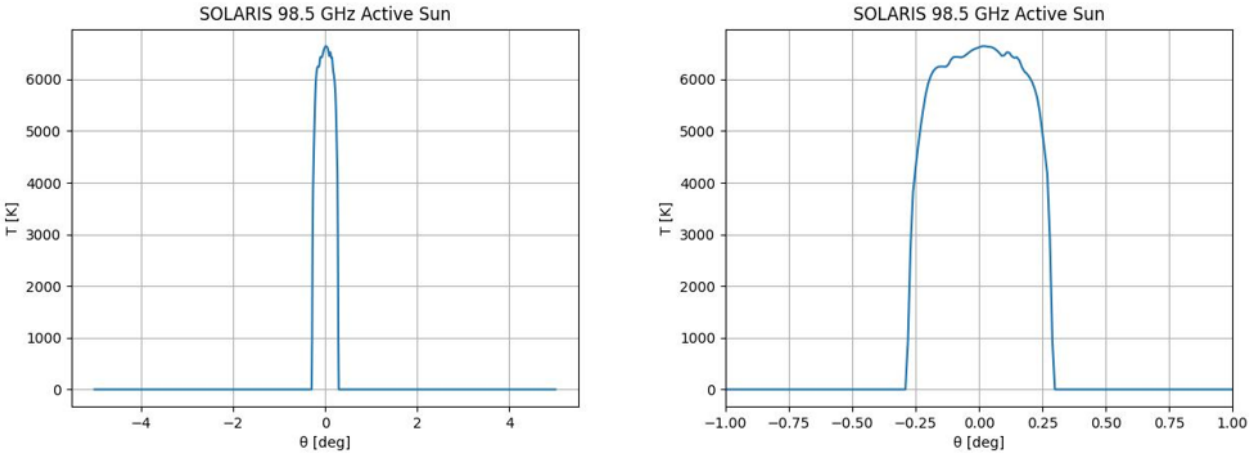

Figure 5.18: Left: the final brightness temperature profile extracted from the 98.5 GHz Solaris Radio Solar Map, 2025 Antarctica expedition (MZS), in a range of $\theta = [-5, 5]°$, 0.01° step, 1001 points; Right: the same exact profile in a zoom between $\theta = [-1, 1]°$.

Fig5.16. This effect is called *Limb brightening*[42]. The wider beam of Solaris, instead, during the process of convolution, applies the so called effect of *beam smoothing*, thus canceling most of the features. In other words, the hotter ALMA limbs arise from a real physical phenomenon, while the more bell-shaped Solaris profile is an effect dominated by the instrumental response. To model the Active Sun, different synthetic *Solar Flares* have been artificially added to the

ALMA $T_\odot$ profile in order to be convolved, turning it from a QS profile to an AR one. Those astrophysical phenomena have been assumed to be $\sim 1'$-wide and for what concerns their position on the solar disk, two cases have been analyzed: a perfectly central flare, and one located on the solar disk's edge. For each of those case-study, three levels of temperatures has been assumed, i.e. $10^5\ K$, $5 \cdot 10^4$ and $10^4\ K$. Fig.5.19 shows the three different synthetic Active Sun based on ALMA $T_\odot$ profiles in the just mentioned two Flare's temperature cases.

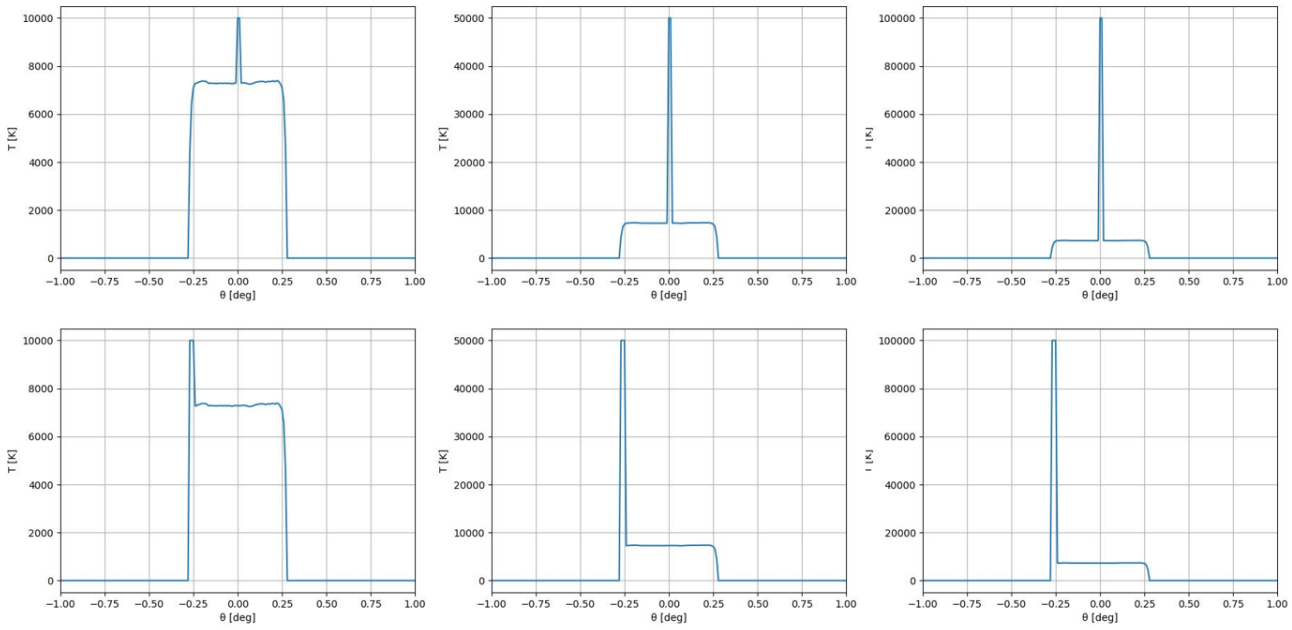

Figure 5.19: Solar Brightness temperatures profiles based on ALMA profile with artificially added synthetic solar flares; First row: central $10^5\ K$, $5 \cdot 10^4$ and $10^4\ K$ added flares; second row: edge $10^5\ K$, $5 \cdot 10^4$ and $10^4\ K$ added flares.

5.2.2 Milano Telescopes Convolutions

Solar observations have been conducted with the EBB2 receiver, installed for testing purposes on Milano Test Antenna in October 2025. In this site and period, the Sun is observable between 10 a.m. and 1 p.m., providing a relatively short time window to perform all the observations needed, which have been subdivided in two different kinds:

- **Sun Tracking** - the antenna is always pointed to the solar disk's center, as it follows its motion in the sky;
- **Solar Transit** - the antenna is set in a steady initial position, which anticipates the Solar entering in the field of view, thus, the transit of the Sun is observed with the telescope at rest. After the completion of the transit, a $300K$ blackbody (RF absorber, Fig.fig:300KLoad) is located in front of the horn aperture as a reference input temperature.

Both these observational techniques have been repeated three times each, one for each of the three bias settings of LNA enlisted in Tab.4.6, i.e. 25, 30, 35 mA for drain current, I_d. The observations, captured on October 8th 2025, lasted approximately 45 minutes, from 11:43 a.m. to 12:27 p.m.. The acquired data are shown in Fig. 5.21 in `ADU - Analog to Digital Units` as a function of time, in the HH:MM:SS format.

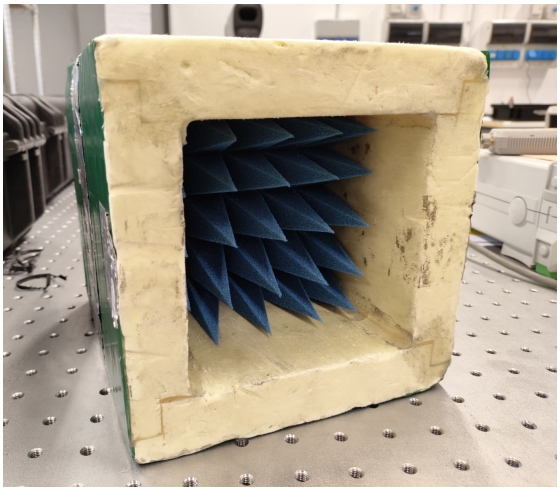

Figure 5.20: The 300 K RF absorber, which acts as a RT source.

A close view of the solar transit with the BIAS 35 set on the LNA is shown in Fig. 5.22. It is the real convolution of the Sun Brightness Temperature profile with the beam of the instrument, clearly showing a small asymmetry towards left. As a matter of fact, the next steps of this section will be dedicated to drawing final conclusions whether the physical or instrumental nature of such feature by convolving the already mentioned different $T_\odot$ profiles with the Milano telescope's power patterns presented in Section 5.1.6.

Based on [51], in this work the description of the convolution has been limited to a transit, i.e. to a one-dimensional convolution. In this case, the *Antenna Temperature*, T_A, refers to the temperature detected by the antenna as the sky brightness temperature weighted over the radiation pattern of the instrument, and can be described by the following relation:

$$T_A(\theta_0) = \frac{\int P_n(\theta - \theta_0)\, T_\odot(\theta)\, d\theta}{\int P_n(\theta)\, d\theta}\,, \tag{5.6}$$

where the numerator represents the convolution between the linear normalized-to-maximum beam or power pattern, $P_n(\theta)$, and the Brightness Temperature distribution of the Sun $T_\odot(\theta)$. In order to highlight the importance of this study and visualize the effect of telescope diffraction patterns in the observations of solar Active Regions, a sketch of a beam scanning the sun dish profile is reported, drawn in Fig.5.23. Let one suppose a beam shifting during the observation from left to right. When the main lobe is pointing towards a quiet region of the Sun, the first right side lobe is the one which first starts to collect power from the bright active source;

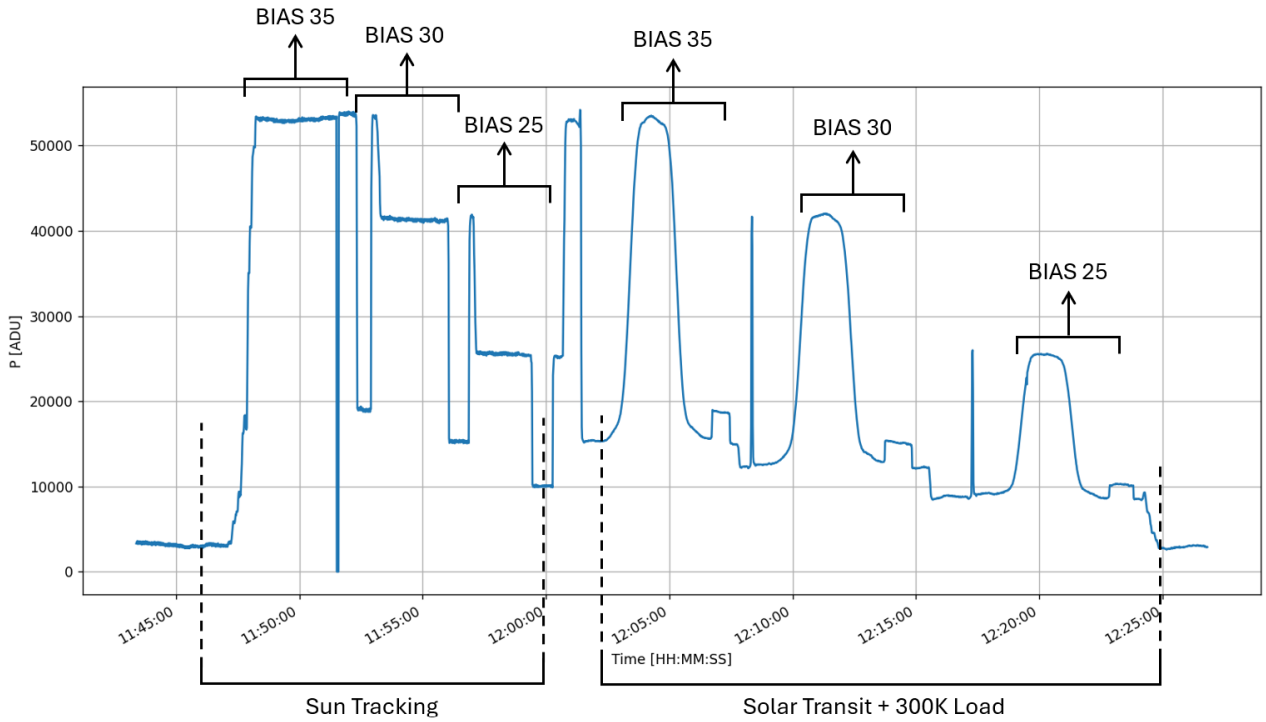

Figure 5.21: The data acquired during the Milano observation by the EBB2 Receiver mounted in the Milano 1.5m Test Antenna. Three chasings and three transits respectively, one of each for each bias setting. Data in `ADU` units per time, HH:MM:SS format.

this bright region is then observed by the main lobe and, finally, by left side lobe. The more sensitive an instrument is, the fainter the signal variation due to sidelobe pickup can be detected, increasing the possibility of a fake detection of an active region. As already intrduced in Sec.3.1, the minimum temperature detectable by a receiver is expressed by the following relation:

$$\Delta T_{min} = \frac{T_{sys}}{\sqrt{\Delta\nu \cdot \tau}} \tag{5.7}$$

where $T_{sys} = T_A + T_N$ is the system temperature, i.e. the sum of the antenna temperature T_A and the noise temperature of the receiver, $\Delta\nu$ the observational bandwidth and τ the integration time of the observation. Clearly, the lower the ΔT_{min}, the higher the sensitivity of a system. The sensitivity gives the threshold above which a signal gets detected or not, either physical or artificial: it is thus of utmost importance to be able to distinguish such origin's duality. As a final statement, in case of Active Sun real observations, the sidelobe maximum acceptable level depends on the FWHM (Eq.5.7), the receiver's sensitivity related to noise and gain (Eq.5.7), and the expected intensity and size of the active regions.

The convolutions between the beam pattern and the Sun profile have been computed in the Fourier domain, by multipling these two quantities accordingly to the Convolution Theorem. On python, this operation has been conducted through the function `fftconvolve`. The denominator provides the proper normalization, ensuring that T_A is a true beam-weighted average of the sky temperature distribution. In the integrals' computation, performed through the *Riemann sum* method , the $d\theta$ factor represents the constant step of the angular grid, thus a value $d\theta = \theta_i - \theta_{i-1}$ equal to the actual angular step used in the calculation of all the power patterns in the GRASP simulation, i.e. $d\theta = 0.01°$ (spherical cuts performed with 1001 values ranging within $\theta = [-5, 5]°$). The convolutions' results have been obtained in two different Sun conditions defined in Sec.5.2.1.

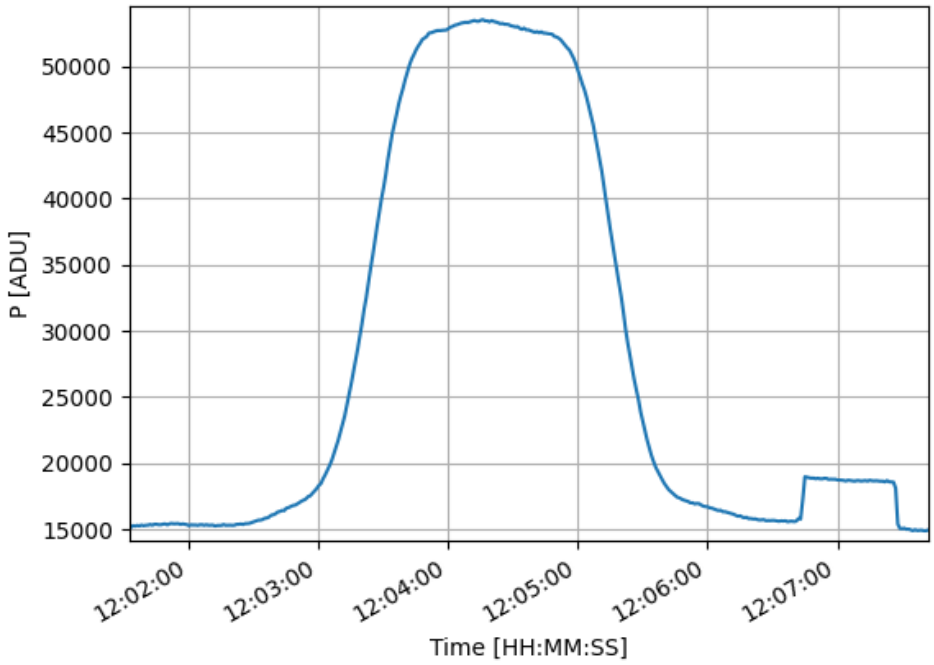

Figure 5.22: The zoom on data contained in Fig 5.21 regarding the transit of the sun detected with the EBB2 receiver mounted on Milano Telescope and with the Bias sets to 35. On the peak, a small asymmetry towards the left part of the plateau is visibile. The signal step after the transit is due to the $300K$ load faced in front at the receiver's feedhorn.

Convolutions with a Quiet Sun

In this case, the convolutions involve beam pattern cuts *without struts* (see Fig.5.7, red curve) and the Quiet Sun Brightness temperature profiles previously introduced, i.e. the Synthetic Flat profile and the ALMA profile; the results of such operations are displayed in Fig.5.24 (Synthetic profile) and Fig.5.25 (ALMA profile). From the two sets of plots, a clear similarity can be noted, thus stressing the way in which most features of a realistic profile such as ALMA's are smeared in the process of the convolution with a beam with large angular resolution. In addition, both peaks of the curves thus obtained show a symmetric behavior, thus excluding that the real Quiet Sun condition (ALMA Sun) could cause the asymmetric features present in the observed profile in Milano. To deeply investigate these asymmetries, it has been decided to conduct the same process in the case of struts presence with the ALMA Sun profile only. The set of plots in Fig. 5.26 report the convolution in logarithmic scale, so to enlarge the effects of the sidelobes. Those seven plots refer to the seven cuts of beams calculated as described in 5.1.6, i.e. cuts each 15° of step in azimuthal angle in the range $\varphi = [0°, 90°]$. As expected, the convolutions follows the same pattern of side lobes level variation described in Sec.5.1.6, with a highest diffraction effect for spherical cuts of $\varphi = 0°$ and $\varphi = 90°$, a minimum one at $\varphi = 45°$ and, finally, intermediate levels in the convolutions concerning the other remaining four cuts.

Convolutions with an Active Sun

In this other case, the beams of both struts and struts-free optical layouts of Milano telescope have been convolved with the $T_{\odot}$ profile of the Active Sun, as shown in the plots of Fig.5.19.

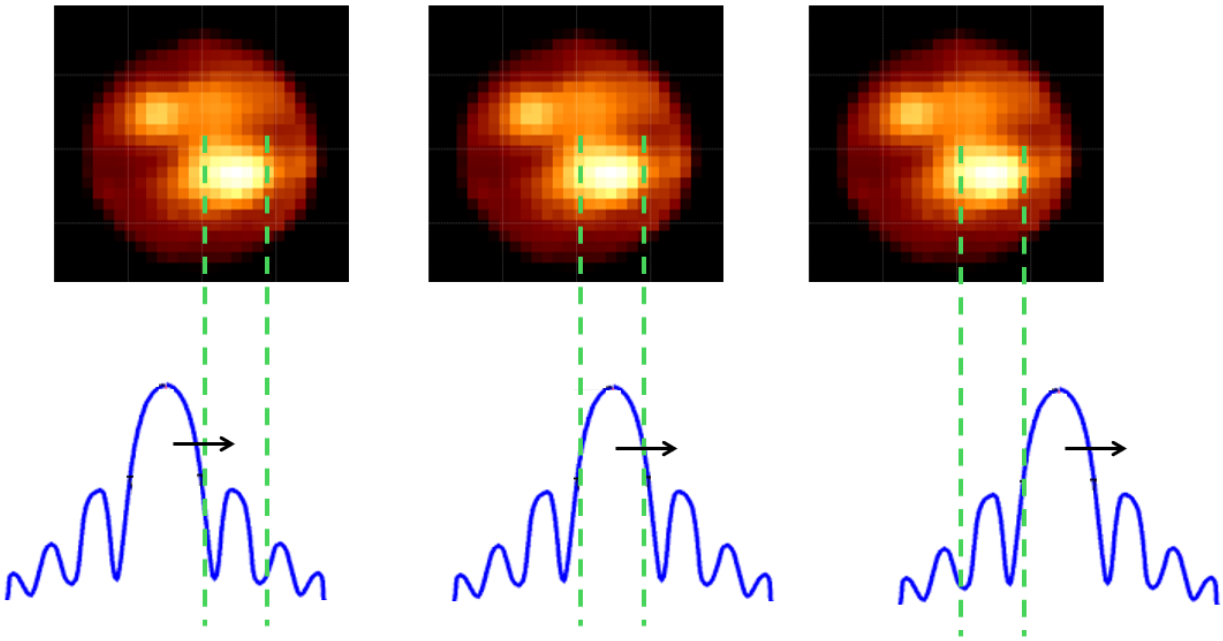

Figure 5.23: Visualisation of the observational scanning process. See text for the details; the beam shifting causes the lecture of some active regions by the side lobes, often causing an easy misinterpretation of the data given by a combination of radiometric sensitivity of an instrument and its side lobe level.

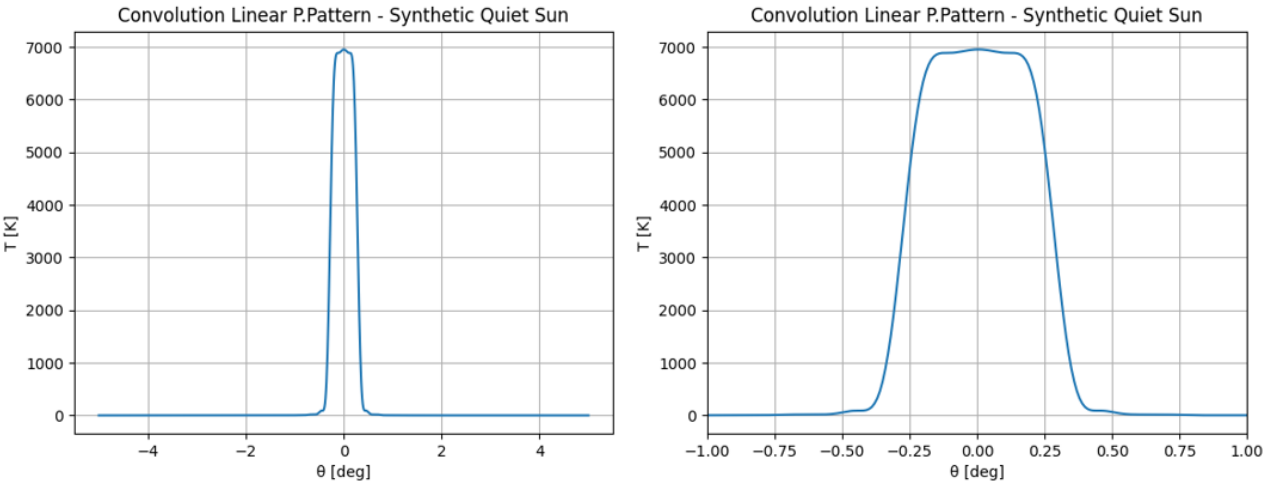

Figure 5.24: Left: convolution between the Synthetic Flat brightness temperature profile and the power pattern struts-free in a range $\theta = [-5, 5]^\circ$; Right: the same exact convolution in a zoom between $\theta = [-1, 1]^\circ$.

Three different sets of power patterns have been used to simulate the observations:

1. the beam pattern calculated with the Tabulated Feed Model and with the struts-less optical layout;
2. the beam pattern calculated with the Tabulated Feed Model, including the struts;
3. the synthetic beam pattern with a gaussian profile with the same $FHWM$ value of the main lobe of the struts-free configuration.

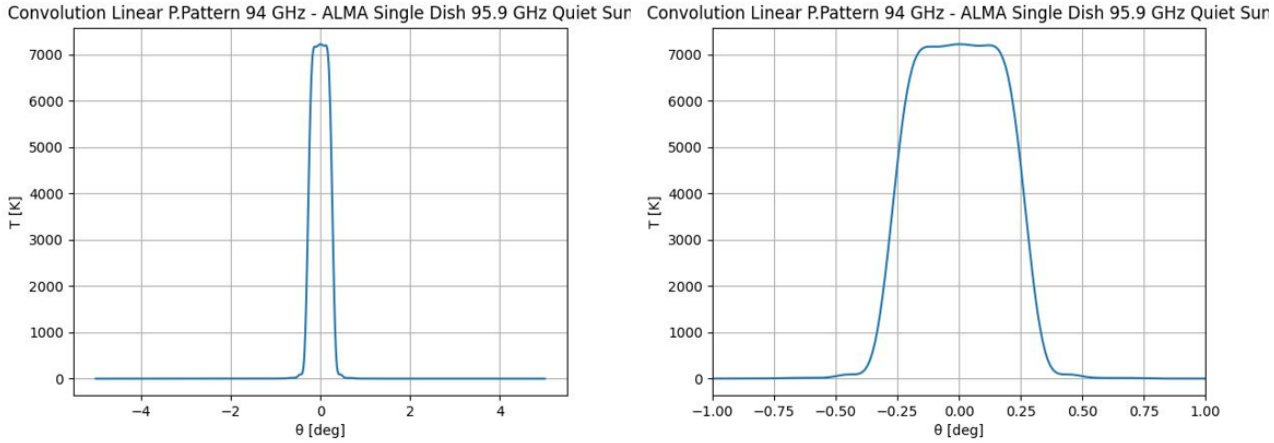

Figure 5.25: Left: convolution between the ALMA QS brightness temperature profile and the linearized power pattern struts-free in a range $\theta = [-5, 5]^\circ$; Right: the same exact convolution in a zoom between $\theta = [-1, 1]^\circ$.

The resulting convolutions within these three patterns and the usual synthetic flared sun profiles are displayed in Fig.5.27, superimposed and on a logarithmic scale, so to better highlight the different effect of each case on the convolutions' overall sidelobes level.

Fig. 5.23 shown the same plots but in linear scale and zoomed in the peak of the signal. It is readily seen from these plots that in presence of active regions, the sidelobes of the antenna pattern could mimic other active solar regions because of their signal-pickup feature.

In each of the three pairs of plots of the convolutions reported in Fig.5.28, the right one represents a zoom on a temperature fluctuation which is exactly caused by the chronologically first encounter of the edge flare with the right first sidelobe of the Antenna Beam during the observation scan (the reasoning on the equatorial beam scans treated in Fig.5.23 has been followed here). If one would measure the ΔT of the such fluctuations visible in that three plots, then the $10^5\ K$ edge flare would produce a $\Delta T \sim 400\ K$, the $5 \cdot 10^4\ K$ flare a $\Delta T \sim 200\ K$ and the $10^4\ K$ flare a $\Delta T \sim 40\ K$. In order to estimate the lowest detectable fluctuation in case of EBB2 receiver, it is necessary to provide an estimate of its radiometer sensitivity: under the reasonable assumption of a total $T_{sys} \approx 10^5\ K$ (accounting for a $T_{flare} \approx 10^5\ K$ and a thus negligible receiver noise temperature $T_N \approx 400\ K$), a $\Delta\nu = 1.4 \cdot 10^{10}\ Hz$ ($\approx 10^{10}\ Hz$) (i.e. a bandwith of $14\ GHz$, assuming the optimal receiver BPF working range of $\nu = [88, 101]\ GHz$) and the integration time $\tau_{int} = 1s$, it turns out a $\Delta T_{min} \approx 1\ K$, meaning that even the convolution product of flare as low as $10^4\ K$ would still be picked up by the beam sidelobes and thus potentially tracked by the receiver.

In conclusion, even if the effects due to the sidelobe could in principle be detected by the receiver installed during the observations' tests in Milano, the asymmetries seen on the data (Fig.5.27) cannot be justified by the sidelobes pickup. Instead, the asymmetry could be due to optical misalignment of the receiver reflecting in a not-perfectly symmetric pattern in case of quiet sun.

5.2.3 ROSA Telescope Convolutions

A similar study has been conducted in the case of the struts-less configuration of ROSA telescope (Concordia station, Antarctica), for which only the convolutions with the Active Sun model, i.e. ALMA synthetic flare Sun profiles, were calculated. Fig.5.29 and Fig.5.30 show the resulting logarithmic-scale convolutions with the ALMA $T_\odot$ profile with the addition of

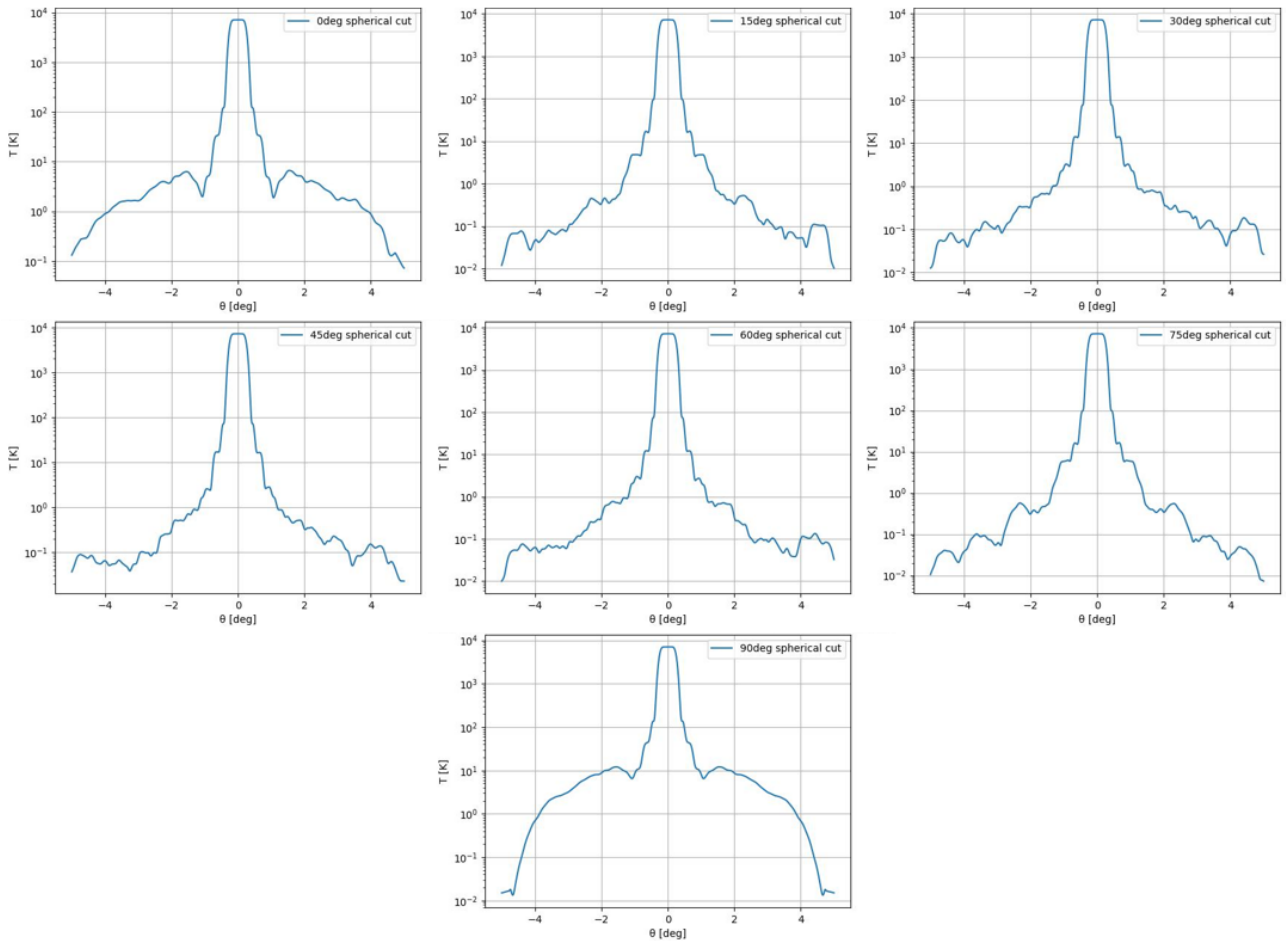

Figure 5.26: The convolutions between the ALMA QS $T_{\odot}$ profile and the seven power patterns as spherical cuts from 0° to 90° with a step of 15° effected by the presence of the subreflector support struts. First row: $\varphi = 0°$, 15°, 30° cuts convolutions; Second row: $\varphi = 45°$, 60°, 70° cuts convolutions; Third row: $\varphi = 90°$ cut convolution.

flares at the center and at the edge of the Sun. As for the Milano telescope, the three different flares' temperatures are analyzed, i.e. 10^4, $5 \cdot 10^4$, and $10^5\,K$. In such plots, the convolution of three different patterns are shown, namely the Tabulated Feed one (yellow curve), the gaussian function as for the procedure described in Sect.5.2.2 (green curve) and the Hybrid mode conical horn's beams for each value of the ET calculated in the range of Edge Taper $[-20, -10]\,dB$. For clarity, given the very large amount (198) of computed convolution, only two ET cases are reported. The first one is the convolution obtained with a beam calculated with the $ET = -20\,dB$ as reported in Fig.5.30 and the second one, the convolution obtained with a the beam calculated with the $ET = -15\,dB$ (ET set's best trade-off between antenna efficiency, FWHM and sidelobe level, Sec.5.1.7), as reported in Fig.5.29.
Furthermore, only the patterns computed at the frequency of $94\,GHz$ has been considered, since the estimated computational time required to repeat the whole calculation procedure for each of the 14 frequencies in the BPF range $\nu = [88, 101]\,GHz$ would have been too long. By observing the above-mentioned Figures, especially the ones displaying the Edge flare case, it is possible to observe the same highly asymmetric shape of the convolutions: by the left side where the flare lies, the sidelobes present at every angle very pronounced peaks w.r.t. the right one. This non trivial effect is caused by the scan acquisition process described in Sec.5.2.2, Fig.5.23, and can be divided in three main phases of scan shifting from left to right:

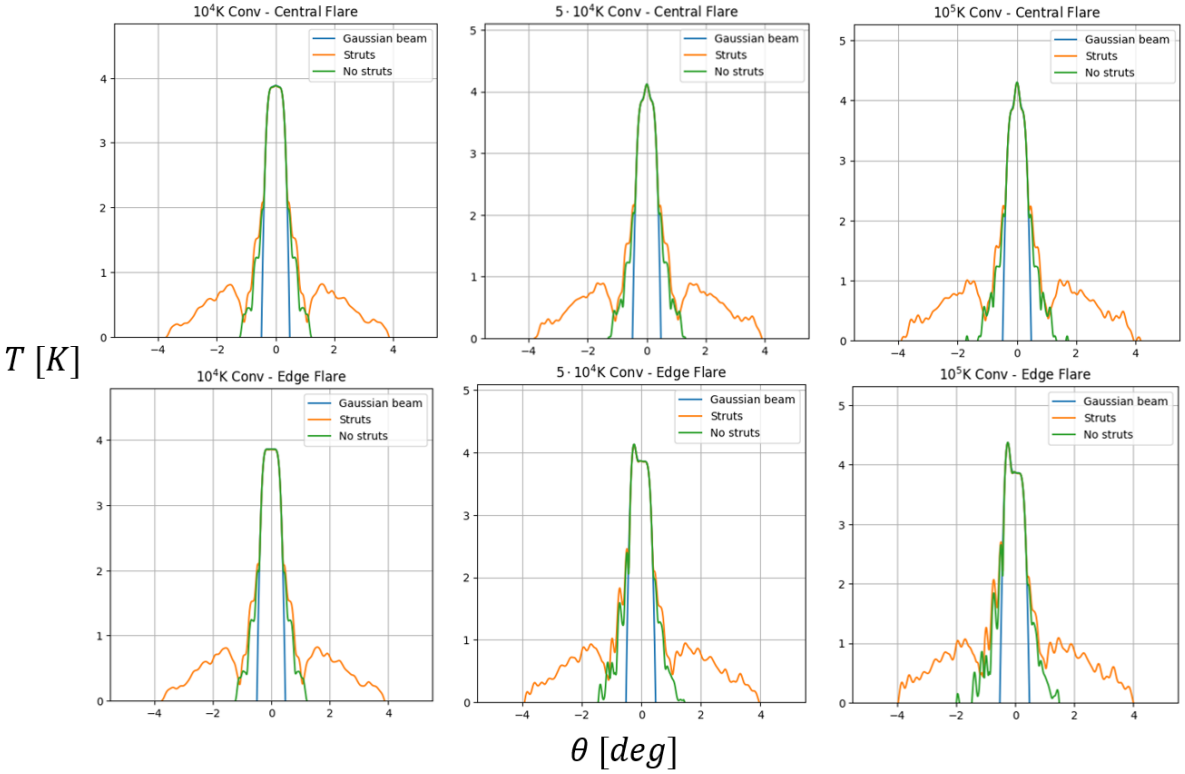

Figure 5.27: Convolution of the three different Milano Telescope beam patterns with the Active Sun based on the ALMA profile (synthetic flare-added, Fig.5.19). First row: central 10^5 K, $5 \cdot 10^4$ and 10^4 K synthetic flares; Second row: edge 10^5 K, $5 \cdot 10^4$ and 10^4 K synthetic flares.

1. **Phase 1**: the right side's sidelobes are the ones which first pickup the disk's edge flare signal. In the meanwhile, main beam and left sidelobes are scanning the space background signal, very low w.r.t. the flare signal;

2. **Phase 2**: the main beam is now detecting the flare, with right sidelobes picking up the QS signal and left sidelobes still on the background;

3. **Phase 3**: the left sidelobes now pickup the flare signal, while both main beam and right sidelobes are on the QS level.

The above-mentioned very visible asymmetry is originated by the fact that the two pickup events on the flare signal by left and right sidelobes occur in two different situations: during Phase 1, the right sidelobes are detecting the flare while the left ones pickup the background; in Phase 2, instead, by the time the left sidelobes are detecting the flare, the right ones are picking up the QS signal, clearly higher w.r.t. the background detection of the first phase. The delta of the signal picked up by the two different sidelobes is thus different, i.e. Flare vs Background (Phase 1) and Flare vs QS (Phase 2). Since the pickup of the Flare vs Background higher delta happens during the scan of the left side, this visual asymmetry manifests as very pronounced sidelobes features in the left part of the final convolution.
Moreover, Fig.5.31 shows the convolutions within the $-15\,dB$ power pattern and the central and edge 10^5 K synthetic flare added to ALMA $T_\odot$ profile, with the θ-angle ranging from $-5°$ to $+5°$: in this way the main discrepancy between tabulated and hybrid mode convolutions, occurring at angles further away from the ones locating the region which contains main beam and first sidelobes, is thus highlighted. The choice of the flare temperature $T_{flare} = 10^5 K$ has been employed so to better show the thus higher sidelobes' features in the convolutions.

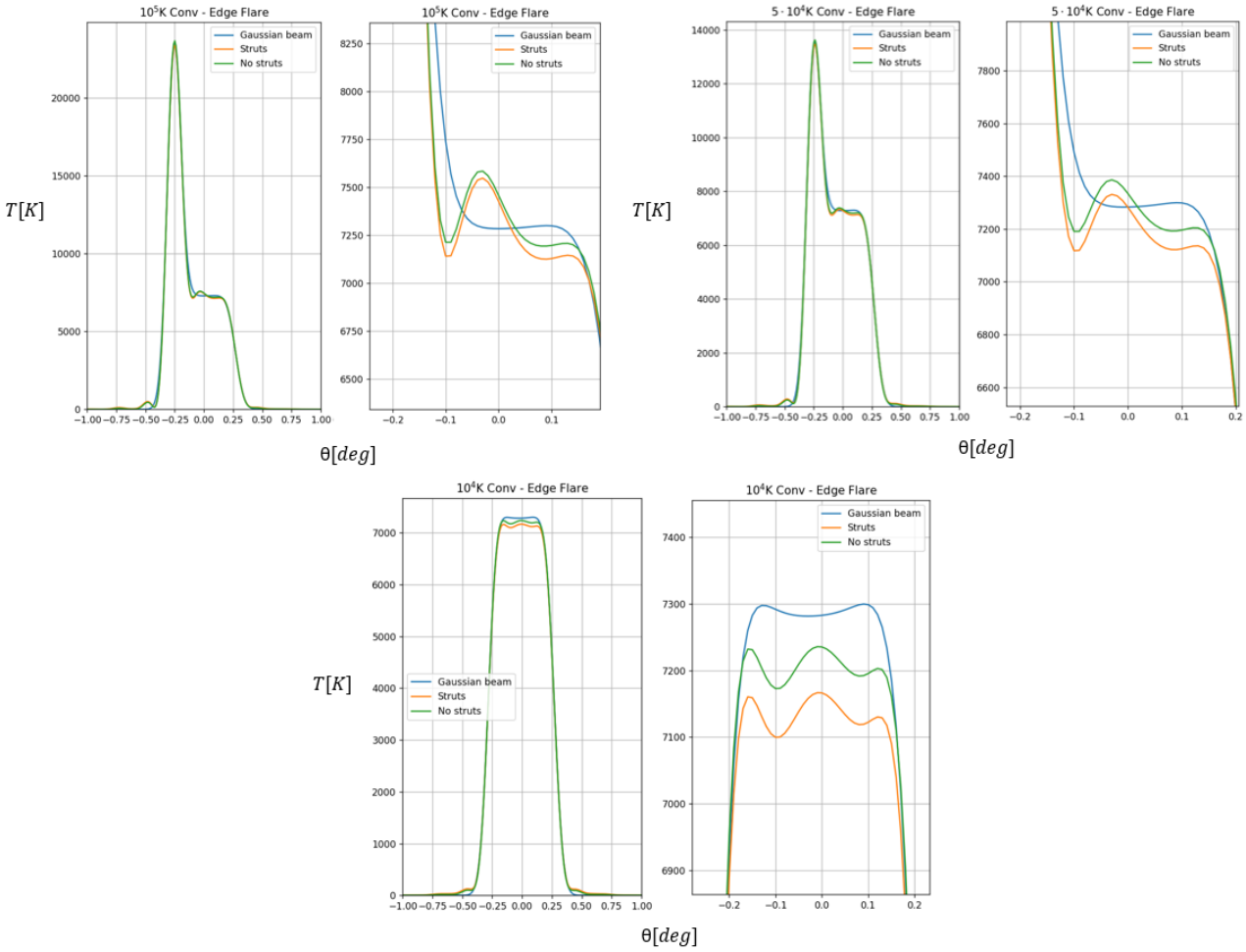

Figure 5.28: Comparison of different convolutions (gaussian curve, struts layout, struts-less layout) in linear scale, to better appreciate the features produced by the side lobes' detection of the edge flare, in all its three cases of 10^5 K, $5 \cdot 10^4$ K and 10^4 K.

To conclude with, Fig.5.32 displays instead ROSA convolutions within the Tabulated horn power pattern case and the 10^4 K, $5 \cdot 10^4$ K, 10^5 K usual flares' profiles, but this time in a linear scale in order to emphasize the widths and the different heights a flare of a given estimated temperature can reach over a quite flat Quiet Sun's Radio signal.

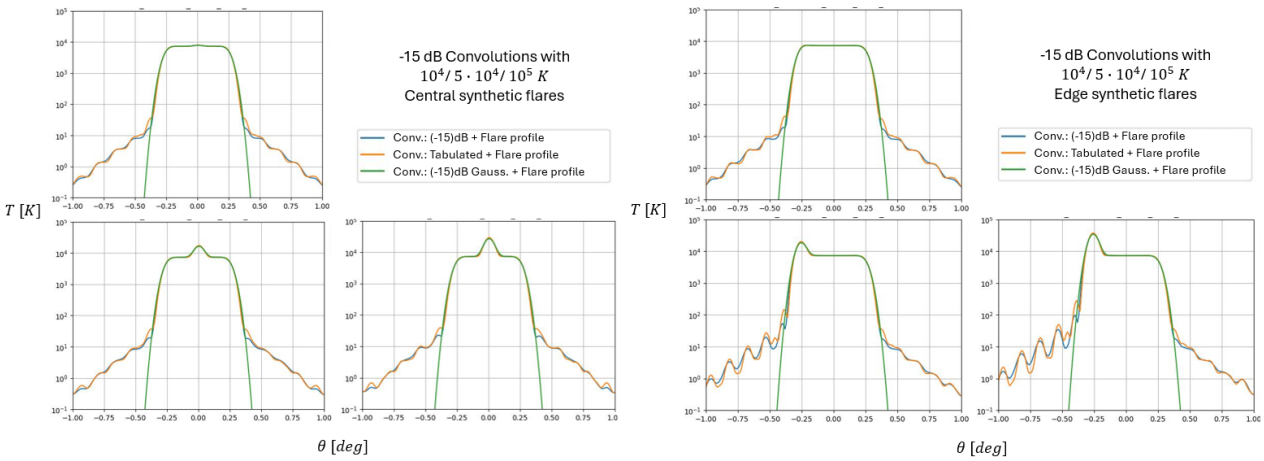

Figure 5.29: ROSA telescope convolutions with the ALMA brightness profiles with added synthetic flares. Each set of plots shows the comparison of convolutions within 10^4, $5\cdot10^4$, 10^5 flare profiles and *a)* Hybrid Mode Horn model with a $ET = -15\ dB$ (blue curve); *b)* gaussian function with the same FWHM of the beam (green curve); *c)* Tabulated pattern horn model (yellow curve). **Left**: case of 10^4, $5\cdot10^4$, 10^5 central synthetic flares; **Right**: case of 10^4, $5\cdot10^4$, 10^5 edge synthetic flares.

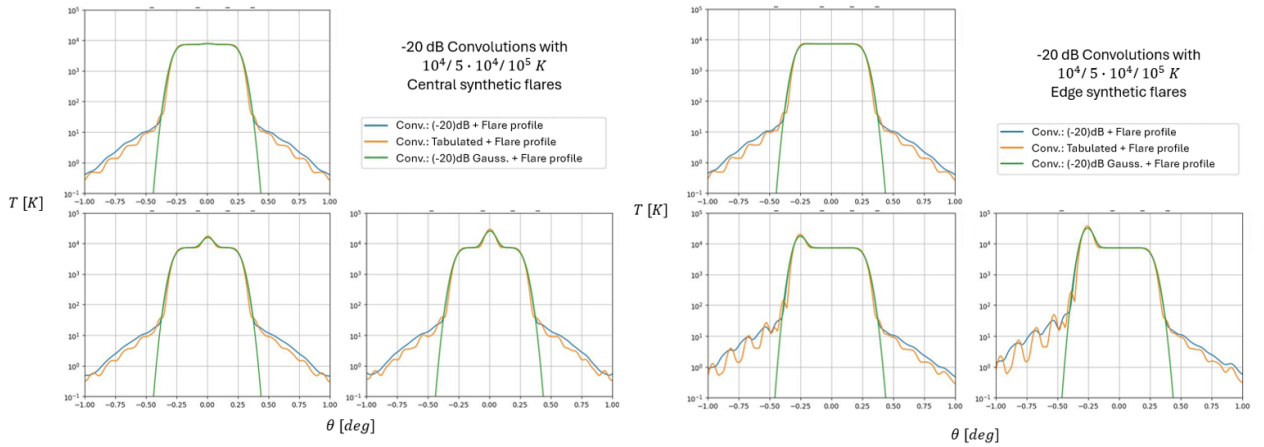

Figure 5.30: ROSA telescope convolutions with the ALMA brightness profiles with added synthetic flares. Each set of plots shows the comparison of convolutions within 10^4, $5\cdot10^4$, 10^5 flare profiles and *a)* Hybrid Mode Horn power pattern produced by a $ET = -20\ dB$ (blue curve); *b)* gaussian function produced with the same FWHM of the beam (green curve); *c)* Tabulated pattern of the antenna (yellow curve). **Left**: case of 10^4, $5\cdot10^4$, 10^5 central synthetic flares; **Right**: case of 10^4, $5\cdot10^4$, 10^5 edge synthetic flares.

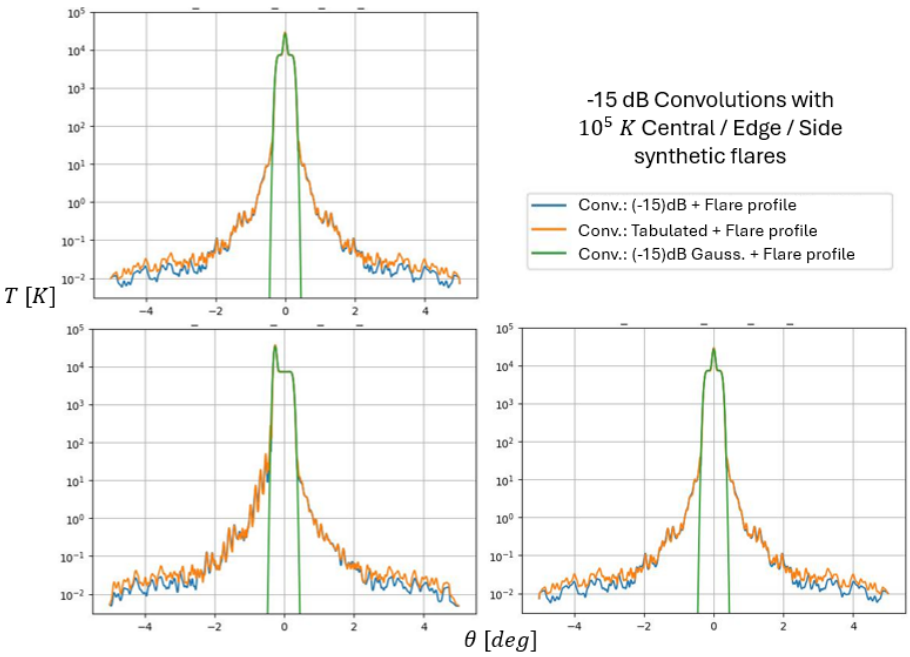

Figure 5.31: ROSA: Convolutions within the -15 dB power pattern and the central (top plot) / edge (bottom-left) / side (bottom-right) 10^5 K synthetic flare-added ALMA $T_{\odot}$ profile, with θ-angle visualization ($\theta = \pm 5°$). The discrepancy within the patterns produced by the two type of horn's models is thus observed at higher angles.

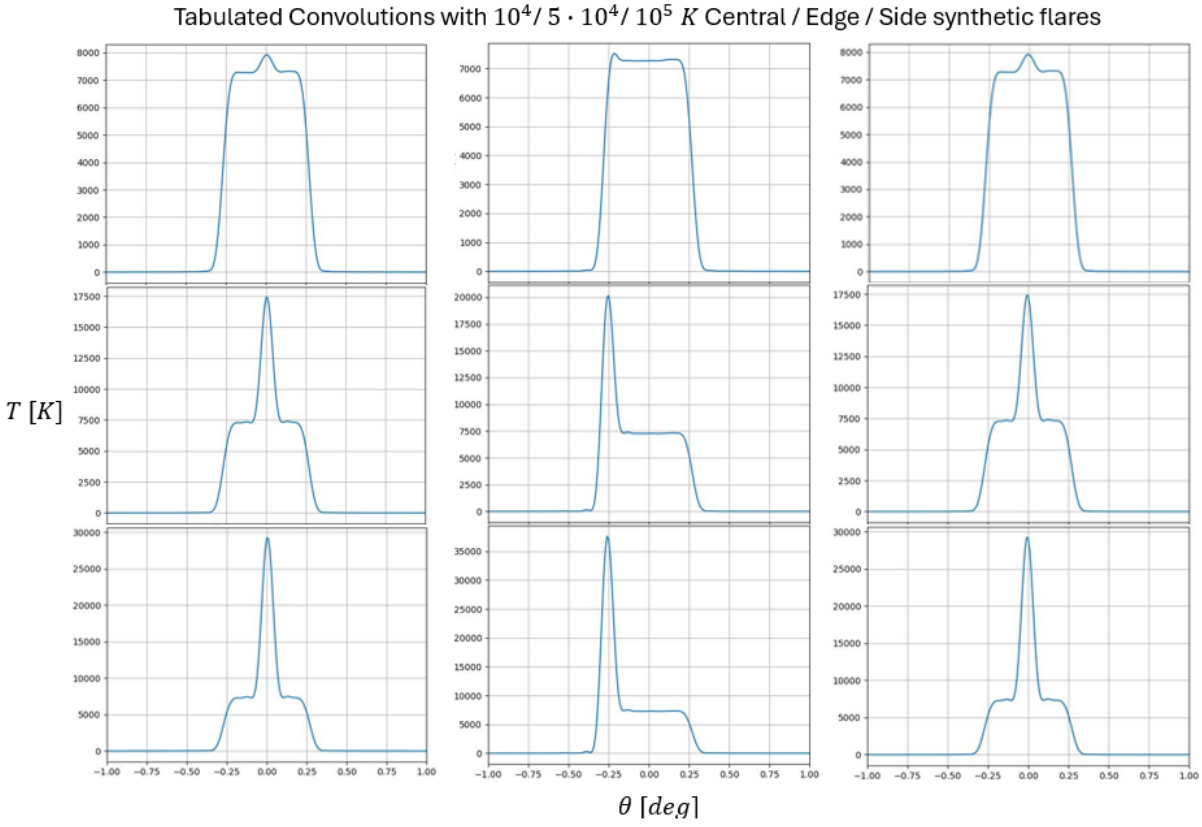

Figure 5.32: ROSA Telescope: Convolutions in linear scale with the 10^4 K (first plots' row), $5 \cdot 10^4$ K (second plots' row) and 10^5 K (third plots' row) and the power pattern calculated with the Tabulate Horn model.

Chapter 6

Conclusions and Future Perspectives

The work presented in this thesis is part of the Solaris project, which aims to observing the Sun at microwave frequencies, namely around 100 GHz, thanks to dedicated observatory facilities whose antennas are currently located in Italy, at the University of Milan and at the Testa Grigia Station, and in Antarctica, at the Mario Zucchelli and Concordia stations. Around the above-mentioned frequency, eruptive solar events occurring during periods of maximum solar activity (e.g., Solar Flares) , can be observed; the detection of such hazardous phenomena, given their potentially severe impacts on Earth's telecommunications and aeronautical workforce, have important applications in the Space Weather branch of physics. Under these circumstances, this work aimed to the development of a W-band receiver which will be able to detect their forecasting signals.
In this work, the Elegant Bread-Board n.2 receiver, or EBB2 receiver, has been assembled and then it has undergone the fundamental processes of VNA characterization and Linearity study. These analysis ensured the estimation of the receiver's Noise temperature and Gain through the realization of new dedicated python scripts, thus providing the best technical settings related to the Sun very bright radio signal's observations: the receiver itself proved its linearity not only in QS conditions, but even under the simulated observation of a 10000 K flare event.
This first practical step unlocked the possibility of conducting real test observations by installing the EBB2 receiver on the Milano Test Antenna, thus being able to observe the Sun radio signal in the unprecedented frequency range of [80-110]GHz. Furthermore, thanks to the employment of the GRASP software, the power patterns of both the Milano and ROSA Antennas were simulated, specifically to support ongoing data analysis and to study the impact of sidelobes on solar observations for further optimisations.
In this Thesis work, dedicated convolutions' routines have been realized on python to simulate observations using such beams and solar temperature profiles derived by real solar maps (Solaris and Alma). In order to provide a study better related to the Space Weather aims of this work, synthetic flares of different temperatures have been added to these profiles and their expected response to such events have been simulated.
Moreover, for what concerns ROSA telescope, an optimization study of the feed horn and related reflector illumination (Edge Taper) has been conducted for the first time under the condition of the current secondary reflectors' shape, identifying in the value of $ET = -15\,dB$ the best trade-off within ROSA's angular resolution, sidelobes level and antenna efficiency. As future developments of the Solaris project, this last-mentioned optical analysis can be further improved by studying a new custom design for the secondary reflectors of Solaris Antennas which will best suit the observational aims of the project. Finally, for this aim's backup, the customized electromagnetic study of a new corrugated feed horn will be realized in the future based on the results of this work. In addition, this prototype receiver, EBB2, together with the other prototype EBB1, mounted at the OASI station at Mario Zucchelli Antarctica Base

(not part of this study), will provide the basis for further developments towards a final receiver design, specific for Solar observations.
In conclusion, after two years of prototyping, Solaris is now entering the next phase of its development. With the forthcoming optimization of the telescope's optical design and the manufacturing of newly engineered receivers, Solaris will enable continuous monitoring of solar activity at microwave frequencies as never before. Thanks also to the $24h$ global solar monitoring coverage aimed by the realization of a northern hemisphere station, this project prospects real and essential pioneering developments and applications on the branch of the Space Weather: by providing unprecedented forecasting warnings which will contribute in the near future to the safety of ground-based and space facilities, the Solaris project will have the possibility to play its part in humanity's greatest endeavour, the exploration of our Universe.

Appendix A

A.1 Attenuator S-parameters

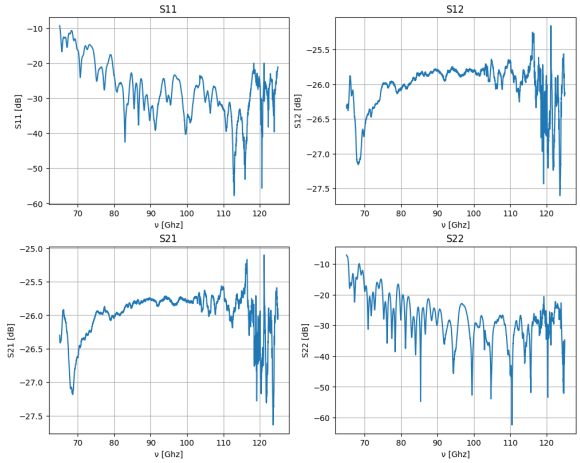

(a) Attenuator's VNA S-parameters output: -25 dB level;

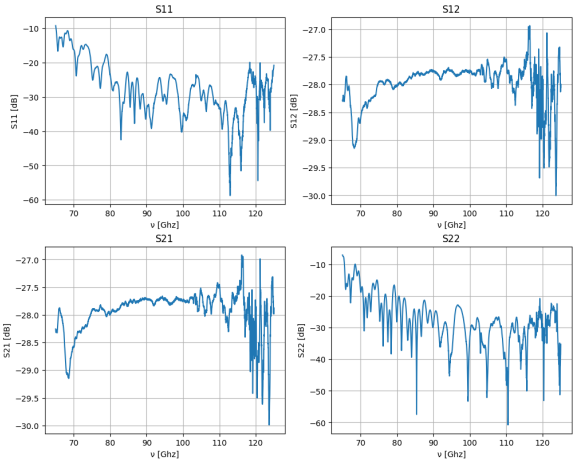

(b) Attenuator's VNA S-parameters output: -27 dB level;

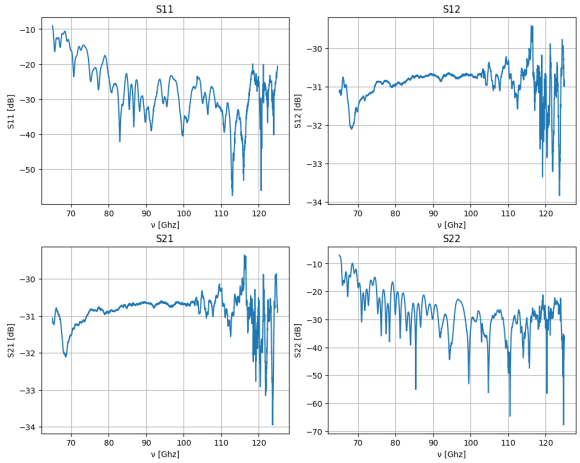

(c) Attenuator's VNA S-parameters output: -30 dB level;

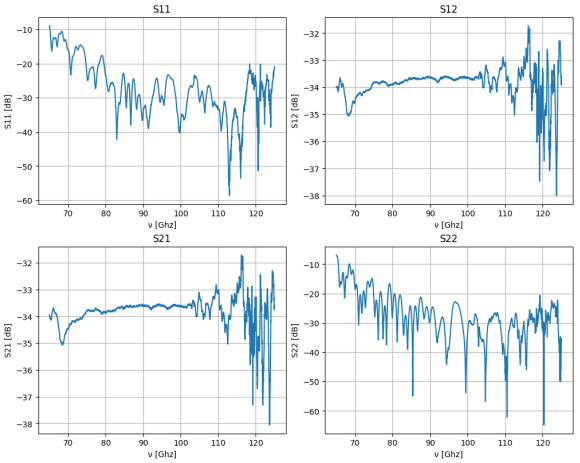

(d) Attenuator's VNA S-parameters output: -33 dB level;

Figure A.1: VNA S-parameters outputs of the Attenuator as set to the values reported on Tab.4.3.

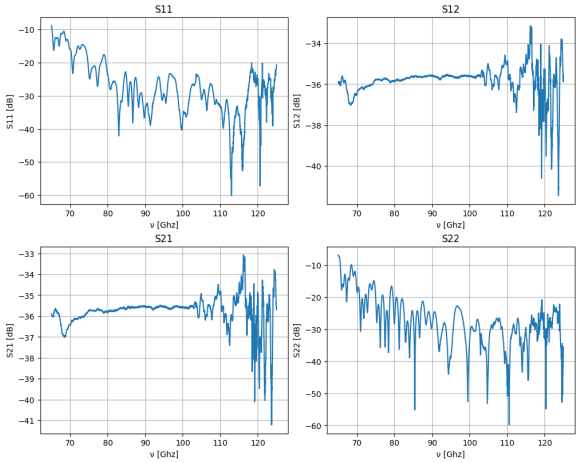

(a) Attenuator's VNA S-parameters output: -35 dB level;

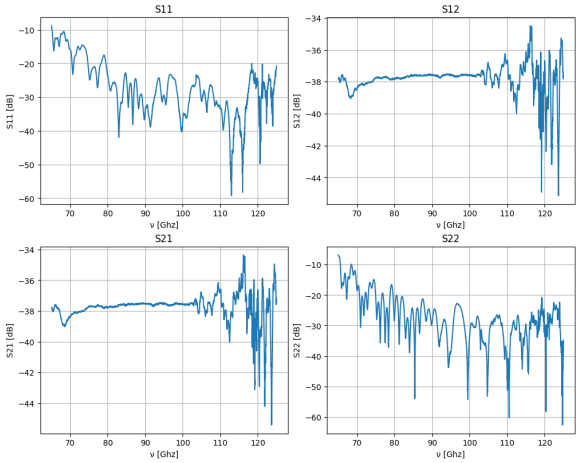

(b) Attenuator's VNA S-parameters output: -37 dB level;

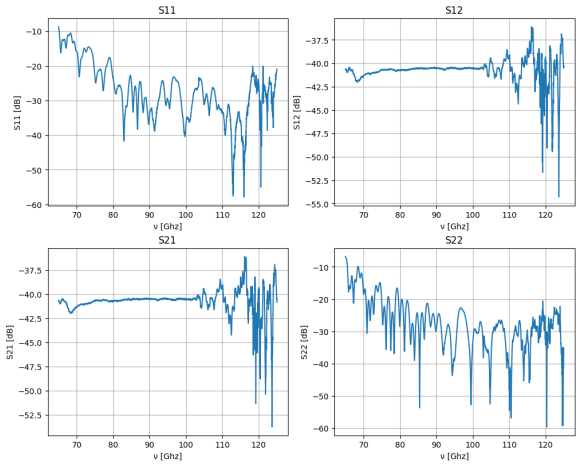

(c) Attenuator's VNA S-parameters output: -40 dB level;

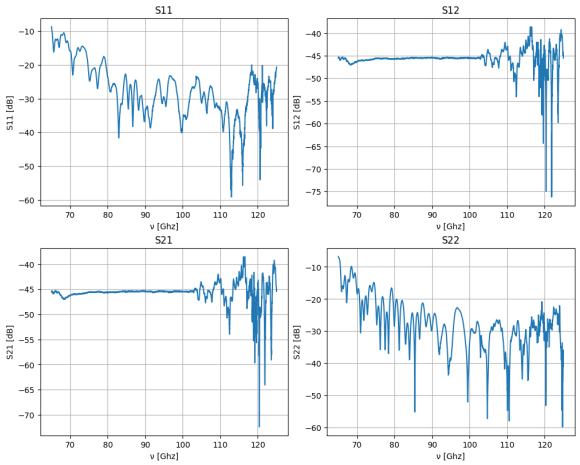

(d) Attenuator's VNA S-parameters output: -45 dB level;

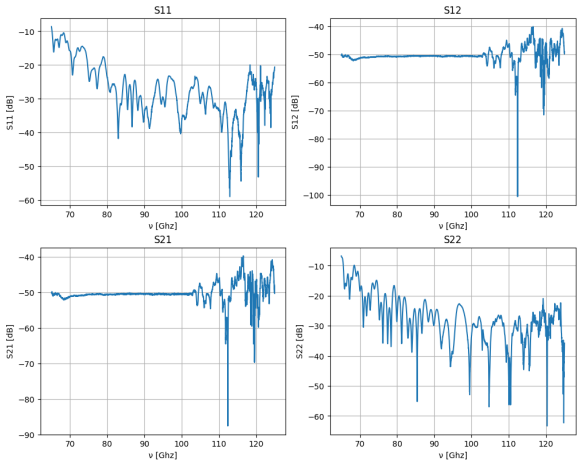

(e) Attenuator's VNA S-parameters output: -50 dB maximum level.

Figure A.2: VNA S-parameters outputs of the Attenuator as set to the values reported on Tab.4.3.

A.2 Response Curve Power Meter Data

Frequency [GHz]	Power [dBm]	Frequency [GHz]	Power [dBm]
80.0	Noise Floor	95.5	−24.18
80.5	Noise Floor	96.0	−26.34
81.0	Noise Floor	96.5	−26.55
81.5	Noise Floor	97.0	−25.90
82.0	Noise Floor	97.5	−25.00
82.5	Noise Floor	98.0	−25.74
83.0	Noise Floor	98.5	−25.49
83.5	Noise Floor	99.0	−25.79
84.0	Noise Floor	99.5	−26.47
84.5	Noise Floor	100.0	−26.51
85.0	Noise Floor	100.5	−28.55
85.5	Noise Floor	101.0	−28.77
86.0	Noise Floor	101.5	−29.88
86.5	Noise Floor	102.0	−30.74
87.0	Noise Floor	102.5	−30.85
87.5	Noise Floor	103.0	−30.66
88.0	−31.81	103.5	−30.49
88.5	−27.34	104.0	−30.26
89.0	−24.32	104.5	−30.42
89.5	−24.22	105.0	−30.61
90.0	−24.02	105.5	−30.19
90.5	−24.10	106.0	−29.78
91.0	−23.59	106.5	−29.04
91.5	−24.90	107.0	−28.22
92.0	−25.05	107.5	−27.88
92.5	−25.06	108.0	−29.12
93.0	−25.62	108.5	−27.91
93.5	−25.82	109.0	−26.51
94.0	−24.81	109.5	−26.62
94.5	−24.38	110.0	−27.58
95.0	−24.59		

Table A.1: Response Curve: absolute power values measured by the power meter as a function of the frequency in the entire EBB2 receiver working range of $\nu = [80, 110]\ GHz$, step of $0.5\ GHz$. The voice "Noise Floor" stands for a measured power below the instrument detection range of $P = [-35, +20]\ dBm$

List of Tables

List of Figures

Bibliography

[1] V. E. Abramov-Maximov et al. "Microwave Observations of Solar Active Regions". In: *Solar Physics* (2013).

[2] Markus J. Aschwanden et al. "Global Energetics of Solar Flares. V. Energy Closure in Flares and Coronal Mass Ejections". In: *The Astrophysical Journal* 836.1 (2017), p. 17. DOI: 10.3847/1538-4357/836/1/17.

[3] A. O. Benz. "Flare Observations". In: *Living Reviews in Solar Physics* 14.2 (2017). DOI: 10.1007/s41116-016-0004-3.

[4] V. M. Bogod, A. G. Stupishin, and L. V. Yasnov. "Modeling of the Solar Atmosphere Above Active Region". In: *Solar Physics* (2012).

[5] V. N. Borovik, S. A. Grigoreva, and A. N. Korzhavin. "Radio Emission of Solar Active Regions". In: *Solar Physics* (2012).

[6] P. Charbonneau. "Solar Dynamo Theory". In: *Living Reviews in Solar Physics* 7.3 (2010). DOI: 10.12942/lrsp-2010-3.

[7] P. J. B. Clarricoats and A. D. Olver. *Corrugated Horns for Microwave Antennas*. Vol. 18. IEE Electromagnetic Waves Series. IET, 1984. ISBN: 978-0-86341-003-1. DOI: 10.1049/PBEW018E.

[8] F. Cuttaia. *Lecture notes, course of Astronomical Instrumentation*. Lecture notes, INAF-OAS Bologna. 2025.

[9] G. Dall'Oglio, P. A. R. Ade, P. Andreani, et al. "The Italian Astrophysical Observatory in Antarctica: OASI". In: *Experimental Astronomy* 2 (1992), pp. 275–285. DOI: 10.1007/BF00690086.

[10] G. A. Dulk. "Radio Emission from the Sun and Stars". In: *Annual Review of Astronomy and Astrophysics* 23 (1985), pp. 169–224. DOI: 10.1146/annurev.aa.23.090185.001125.

[11] Francesco Rosario Ferraro. *Lecture notes, course of Stellar Astrophysics*. Lecture notes, Università di Bologna. Dipartimento di Fisica e Astronomia. 2025.

[12] Paul F. Goldsmith. *Quasioptical Systems: Gaussian Beam, Quasioptical Propagation and Applications*. New York: IEEE Press / Chapman & Hall, 1998. ISBN: 978-0-7803-3439-7.

[13] Robert D. Guenther, ed. *Encyclopedia of Modern Optics*. Amsterdam: Elsevier Academic Press, 2005. ISBN: 978-0-12-227600-6.

[14] D. H. Hathaway. "The Solar Cycle". In: *Living Reviews in Solar Physics* 7.1 (2010). DOI: 10.12942/lrsp-2010-1.

[15] INAF. *SOLARIS Program – SOLARIS Alpine (Testa Grigia, Alps)*. https://sites.google.com/inaf.it/solaris/the-solaris-program/solaris-alpine-testa-grigia-alps. Accessed: 2024. 2023.

[16] Instituto de Astrofísica de Canarias. *Swedish Solar Telescope*. https://www.iac.es/en/observatorios-de-canarias/telescopes-and-experiments/swedish-solar-telescope. Accessed: 2024.

[17] J. D. Kraus. *Radio Astronomy*. New York: McGraw-Hill, 1966.

[18] M. R. Kundu. *Solar Radio Astronomy*. New York: Interscience, 1965.

[19] E. Landi and F. Chiuderi Drago. "The Quiet-Sun Differential Emission Measure from Radio and UV Measurements". In: *The Astrophysical Journal* 675.2 (2008), p. 1629. DOI: 10.1086/527285.

[20] Egidio Landi Degl'Innocenti. *Fisica Solare*. Milano: Springer-Verlag Italia, 2008.

[21] J. Lee. "Radio Emissions from Solar Active Regions". In: *Space Science Reviews* 133 (2007), pp. 73–102. DOI: 10.1007/s11214-007-9206-2.

[22] S. Loru et al. "Solar radio observations". In: *Astronomy & Astrophysics* (2021).

[23] S. Loru et al. “SRT solar radio observations”. In: *Astronomy & Astrophysics* (2019).

[24] M. Marongiu et al. “Solar monitoring with the SRT”. In: *Astronomy & Astrophysics* (2020).

[25] M. Marongiu et al. “Study of Solar Brightness Profiles in the 18–26 GHz Frequency Range with INAF Radio Telescopes. I. Solar Radius”. In: *Astronomy & Astrophysics* 684 (2024), A122. DOI: 10.1051/0004-6361/202348768.

[26] D. J. McLean and N. R. Labrum, eds. *Solar Radiophysics*. Cambridge: Cambridge University Press, 1985.

[27] MLSO/HAO. *SMM CME Catalog*. https://www2.hao.ucar.edu/mlso/solar-maximum-mission/smm-cme-catalog. Accessed: 2024.

[28] NASA. *Eclipse Web Site*. https://eclipse.gsfc.nasa.gov/. Accessed: 2024.

[29] R. Nesti et al. “Design of a 67–116 GHz Corrugated Circular Horn for the ALMA Radio Telescope”. In: *2017 IEEE International Symposium on Antennas and Propagation & USNC/URSI National Radio Science Meeting*. San Diego, CA, USA, 2017, pp. 565–566. DOI: 10.1109/APUSNCURSINRSM.2017.8072325.

[30] NOAA Space Weather Prediction Center. *Solar Flares – Radio Blackouts*. https://www.swpc.noaa.gov/phenomena/solar-flares-radio-blackouts. Accessed: 2024.

[31] NRAO/ALMA. *ALMA Science Archive – SALSA*. https://almascience.nrao.edu/. Accessed: 2024.

[32] Judith de Patoul. “Stereoscopy and Tomography of Coronal Structures”. In: *PhD Thesis, KU Leuven* (2012).

[33] A. Pellizzoni et al. “Solar Radio Observations with the SRT”. In: *Astronomy & Astrophysics* (2019).

[34] A. Pellizzoni et al. “SOLARIS: a smart Solar imaging system at high radio frequency for continuous Solar monitoring and Space Weather applications”. In: *Publications of the Astronomical Society of the Pacific* (2022). See also: https://sites.google.com/inaf.it/solaris.

[35] Pellizzoni A., INAF - Osservatorio Astronomico di Cagliari. *The SunDish Project*. https://sites.google.com/inaf.it/sundish/the-sundish-project. Accessed: 2024.

[36] David M. Pozar. *Microwave Engineering*. 4th. Hoboken, NJ: Wiley, 2011. ISBN: 978-1-118-21363-6.

[37] E. R. Priest. *Magnetohydrodynamics of the Sun*. Cambridge: Cambridge University Press, 2014.

[38] Federico Maria Rossi. *TICRA Tools Design of SOLARIS OASI Dual Reflector Antenna and VNA Analysis of the 105–115 GHz SOLARIS Bandpass Filter*. Internship Report. A.Y. 2024/2025. INAF-OAS Bologna, 2025.

[39] J. Ruze. “Antenna Tolerance Theory — A Review”. In: *Proceedings of the IEEE* 54.4 (Apr. 1966), pp. 633–640. DOI: 10.1109/PROC.1966.4784.

[40] L. Sabbatini et al. “COCHISE: Cosmological Observations from Concordia, Antarctica”. In: *Journal of Physics: Conference Series* 280 (2011), p. 012006. DOI: 10.1088/1742-6596/280/1/012006.

[41] M. Sandri et al. *Optimisation of Edge Taper Values for the 70 GHz LFI Feed Horns*. Tech. rep. Available at openaccess.inaf.it. INAF, 2003.

[42] K. Shibasaki, C. E. Alissandrakis, and S. Pohjolainen. “Radio Emission of the Quiet Sun and Active Regions (Invited Review)”. In: *Solar Physics* 273.2 (2011), pp. 309–337. DOI: 10.1007/s11207-011-9788-4.

[43] Stanford–Lockheed Institute for Space Research. *SOHO/MDI Results*. http://soi.stanford.edu/results/SolPhys200/Schrijver/. Accessed: 2024.

[44] TICRA. *TICRA Engineering Consultants*. https://www.ticra.com. Accessed: 2024.

[45] TICRA. *TICRA Tools User Manual*. https://www.ticra.com. TICRA Engineering Consultants. Copenhagen, Denmark, 2023.

[46] F. Villa. *Gaussian Beam for Corrugated Feedhorns*. Tech. rep. Internal Report ITESRE 286/2000. Bologna, Italy: Istituto TESRE, CNR, 2000.

[47] S. Wedemeyer et al. “The Sun at Millimeter Wavelengths. I. Introduction to ALMA Band 3 Observations”. In: *Astronomy & Astrophysics* 635 (2020), A71. DOI: 10.1051/0004-6361/201936475.

[48] Nigel O. Weiss et al. “The Origin of Penumbral Structure in Sunspots: Downward Pumping of Magnetic Flux”. In: *The Astrophysical Journal* 600.2 (2004), pp. 1073–1090. DOI: 10.1086/380091.

[49] Wendy Carlos. *Wendy Carlos Corona photo collection*. https://www.wendycarlos.com/. Accessed: 2024.

[50] S. M. White. "The Solar–Stellar Connection". In: *Science with the Square Kilometre Array*. Ed. by C. Carilli and S. Rawlings. Vol. 48. New Astronomy Reviews. Elsevier, 2004.

[51] T. L. Wilson, K. Rohlfs, and S. Hüttemeister. *Tools of Radio Astronomy*. 6th. Berlin: Springer, 2013. DOI: 10.1007/978-3-642-39950-3.

[52] P. Yagoubov et al. "Wideband 67116 GHz receiver development for ALMA Band 2". In: *Astronomy & Astrophysics* 634 (2020), A46. DOI: 10.1051/0004-6361/201936777.